DISSERTATION

STUDIES OF MAGNETIZATION DYNAMICS IN MAGNETIC RECORDING MEDIA AND PATTERNED YTTRIUM IRON GARNET FILMS

Submitted by

Daniel Richardson

Department of Physics

In partial fulfillment of the requirements

For the Degree of Doctor of Philosophy

Colorado State University

Fort Collins, Colorado

Fall 2018

Doctoral Committee:

Advisor: Mingzhong Wu

Jose de la Venta Granda
Pavel Kabos
David Krueger
Mario Marconi

ABSTRACT

STUDIES OF MAGNETIZATION DYNAMICS IN MAGNETIC RECORDING MEDIA AND PATTERNED YTTRIUM IRON GARNET FILMS

Exchange coupling and damping are studied in magnetic media materials for applications in current perpendicular magnetic recording (PMR) technology as well as future heat assisted magnetic recording (HAMR) media technology. Damping and exchange coupling are directly related to magnetization switching time in writing operation and the signal-to-noise ratio in reading, both critical to the performance of hard disk drives.

Intergranular exchange is studied in current PMR media to see how exchange is altered in the presence of SiO_2 based segregant. By varying the segregant by as much as 30%, there is strong tunability of the exchange field between the grains. The damping in future FePt-based HAMR media is studied near the curie temperature (725 K) of FePt where the writing stage in the recording media takes place. The trends of ferromagnetic resonance (FMR) linewidth varying with the sample temperature, the volume fraction of carbon in the media, and the angle of the external field indicate that the overall damping includes strong contributions from intrinsic magnon-electron scattering as well as extrinsic two-magnon scattering between the grains. Interlayer exchange coupling and damping were studied in magnetic layered systems consisting of a soft ferromagnetic transition metal or alloy layer and a hard FePt layer at room and elevated temperatures. It was found that exchange coupling and damping are strongly dependent on temperature, the soft layer thickness, and the choice of material of the soft layer.

Spin waves are studied in the linear and non-linear regimes using magnonic crystals consisting of yttrium iron garnet (YIG) thin film strips with periodic etched lines or periodic metallic lines deposited on top of the YIG strip, as well as YIG strips with randomly spaced metallic lines deposited on top. The various media provide ways of controlling the dispersion by altering the interference of the spin waves, allowing for a wide range of interesting phenomenon to be observed.

Spin-wave fractals are observed for the first time in a YIG strip with periodic etched lines. The etched lines serve as position dependent potentials to increase dispersion in the YIG strip large enough for fractal formation in the nonlinear regime. This is also the first time fractals of any type that have been observed without the formation of time-domain solitons. Spin-wave localization is observed in the linear regime for the first time in YIG strips with randomly spaced metallic lines where the metallic lines serve as potential barriers for causing spin wave interference. Magnonic crystals consisting of YIG strips with periodically spaced metallic lines are used to compare a standing wave state with the localized state. The localized state is much stronger and much more confined to a smaller physical space than the standing wave state.

ACKNOWLEDGEMENTS

First, I would like to thank my advisor, Prof. Mingzhong Wu, for the knowledge and wisdom imparted to me over the years. It's thanks to his guidance and expertise as a research professional and an advisor that completion of this degree was possible. I would like to thank Prof. Boris Kalinikos and Prof. Carl Patton for inspiration and good discussions.

I would like to thank the members of my committee: Prof. Jose de la Venta Granda, Dr. Pavel Kabos, Prof. David Krueger, and Prof. Mario Marconi for agreeing to be on my committee and for their valuable questions and suggestions. Thanks to Dr. Kumar Srinivasan and Dr. Antony Ajan at Western Digital for their professional support over the years. Thanks to all my fellow graduate students and colleagues in the lab for their support. Special thanks to: Tao Liu, Peng Li, Praveen Janantha, David Ellsworth, Josh Lauzier, Weston Maughan, Ryan Baur, Jinjun Ding, Grant Riley, August Demann, Houchen Chang, Chris Slone, Diego Ascala, Prof. Lincoln Carr, Lei Liu, and Robert Adame.

I would especially like to thank Prof. David Krueger and Prof. William Fairbank for teaching several of my graduate level physics courses. Their enthusiasm and knowledge of physics were very inspiring, and I very much enjoyed being in their classes.

I am greatly thankful for Prof. Kevin Cornelius, Prof. Angela Douglass, and 'Dr.' Glenn Good for all the guidance and support during my undergraduate education. If it wasn't for these 3 individuals, completion of this degree wouldn't have been possible.

TABLE OF CONTENTS

Chapter 1. Introduction

1.1 Background and motivation

Electromagnetism is the study of the electromagnetic force, one of the four fundamental forces of nature that governs the physical interactions of electrically charged particles. People have been aware of electromagnetism for thousands of years, but it wasn't until the last hundred years or so that physicists began to truly understand it's microscopic origins. With the development of a theory of quantum physics in the early 1900s, it became clear that many properties of matter are quantized. Physicists learned that microscopic particles have quantized charge and motion, among other things, and that the motion of electrically charged particles is fundamentally what creates magnetic fields. In materials deemed 'magnetic materials' the origin of macroscopic electromagnetic properties can be traced back to the collective motion of electrons orbiting a nucleus of an atom. An electron possesses two types of angular momentum in orbit around a nucleus. The first is a transient form of angular momentum that we call orbital angular momentum, while the other is an intrinsic form of angular momentum that we call spin angular momentum. Another way to view this is that orbital motion is motion of the center of mass while spin is the motion about the center of mass. Lastly, though electromagnetism encompasses electric and magnetic interactions, since all of the work in this dissertation take place in the magnetostatic limit, much of the work in this dissertation is devoted to the magnetic interactions.

One of the earliest applications of magnetism was the invention of the compass that is used for navigation using the Earth's magnetic "north" and "south" poles. Today, magnetic fields can be found in almost every aspect of everyday life. They play a key role in magnetic resonance imaging (MRI) machines, magnetic memory, electric generators, RF communication devices, and

even refrigerators. To create faster and more energy efficient technology, current scientific research is performed at the nanoscale level. Whether the applications are for data storage, high-frequency communications, or keeping your refrigerator cool, it's important to understand the microscopic magnetic interactions that enable these technologies.

In this dissertation, the introduction sections use the SI unit system (chapters 1-3) while many of the experimental data and analyses use the CGS unit system (chapters 4-8). Traditionally, magnetics research in the United States is done using gaussian units, but the SI unit system is the international standard of units.

1.2 Dissertation outline

This dissertation presents a comprehensive study of spin wave dynamics in yttrium iron garnet (YIG) structures, as well as exchange coupling and damping in current and next-generation hard drive media. Chapter 2 will present an introduction to electromagnetism in magnetically ordered materials and discuss dissipation and scattering mechanisms, as well as wave propagation. Chapter 3 will describe the various experimental methods and techniques used throughout this dissertation. Chapters 4-6 will show experimental results for exchange coupling and damping in current and next-generation hard drive materials. Chapter 7 and 8 show experimental results for spin-wave experiments performed using patterned YIG structures. Finally, chapter 9 will summarize the main findings.

Chapter 2. Introduction to magnetization dynamics

2.1 Fundamentals of electromagnetism

The fundamental equations governing electromagnetism are Maxwell's equations

$$\nabla \cdot \mathbf{B} = 0 \tag{2.1}$$

$$\nabla \cdot \mathbf{E} = \frac{\rho}{\varepsilon_0} \tag{2.2}$$

$$\nabla \times \mathbf{E} + \frac{\partial \mathbf{B}}{\partial t} = 0 \tag{2.3}$$

$$\nabla \times \mathbf{B} - \frac{1}{c^2}\frac{\partial \mathbf{E}}{\partial t} = \mu_0 \mathbf{J} \tag{2.4}$$

along with the Lorentz force equation

$$\mathbf{F} = q\mathbf{E} + q\mathbf{v} \times \mathbf{B} \tag{2.5}$$

and the continuity equation[1,2]

$$\nabla \cdot \mathbf{J} + \frac{\partial \rho}{\partial t} = 0 \tag{2.6}$$

These quantities are defined as:

B is the magnetic flux density (T);

E is the electric field intensity (V/m);

ρ is the total electric charge volume density (C/m^3);

$\epsilon_0$is the permittivity of free space (F/m);

$\mu_0$is the permeability of free space (H/m);

c is the speed of light in a vacuum (m/s);

J is the total electric current volume density (A/m^2);

F is the force (N);

q is the electric charge of a particle (C); and

v is the velocity (m/s).

Here, all the quantities are assumed to be time and position dependent. It should be noted that though the above fields are the macroscopic fields, Maxwell's equations hold microscopically as well. The Lorentz force and continuity equations must be slightly modified when applied to microscopic circumstances, as their physical meanings are slightly different. These equations are also valid when considering relativity, but relativistic effects (other than the existence of spin) will be ignored because all of the work in this dissertation is done in the non-relativistic limit.

The uniqueness theorem and the superposition principle allow for a convenient choice of harmonic time dependence $e^{-i\omega t}$, so that arbitrary solutions can be formed from a Fourier superposition. Now Maxwell's equations can be written as

$$\boldsymbol{\nabla} \cdot \mathbf{B}(\mathbf{r}) = 0 \tag{2.7}$$

$$\boldsymbol{\nabla} \cdot \mathbf{E}(\mathbf{r}) = \frac{\rho(\mathbf{r})}{\varepsilon_0} \tag{2.8}$$

$$\boldsymbol{\nabla} \times \mathbf{E}(\mathbf{r}) - i\omega \quad (\mathbf{r}) = 0 \tag{2.9}$$

$$\boldsymbol{\nabla} \times \mathbf{B}(\mathbf{r}) + \frac{i\omega}{c^2}\mathbf{E}(\mathbf{r}) = \mu_0 \mathbf{J}(\mathbf{r}) \tag{2.10}$$

It's often convenient to define a magnetic vector potential and electric scalar potential

$$\mathbf{B}(\mathbf{r}) = \boldsymbol{\nabla} \times \mathbf{A}(\mathbf{r}) \tag{2.11}$$

$$\mathbf{E}(\mathbf{r}) = -\boldsymbol{\nabla}\Phi(\mathbf{r}) + i\omega\mathbf{A}(\mathbf{r}) \tag{2.12}$$

where $\mathbf{A}(\mathbf{r})$ is the magnetic vector potential and $\boldsymbol{\Phi}(\mathbf{r})$ is the electric scalar potential. They can be freely transformed according to

$$\mathbf{A} \rightarrow \mathbf{A}' = \mathbf{A} + \boldsymbol{\nabla}\Psi \tag{2.13}$$

$$\Phi \rightarrow \Phi' = \Phi - \frac{\partial \Psi}{\partial \mathrm{t}} \tag{2.14}$$

Equations (2.13) and (2.14) describe what is called a gauge transformation. Maxwell's equations can be rewritten in terms of the vector and scalar potentials for convenience, but some restrictions must be put in place by choosing a specific gauge. To the author's knowledge the current scientific consensus is that the choice of gauge in electromagnetism doesn't hold any physical meaning since the electric and magnetic fields are unchanged by the choice of gauge. The gauge is purely chosen as a matter of convenience for a specific circumstance, though some choices can lead to strange and unphysical consequences for the scalar and vector potentials. The two most widely used are the Coulomb (sometimes called radiation or transverse) and Lorenz gauges, but they will not be discussed in detail here. The Lorenz gauge has the benefit of being Lorenz covariant and is widely used when transforming between reference frames in special relativity. The Coulomb gauge allows for easy quantization of the vector potential and is widely used in quantum electrodynamics and condensed matter physics. The coulomb gauge will be used throughout this dissertation.

2.2 Electromagnetism in a macroscopic medium

So far, not much has been said about $\mathbf{J}$ and ρ. They include the contributions from free charges as well as bound charges when the fields propagate through matter. $\mathbf{J}$ and ρ can be written as

$$\mathbf{J} \rightarrow \mathbf{J}_{\text{total}} = \mathbf{J}_{\text{free}} + \mathbf{J}_{\text{bound}} = \mathbf{J}_{\text{free}} + \mathbf{J}_{\text{magnetic}} + \mathbf{J}_{\text{electric}} \tag{2.15}$$

$$\rho \rightarrow \rho_{\text{total}} = \rho_{\text{free}} + \rho_{\text{bound}} = \rho_{\text{free}} + \rho_{\text{electric}} \tag{2.16}$$

To describe the bound charges in order to gain useful insight, the analysis from here on will only apply to macroscopic dynamics so that useful approximations can be made by modeling an effective medium. There is no ρ associated with the magnetic field because there isn't a magnetic charge or monopole as far as we know. In general, the electric scalar potential is

$$\Phi(\mathbf{r}) = \frac{1}{4\pi\varepsilon_0}\int \frac{\rho_{\text{total}}(\mathbf{r}')}{|\mathbf{r}-\mathbf{r}'|}\, d^3r' \tag{2.17}$$

The bound charge will be localized in space so its integral contribution can be approximated by using a power series expansion (about equilibrium) and keeping only the lowest order terms. This is commonly referred to as a multipole moment expansion. The first term will be the electric monopole moment and can be grouped in with the free charge term. The second term will be the electric dipole moment

$$\mathbf{p} = \int \mathbf{r}' \rho_{\text{electric}}(\mathbf{r}')\, d^3 r \tag{2.18}$$

The scalar potential due to the dipole moment is

$$\Phi(\mathbf{r}) = \frac{1}{4\pi\varepsilon_0} \frac{\mathbf{p} \cdot \mathbf{r}}{r^3} \tag{2.19}$$

In some cases, it's important to keep higher order moments to accurately describe the dynamics in some materials. For example, in nuclear physics the quadrupole moment becomes important. As stated previously, this dissertation will focus on macroscopic electromagnetism due to electrons only, so the dipole approximation works very well. It's useful to define the dipole polarization $\mathbf{P}(\mathbf{r})$ as the electric dipole density. The total electric scalar potential from a small volume ΔV can then be written as

$$\Delta\Phi(\mathbf{r}) = \frac{1}{4\pi\varepsilon_0} \left(\frac{\rho_{\text{free}}(\mathbf{r}')}{|\mathbf{r} - \mathbf{r}'|} + \frac{\mathbf{P}(\mathbf{r}') \cdot (\mathbf{r} - \mathbf{r}')}{|\mathbf{r} - \mathbf{r}'|^3} \right) \Delta V \tag{2.20}$$

Now we treat ΔV as (macroscopically) infinitesimal and rearrange the second term

$$\Phi(\mathbf{r}) = \frac{1}{4\pi\varepsilon_0} \int \left(\frac{\rho_{free}(\mathbf{r}')}{|\mathbf{r} - \mathbf{r}'|} + \mathbf{P}(\mathbf{r}') \cdot \boldsymbol{\nabla}' \left(\frac{\mathbf{1}}{|\mathbf{r} - \mathbf{r}'|} \right) \right) d^3 r' \tag{2.21}$$

then

$$\Phi(\mathbf{r}) = \frac{1}{4\pi\varepsilon_0} \int \frac{\rho_{\text{free}}(\mathbf{r}') - \boldsymbol{\nabla}' \cdot \mathbf{P}(\mathbf{r}')}{|\mathbf{r} - \mathbf{r}'|} d^3 r' \tag{2.22}$$

Therefore, the second of the Maxwell's equations, Eq. (2.8), now reads

$$\nabla \cdot \mathbf{E}(\mathbf{r}) = \frac{\rho_{\text{free}} - \nabla \cdot \mathbf{P}}{\varepsilon_0} \tag{2.23}$$

This can be qualitatively explained as follows: if there is a non-uniform polarization there will be a change in the charge distribution in any small volume. By defining an electric flux density (sometimes called electric displacement) $\mathbf{D}$ (C/m^2) as

$$\mathbf{D} = \varepsilon_0 \mathbf{E} + \mathbf{P} \tag{2.24}$$

equation (2.23) can be rewritten as

$$\nabla \cdot \mathbf{D} = \rho_{\text{free}} \tag{2.25}$$

An equation for $\mathbf{J}_{\text{electric}}$ can be obtained by substituting the equation for ρ_{electric} into the continuity equation

$$\mathbf{J}_{\text{electric}} = \frac{\partial \mathbf{P}}{\partial t} = i\omega \mathbf{P} \tag{2.26}$$

To determine $\mathbf{J}_{\text{magnetic}}$, the magnetic vector potential can be treated in a similar manner as the electric scalar potential. $\mathbf{A}(\mathbf{r})$ in some unbounded space is

$$\mathbf{A}(\mathbf{r}) = \frac{\mu_0}{4\pi} \int \frac{\mathbf{J}_{\text{total}}(\mathbf{r}')}{|\mathbf{r} - \mathbf{r}'|} d^3\mathrm{r}' \tag{2.27}$$

If we split the integrals into three separate integrals, the integral containing $\mathbf{J}_{\text{magnetic}}$ can be expanded in a power series like for the electric scalar potential. The first term vanishes because there is no magnetic monopole. Thus, the first non-vanishing term will be the second term in the expansion and is called the magnetic dipole moment

$$\mathbf{m} = \frac{1}{2} \int \mathbf{r}' \times \mathbf{J}_{\text{bound}}(\mathbf{r}') d^3 r' \tag{2.28}$$

where $\mathbf{J}_{\text{bound}}$ is the current due to $\mathbf{J}_{\text{magnetic}}$ and $\mathbf{J}_{\text{electric}}$. Then $\mathbf{A}(\mathbf{r})$ can be written

$$\mathbf{A}(\mathbf{r}) = \frac{\mu_0}{4\pi} \frac{\mathbf{m} \times \mathbf{r}}{|\mathbf{r}|^3} \tag{2.29}$$

It's useful to define the dipole magnetization $\mathbf{M}(\mathbf{r})$ as the magnetic dipole density due to $\mathbf{J}_{\text{magnetic}}$ only. The total magnetic vector potential from a small volume ΔV can then be written as

$$\Delta\mathbf{A}(\mathbf{r}) = \frac{\mu_0}{4\pi}\left(\frac{\mathbf{J}_{\text{free}}(\mathbf{r}') + \mathbf{J}_{\text{electric}}(\mathbf{r}')}{|\mathbf{r}-\mathbf{r}'|} + \frac{\mathbf{M}(\mathbf{r}') \times |\mathbf{r}-\mathbf{r}'|}{|\mathbf{r}-\mathbf{r}'|^3}\right)\Delta V \tag{2.30}$$

Now we treat ΔV as (macroscopically) infinitesimal

$$\mathbf{A}(\mathbf{r}) = \frac{\mu_0}{4\pi}\int\left(\frac{\mathbf{J}_{\text{free}}(\mathbf{r}') + \mathbf{J}_{\text{electric}}(\mathbf{r}')}{|\mathbf{r}-\mathbf{r}'|} + \mathbf{M}(\mathbf{r}') \times \nabla'\left(\frac{\mathbf{1}}{|\mathbf{r}-\mathbf{r}'|}\right)\right)d^3\mathrm{r}' \tag{2.31}$$

then

$$\mathbf{A}(\mathbf{r}) = \frac{\mu_0}{4\pi}\int\left(\frac{\mathbf{J}_{\text{free}}(\mathbf{r}') + \mathbf{J}_{\text{electric}}(\mathbf{r}') + \nabla' \times \mathbf{M}(\mathbf{r}')}{|\mathbf{r}-\mathbf{r}'|}\right)d^3\mathrm{r}' \tag{2.32}$$

Therefore, the last of Maxwell's equations, Eq. (2.10), can be written as

$$\nabla \times \mathbf{B} + \frac{i\omega}{c^2}\mathbf{E} = \mu_0(\mathbf{J}_{\text{free}} + i\omega\mathbf{P} + \nabla \times \mathbf{M}) \tag{2.33}$$

or if we define the magnetic field intensity (A/m) as

$$\mathbf{H} = \frac{1}{\mu_0}\mathbf{B} - \mathbf{M} \tag{2.34}$$

and use the equation for the electric flux density Eq. (2.32) can be written as

$$\nabla \times \mathbf{H} + i\omega\mathbf{D} = \mathbf{J}_{\text{free}} \tag{2.35}$$

Thus, to a good approximation the magnetic dipole moment and the electric dipole moment will be the only significant contributions. Throughout this dissertation any higher order magnetic moments will be neglected. It should be noted that the magnetization is defined as the total magnetic moment per unit volume only when the material dimensions are small compared to the wavelength and the magnetization is uniform. At the higher frequencies, near the optical regime, the moment has contributions from $\mathbf{J}_{\text{electric}}$ as well as $\mathbf{J}_{\text{magnetic}}$[3]**.** However, all the work in this dissertation is in the microwave frequency regime or lower and the magnetization is mostly

uniform, so to a good approximation the magnetization can be defined as the magnetic moment per unit volume.

So far, approximations have been made for the bound charge and bound current densities by treating matter as a macroscopic medium and using a multipole expansion keeping terms through second order. The bound charge and current densities describe the interactions of particles, or rather the losses, in a material in response to electromagnetic fields in matter. It's also been assumed that the magnetization is uniform and the frequency is small enough to define the magnetization as the magnetic moment density. The case of non-uniform magnetization will be treated as a perturbation later in the dissertation when the need arises. Often, it is necessary to assume relationships between **H** and **B**, **D** and **E**, and even **E** and **B** with $\mathbf{J}_{\text{free}}$ as well.

$$\mathbf{B} = \bar{\mu}\mathbf{H} \tag{2.36}$$

$$\mathbf{D} = \bar{\varepsilon}\,\mathbf{E} \tag{2.37}$$

$$\mathbf{J}_{\text{free}} = \sigma(\mathbf{E} + \mathbf{v} \times \mathbf{B}) \tag{2.38}$$

where $\bar{\mu}$ is an effective permeability tensor, $\bar{\varepsilon}$ is an effective permittivity tensor, and σ is the electrical conductivity tensor ($\Omega^{-1}m^{-1}$). To a good approximation, these relationships can be assumed to be linear. This linear approximation often breaks down when the current densities become large.

Once the total charge and current densities are known, the electromagnetic fields can be determined. However, even though these approximations allow for more simple interpretations and calculations of the electromagnetic fields, it can be very challenging to write down analytic equations for the total charge and current densities because of complicated electron trajectories in atoms and materials. Other methods are often used in conjunction with Maxwell's equations to circumvent the need to know the total charge and current densities explicitly. In the next section,

the analysis above is built on by looking at the response of the magnetic moment from a single electron (and then many electrons) to a magnetic field.

2.3 Landau-Lifshitz equation

It can be shown that the magnetic dipole moment of a single electron is approximately[4,5]

$$\mathbf{m} = \frac{ge}{2m_e}\boldsymbol{\mathcal{J}} = -|\gamma|\boldsymbol{\mathcal{J}} \tag{2.39}$$

where e is the unit of fundamental charge (negative), g is a dimensionless correction factor, m_e is the mass of the electron, $\boldsymbol{\mathcal{J}}$ is the total angular momentum of the electron that includes orbital and spin vectors $\boldsymbol{\mathcal{J}} = \mathbf{L} + \mathbf{S}$, and γ is defined as the angular gyromagnetic ratio. Classical derivations of this equation do not include the dimensionless correction factor. This correction can be obtained from the Dirac equation, a fundamental quantum mechanical equation that connects the electron spin with its electromagnetic properties. Reduction of the Dirac equation for an electron in a magnetic field to its non-relativistic limit yields the Schrödinger equation with a correction term. A further correction from interactions with virtual photons (not considered in the Dirac equation) by considering all possible electromagnetic interactions using a complete theory of quantum electromagnetism gives a more accurate value. The actual value of g depends on the spin and orbital contributions to $\boldsymbol{\mathcal{J}}$. For example, if due to spin alone, the value is close to 2.002. A relationship between a single magnetic moment and magnetic flux can be obtained classically by examining the torque on a magnetic moment or quantum mechanically by using the quantum kinetic equation. Even in the case of non-electrically insulating materials such as Fe or Co, the total contribution from $\mathbf{L}$ is typically small.

2.3.1 Classical derivation of Landau-Lifshitz equation

The torque on a magnetic moment due to a magnetic flux is

$$\boldsymbol{\tau} = \mathbf{m} \times \mathbf{B} \tag{2.40}$$

According to Newton's second law, this torque can lead to a change in angular momentum as

$$\boldsymbol{\tau} = \frac{d\boldsymbol{\mathcal{J}}}{dt} \tag{2.41}$$

Combining these equations and replacing **B** with **H** leads to what is known as the Landau-Lifshitz (LL) equation of motion

$$\frac{d\mathbf{m}}{dt} = -\mu_0|\gamma|\mathbf{m} \times \mathbf{H} \tag{2.42}$$

Now if the approximation from the previous section for the relationship between the magnetic moment and magnetization is applied and uniform magnetization is assumed, one can rewrite Eq. (2.42) as

$$\frac{d\mathbf{M}}{dt} = -\mu_0|\gamma|\mathbf{M} \times \mathbf{H} \tag{2.43}$$

2.3.2 Quantum derivation of Landau-Lifshitz equation

An alternative method for arriving at the LL equation is to use the quantum kinetic equation (or the Heisenberg equation). This microscopic equation

$$\frac{d}{dt}\langle\mathbf{Q}\rangle = \frac{i}{\hbar}\langle[H, \mathbf{Q}]\rangle + \langle\frac{\partial\mathbf{Q}}{\partial t}\rangle \tag{2.44}$$

can be obtained in a linear, non-relativistic scheme by computing the time derivative of an expectation value of some observable, $\mathbf{Q}(\mathbf{x}, \mathbf{p}, t)$. Here, H is the Hamiltonian for the system and $\hbar$ is the reduced Planks constant. As in the classical case, if only the interaction of a magnetic moment from a single electron is considered in the presence of a magnetic field, the Hamiltonian can be written as

$$H = -\mathbf{m} \cdot \mathbf{B} \tag{2.45}$$

This is a well-known quantum mechanical result obtained by considering only the angular motion of an electron in a magnetic field, commonly referred to as the Zeeman interaction. By letting **Q**

be the magnetic flux and averaging over many electrons (again assuming no interaction), the same result is obtained as in the classical case.

This macroscopic equation provides additional information about the response of the magnetization to a magnetic field. However, though this equation applies to a macroscopic media, it has neglected an interaction between the moments and any motion of electrons through the medium. Another way to say this is that it only partially takes into consideration the charge and current densities. Thus, this equation does not account for the losses. In order to complete this equation something must be said about the relationship between neighboring magnetic moments. In the next section, magnetic ordering in materials is categorized based on the response of moments to a magnetic field, among other things. Once the ordering is identified and thus the possible energy transfer mechanisms (losses) are identified for a particular material, a term can be phenomenologically identified and added as a damping term to the LL equation. This is a convenient way of addressing the losses in a material without explicitly stating the charge and current densities. To identify these scattering mechanisms, a Hamiltonian is constructed for the likely interactions so that probability of interaction, or relaxation, times can be identified. This allows for a more correct choice of a phenomenological damping term.

2.4 Introduction to magnetic ordering

As previously mentioned in chapter 1.1, in some materials the collective motion of electrons can produce permanent magnetic behavior in materials that are deemed ‘magnetic materials’. This behavior is often referred to as magnetic ordering. Magnetic materials are placed into one of five major categories based on several criteria involving their magnetic moments. These five categories are diamagnetic, paramagnetic, ferromagnetic, ferrimagnetic, and antiferromagnetic as shown in Fig. 2.1.

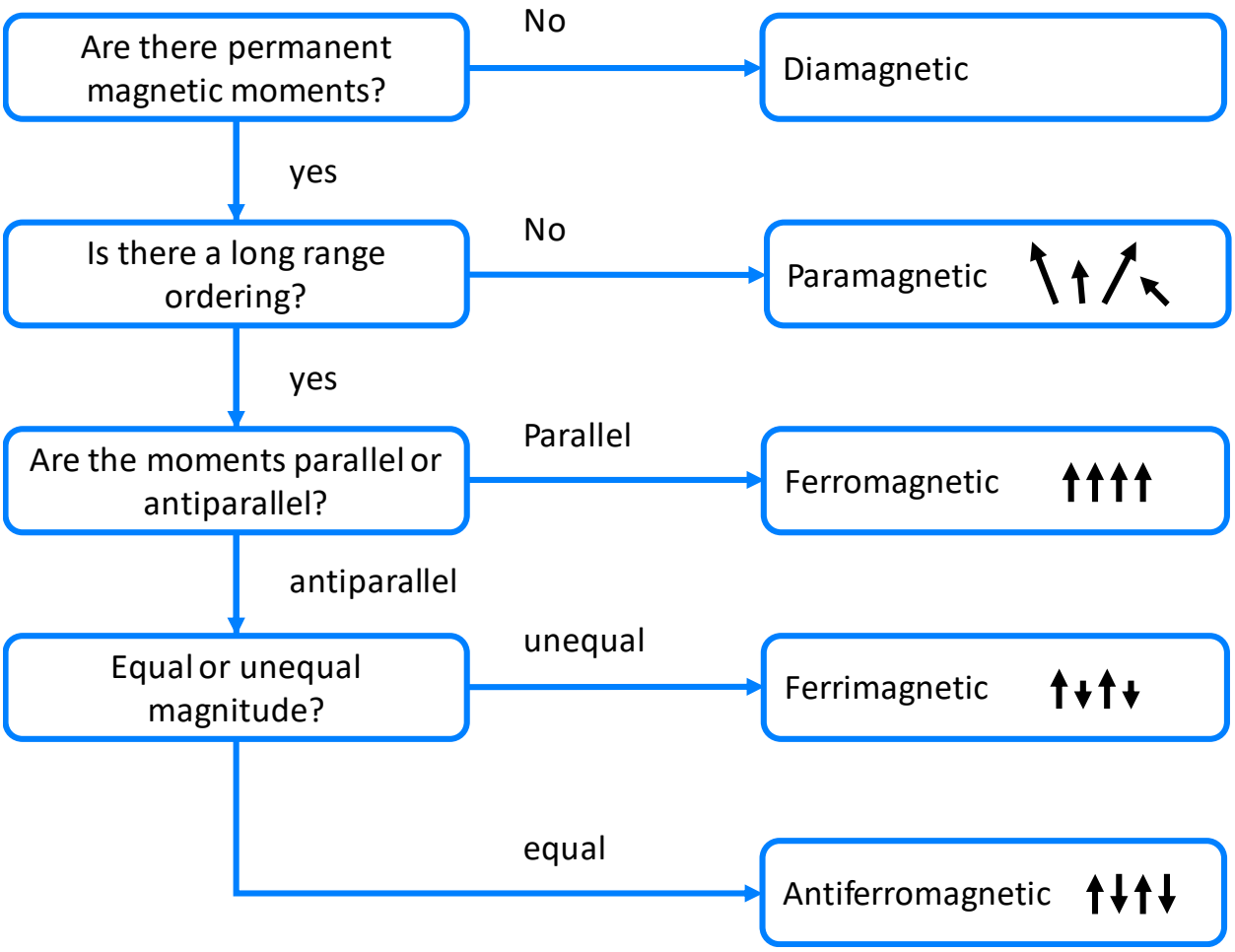

Fig. 2.1. Process for categorizing magnetic materials.

First, if the material doesn't possess a permanent magnetic moment (there is no net angular momentum from unpaired electrons) it is classified as diamagnetic. In the presence of an external magnetic field, the electrons will reorient themselves such that their moments will produce an opposing magnetic field. This phenomenon can be explained by Lenz's law. Virtually every material will have some diamagnetic contribution, even those that fit into one of the other four categories, though it will be much smaller than their other respective category's contribution.

Second, if the material has a permanent magnetic moment but doesn't have a long-range ordering it is classified as paramagnetic. In the presence of an external magnetic field the moments will align themselves with the magnetic field. However, when the external field is removed, the

moments will randomly orient themselves. Above or below certain temperatures and pressures, the ferromagnetic, ferrimagnetic, and antiferromagnetic materials will undergo a phase change to become paramagnetic.

Third, if the motion of the electrons between neighboring atoms couple very strongly to one another via the exchange and dipolar interactions there will be long range ordering, and thus even in the absence of an external magnetic field the moment will align along a particular direction. This type of ordering is called ferromagnetic ordering.

The last two types of ordering are a bit more complicated. Similar to ferromagnetic materials, the coupling between neighboring atoms is very strong. However, it is possible that given the right crystal structure, neighboring atoms will have moments in opposite directions of one another. In the case that the opposite moments result in a zero net magnetization, one has antiferromagnetic ordering. If the antiparallel moments have different magnitudes and thereby give rise to a nonzero net magnetization, one has ferrimagnetic ordering. In the next section, several types of common energy transfer mechanisms are identified for ferromagnetic and ferrimagnetic materials and their microscopic origins are discussed.

2.5 Introduction to energy transfer mechanisms

So far, a variety of terms have been used to describe the transfer of energy. These include scattering, relaxation, loss, dissipation, and damping. These terms are more or less equivalent but for conventional reasons each term is used when describing different circumstances. Sometimes the LL equation is referred to as lossless. This is misleading as there is still power radiated from the fields, and though explicit interactions between moments is neglected, the total magnetic field may have contributions from nearby moments. The term ‘lossless’ refers to the fact that the

magnetization will continue to process about the magnetic field indefinitely, instead of relaxing to align itself with the field.

It's useful to describe quantized interactions or scattering with particles that possess quantized units of magnetic moment, momentum, charge, mass, etc. For example, the photon was mentioned in a previous section, and is the quantized force carrier particle for the electromagnetic force. It is convenient to define a quasi-particle called a magnon that describes a decrease in one unit of magnetization of $2\mu_B$ and a decrease in one unit of spin of $\hbar$. Here μ_B is defined as the Bohr magneton. Another type of quasi particle that will be discussed is the phonon, which is the quantized interaction of lattice vibrations. Both are bosonic particles in nature. Subsequently, interactions will be described in terms of interactions between photons, magnons, phonons, and electrons. Interactions of these particles must conserve momentum, energy, magnetization, etc. Very often momentum and energy are described in terms of wave vector and frequency, respectively.

2.5.1 Common types of interactions

This section describes the most common types of relaxation processes and provides a brief description for each process in which energy is transferred away from the magnetic moments when they are excited away from equilibrium by some external fields (photons). The frequency of the photons is chosen such that the magnetization is excited but other dynamics are not due to resonance phenomenon of the magnetization. It's important to note that ultimately the energy will end up as heat from lattice vibrations. For example, if the most likely energy transfer mechanism is some type of magnon-electron scattering, the energy of the electrons will then be transferred to the crystal structure afterward as lattice vibrations. However, this dissertation will focus on energy

transferred away from the magnetic moments, not subsequent processes. The subsequent processes won't influence the magnetization dynamics any noticeable amount.

Magnon-phonon processes typically dominate in materials that are electrically insulating. This is the process by which magnons scatter with lattice vibrational modes[6]. This can be due to direct scattering between one or more magnons and phonons, impurities in a lattice, or degeneracies in electron orbits. The impurities can be isotropic or anisotropic which lead to fast or slow relaxation, respectively. The nature of the degenerate electron orbits depends on the elements in the lattice. For example, if there are Fe^{2+} and Fe^{3+} ions at equivalent lattice sites, like in some magnetic materials, there will be a hopping of a 3d electron between the two sites. Though there is an electron in motion, it is localized and can still be considered electrically insulating. An illustration of scattering between one or more magnons and phonons is shown in Fig. 2.2.

Magnon-electron processes typically dominate in materials that are electrically conducting, though there will still be some magnon-phonon scattering. Magnon-electron scattering is the process in which one or more magnons scatter with electrons directly. This includes the flow of conduction electrons due to spin-orbit coupling (Eddy currents), spin-flip scattering, and breathing Fermi-associated scattering. At low temperatures where electron states are more discretized, the

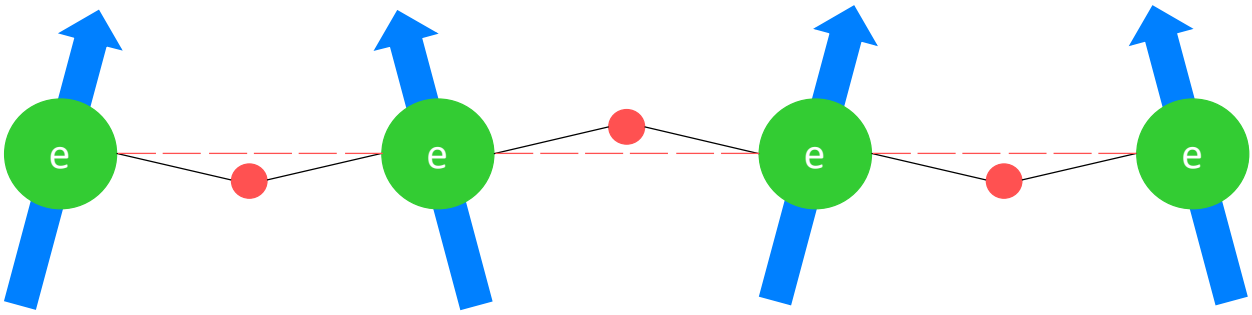

Fig. 2.2. Illustration of magnon phonon scattering. The green circles and blue arrows indicate electrons and magnetic moments, respectively, and the red dots and black lines indicate the lattice or phonon coupling. The electron moments are highly coupled to the lattice and thus changes in the moment direction will influence the phonon coupling.

breathing Fermi surface scattering, or intraband scattering, is more likely to occur. This involves the modification of electron states above and below the Fermi level due to scattering with magnon, and as the name suggests, the Fermi level will be modified. The spin-flip scattering, or interband scattering, is more likely to occur at higher temperatures where the broadening of the Fermi level leads to flipping of electron spins. Kambersky, in addition to several others, studied the relaxation times for several materials in great detail and found that to first order the breathing Fermi surface showed a $\frac{1}{T^2}$ dependence while the spin-flip scattering showed a T^2 dependence, where T stands for absolute temperature[7,8,9,10]. It's important to note that the total relaxation time depends on the probability of occurrence as well as the relative 'strength' of each mechanism. The theory was in good agreement with some experiments performed for iron, cobalt, and nickel. Figures 2.3(a) and

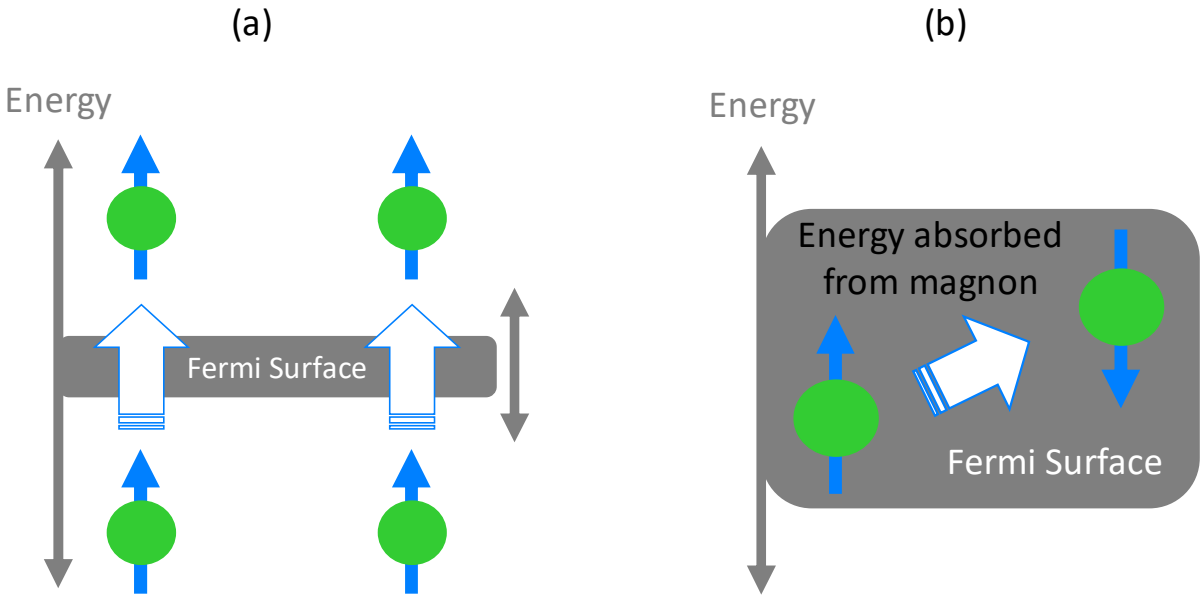

Fig. 2.3. Description of the two types of magnon electron scattering. (a) The breathing Fermi surface scattering. Via spin-orbit coupling, the scattering changes the energy of the free electron states. This pushes some of the free electrons above the Fermi level, effectively creating occupied states above and unoccupied states below in different energy bands. This energy will eventually be transferred to the lattice and the free electrons will move back to their original states. This causes the Fermi surface to move up and down or 'breathe'. (b) The spin-flip scattering. At higher temperatures the Fermi surface isn't clearly defined and begins to broaden. It becomes more likely to see scattering between the bands than within the bands. Electrons within this region will absorb energy from the magnons, flip their spin, and move to a higher energy with the Fermi surface.

2.3(b) illustrates these two types of magnon-electron scattering. Eddy currents are common in thicker materials but typically negligible in thinner materials as the damping should go with the square of the thickness[11]. It's essentially the process by which electrical currents are created in a material that produce electromagnetic fields that restrict the magnetization from processing. They won't be discussed in detail here because only thin metallic materials are discussed in this dissertation.

Magnon-magnon scattering refers to any type of scattering between two or more magnons. The three most common types are two, three, and four magnon scattering. Conservation of the momentum allows for scattering of magnons with different wave numbers and this can involve two or more magnons depending on the circumstance[12,13]. It's also possible to have anisotropy induced two magnon scattering in materials with strong anisotropy[14]. It's also common to have

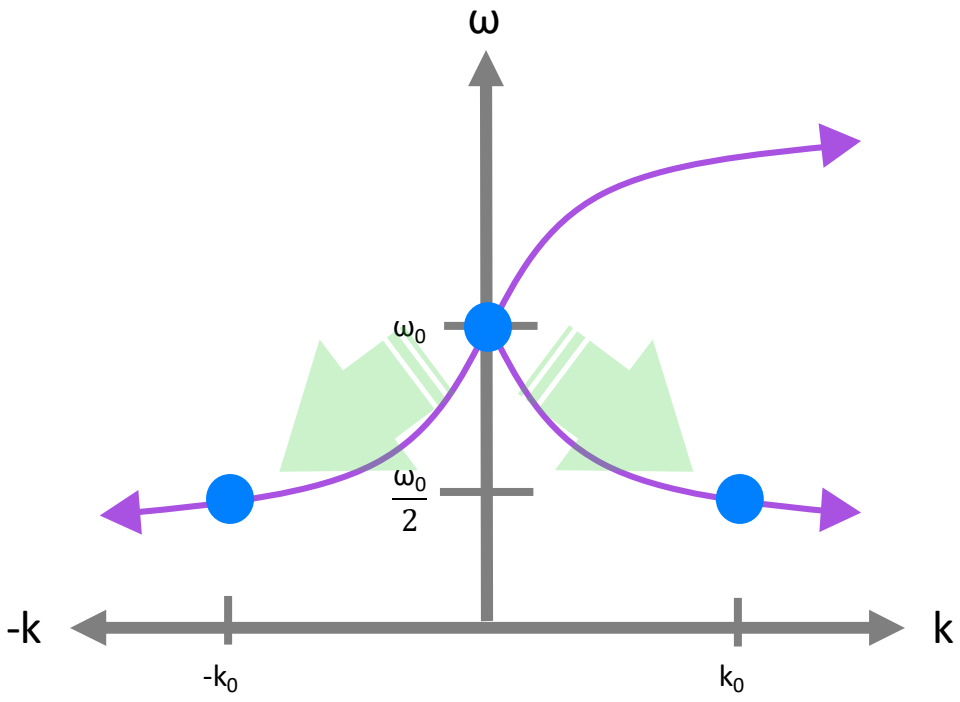

Fig. 2.4. An example of a three magnon splitting process. The purple curves represent possible dispersion (ω vs. k) curves for a case where a magnon in the surface wave configuration splits into two backward volume wave magnons. These spin wave configurations are discussed in detail in section 2.6. Here a ($\omega=\omega_0$, $k=0$) magnon splits into two magnons each with $\omega=\omega_0/2$ but with different k values of k_0 and $-k_0$.

large two magnon scattering due to inhomogeneities in a material. Sample dimensions, magnetization orientation, frequency, and the power will play important roles in the types of magnon-magnon scattering allowed. Figure 2.4 illustrates an example of a three magnon splitting process. Lastly, it's possible to have external influence on the system where energy flows in or out. One common example of this is spin pumping (Ch. 6) where angular momentum flows out of a magnetic layer into an adjacent, typically nonmagnetic, layer. An additional damping term is needed in order to describe these types of external influences that are specific to a given situation.

2.5.2 Hamiltonian formalism for identifying dominant mechanisms

Much work has been done over the years to write a Hamiltonian to describe the above interactions whereas the probability of occurrence and the relaxation time can then be determined. They treat Hamiltonians as perturbations to the system and solve for a specific interaction. It's important to note that the Hamiltonians are used in the linear, non-relativistic Schrödinger equation. Nonlinear or relativistic damping considerations will be neglected as their contributions are negligible. Though the Hamiltonian formalism is correct and gives detailed information about a system, it can be more useful to use the insight gained from this method and choose a phenomenological damping term to add to the LL equation for studying macroscopic interactions.

2.5.3 Common phenomenological damping terms

A lot of information is buried within each scattering mechanism. For example, Magnon-electron scattering conserves magnetization but two magnon scattering does not. Several common relaxation terms, the scattering it attempts to describe, and useful information for each are given below.

Historically, Landau and Lifshitz, when first deriving the LL equation suggested a damping term[15].

$$\frac{-\mu_0|\gamma|\lambda}{M_s}\mathbf{M}\times(\mathbf{M}\times\mathbf{H}) \tag{2.46}$$

where λ is a unitless damping parameter and is assumed to be frequency independent. It was designed so that the magnetization would be conserved during the procession and the magnetization would eventually align with the magnetic field since this is what early experiments were indicating. It was an attempt to describe magnon-electron and magnon-phonon scattering since magnon-magnon interactions do not conserve the magnetization. It was an excellent first attempt but fails to accurately describe the magnetization dynamics in several ways. Most notably, the trajectory of the precession is unaffected by the damping and actually causes the magnetization to increase[16]. This leads to a decrease in switching time with an increase in damping. For small damping though, this term works okay, and these effects aren't very noticeable.

Like Landau and Lifshitz, Gilbert wanted to come up with a damping term in which magnetization is conserved and the magnetization relaxes to align with the magnetic field. Thus, his term can describe magnon-electron scattering and magnon-phonon scattering as well. However, the Gilbert term has a more physical origin and more accurately describes the dynamics observed experimentally[17]. The Gilbert damping term is

$$\frac{\alpha}{M_s}\mathbf{M}\times\frac{d\mathbf{M}}{dt} \tag{2.47}$$

where α is a unitless damping parameter and is assumed to be frequency independent. Gilbert considered the Rayleigh dissipation force function where a conservative or non-conservative force, linear in velocity, is applied to a system. It would be possible to include higher order terms in velocity. This has been used successfully in many classical systems to describe damping. α is originally assumed to be a tensor but to simplify the description it is reduced to a constant. He later applies a conservation of magnetization restriction when constructing a Lagrangian to determine

an equation of motion, and thus magnon-magnon scattering is then prohibited. To date, his model seems to be the most appropriate for describing magnon-electron and magnon-phonon scattering in magnetic materials. When the Gilbert term is added to the LL equation it is often called the Landau-Lifshitz Gilbert (LLG) equation. It's worth noting that though this model may not be the most appropriate model at high temperatures, there are a few papers that have applied the LLG model to describe the dynamics at high temperatures[18,19].

Though originally designed for paramagnetic systems and nuclear resonance phenomenon, Bloembergen and Bloch suggested time relaxation terms to describe a two-step process[20].

$$-\frac{1}{2T_1}(M_z - M_s)\,\hat{z} \tag{2.48}$$

$$-\frac{1}{2T_2}\left(M_{x,y}\right)\hat{x},\hat{y} \tag{2.49}$$

The two-step process allows for some magnon-magnon scattering processes in which the magnetization is not conserved but the other types of scattering can't be described by this model. This could describe two-magnon scattering due to inhomogeneities or magnon-magnon scattering when a material is heated and approaches the paramagnetic phase at the Curie temperature. Two other damping models, the self-consistent Bloch (SCB) and the Grobis terms have been suggested for modeling granular, large anisotropy materials near the Curie temperature[21,22]. Those models

$$-\frac{1}{\tau_s}\left(\mathbf{M} - \mathbf{M}_{eq}\right) \tag{2.50}$$

$$-\frac{1}{\tau_s}(\mathbf{M} - \mathbf{M}_0) \tag{2.51}$$

for the SCB and Grobis, respectively, differ from the Bloembergen Bloch (BB) model in the definition of the equilibrium state of the magnetization and slight variations in the spin dependent relaxation. Interestingly, all three have similar physical origins but are derived in very different

ways. The BB model was purely conceptual, the SCB was based on a spin dependent relaxation using the quantum kinetic equation, and the Grobis was derived using a spin dependent relaxation and the statistical Fokker-Plank equation. It's important to note that the SCB and Grobis models attempt to describe magnon-electron and magnon-phonon scattering as well to some extent. Also, the time relaxation parameters are not assumed to be frequency independent.

The need for a damping term near the Curie temperature of a ferromagnetic material is what brought about the SCB and Grobis damping terms. Heat assisted magnetic recording (HAMR) is a magnetic recording technology still in development that reads and writes at temperatures near the Curie temperature as illustrated in Fig. 2.5. As such, damping at elevated temperatures becomes very important. Another popular model uses the Landau-Lifshitz Bloch equation (LLB) damping term[23,24,25].

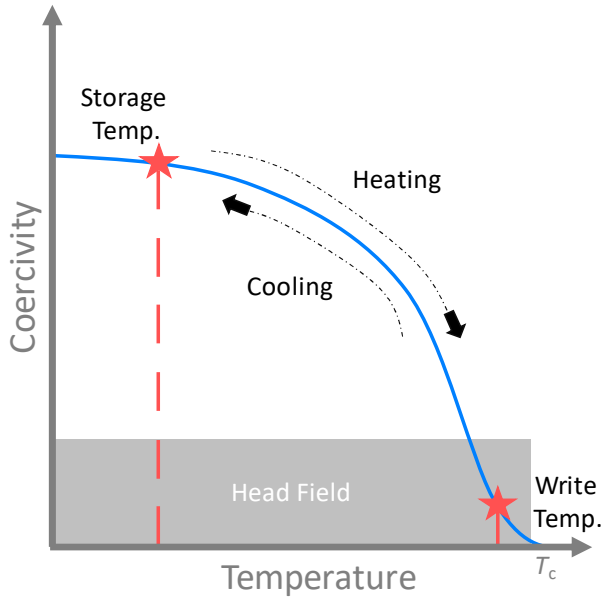

Fig. 2.5. A description of HAMR media reading and writing process. The coercivity is defined as the field at which zero magnetization is reached. As the media is heated from the storage temperature up to the write temperature, the coercivity is drastically reduced so that the head field available can read or write information. The media is then cooled back to the storage temperature. Because the coercivity is so large at the storage temperature, the media is more thermally stable which allows for greater areal density.

$$\frac{\mu_0|\gamma|\alpha_{||}}{M_s^2}\mathbf{M}(\mathbf{M}\cdot\mathbf{H}) - \frac{\mu_0|\gamma|\alpha_{\perp}}{M_s^2}\mathbf{M}\times(\mathbf{M}\times\mathbf{H}) \tag{2.52}$$

The α terms are unitless longitudinal and transverse damping parameters and are frequency independent. They can be related to the temperature if a small external field limit is applied. Though this damping term is very popular, it has physical problems as mentioned in the papers by Grobis and Zhang, *et al*. The biggest problem is that its derivation assumes a constant atomic damping which is known to be unphysical. The Grobis model is probably the most appropriate model for describing the dynamics of granular media at elevated temperatures near the Curie temperature. Each of these models makes several assumptions involving uniform temperature and magnetic properties throughout the grains. These models begin to break down as the grains become very small on the order of a few nanometers.

Several terms have been suggested to account for the stochastic thermal fluctuations as well. Those won't be discussed in detail here as they aren't relevant to the experiments in the later chapters. It's important to note that all the damping parameters are assumed to be temperature dependent. Typically, these damping parameters are identified by performing ferromagnetic resonance (FMR) measurements as will be discussed in the next sections.

2.6 Spin Waves

A spin wave is defined as the collective motion of the magnetic moments in a material and, as previously mentioned, the quantized interactions of spin waves are referred to as magnons. So far, though magnetic ordering and interactions have been discussed, the physical mechanisms behind the ordering have not. Several common magnetic interactions that lead to ordering are discussed in detail below.

2.6.1 Quantum mechanical formalism

Because electrons are classified as fermions, they obey the Pauli exclusion principle, which has important implications that dictates how atoms organize and share electrons. The exclusion principle dictates that the overall quantum mechanical wavefunction be antisymmetric when two electrons are shared or exchanged. This requires two electrons with the same orbital angular momentum to occupy different spin states. This can also be understood in that two electrons, for example, will be spatially further apart if they possess spin (or moments) in the same directions, thus minimizing the electrostatic energy (principle of least action). So the energetically preferred state is the alignment of moments and it's called the exchange interaction. The interaction is normally short ranged and only affects the nearest neighbor spins, but it's possible to have indirect types of coupling. The direct exchange interaction Hamiltonian to first order is given as

$$H_{\text{ex}} = -\frac{1}{2} J_{\text{ex}} \sum_{i,j} \langle \mathbf{S}_i \cdot \mathbf{S}_j \rangle \tag{2.53}$$

where J_{ex} is the exchange constant and is related to the energy associated with the separation between two electrons. The factor of $\frac{1}{2}$ is needed for the double counting done in the summation. Note that if the sign of J_{ex} is flipped, this describes antiferromagnetic ordering and neighboring moments will energetically prefer antialignment.

Another interaction that strongly affects ordering is the magnetic dipole-dipole interaction. As the name suggests, it's the interaction between dipole moments and is a longer-range interaction than the exchange interaction. The dipole interaction, unlike the ferromagnetic exchange interaction, prefers the antialignment of the moments. To minimize the energy of, say two dipole moments aligned with each for example, one dipole would prefer to switch to the other direction.

A factor of $\frac{1}{2}$ is again included to account for the double counting done by the summation. It's Hamiltonian to first order is given by

$$H_{\text{dip}} = \frac{1}{2}\sum_{i,j}\frac{1}{{R_{ij}}^5}\left({R_{ij}}^2(\mathbf{m}_i \cdot \mathbf{m}_j) - 3(\mathbf{R}_{ij} \cdot \mathbf{m}_i)(\mathbf{R}_{ij} \cdot \mathbf{m}_j)\right) \tag{2.54}$$

where R is the separation between two moments.

Next is the magneto-crystalline anisotropy interaction. If the orbit of an electron is not spherically symmetric, the energy of the state of the electron will depend on the orientation of the orbital with respect to the neighboring ions. This will create a preferred direction (to minimize energy) of the magnetization. It's Hamiltonian depends on the type of magneto-crystalline anisotropy. It's common in hard drive media to have uniaxial anisotropy along a particular axis. There are other types of magnetic anisotropic interactions, but all can essentially be described by preferred direction of magnetization based on the surroundings of a moment. Though an equation can be derived for a specific case, it's often necessary to experimentally determine the magnetic field associated with this interaction.

The last notable interaction is the Zeeman interaction, which has already been discussed in some detail. In the presence of a magnetic field, the magnetic moments will precess about the magnetic field. The Zeeman interaction Hamiltonian to first order is given by

$$H_{\text{zeeman}} = -\sum_i \mathbf{m}_i \cdot \mathbf{B} \tag{2.55}$$

Many years ago, Holstein and Primakoff *et al*. derived many useful relationships, including a dispersion relation and magnon-magnon scattering relations, using these (excluding magneto-crystalline anisotropy) magnetic interactions when studying the microscopic dynamics[26]. In the next section these interactions are discussed in detail on the macroscopic scale, where things can be modeled using effective media and the useful relations from chapter 1 can be applied.

2.6.2 Classical formalism

The exchange, dipolar, and anisotropy energy terms have a magnetic field associated with their interactions. The Zeeman interaction doesn't have one as it doesn't describe interactions between moments but rather is a response to a field itself. These, with the addition of any external fields, will define the total field and can have time and spatial dependence.

$$\mathbf{H}(\mathbf{r},t) = \mathbf{H}_{\text{ext}}(\mathbf{r},t) + \mathbf{H}_{\text{ex}}(\mathbf{r},t) + \mathbf{H}_{\text{dip}}(\mathbf{r},t) + \mathbf{H}_{\text{anisotropy}}(\mathbf{r},t) \tag{2.56}$$

The magnetic field (and the other fields) can be split into a time varying component and a static component

$$\mathbf{H}(\mathbf{r},t) = \mathbf{H}_0 + \mathbf{h}(\mathbf{r},t) \tag{2.57}$$

where $\mathbf{H_0}$ is the static component and is assumed to be position independent since spatial uniformity is assumed, and $\mathbf{h}(\mathbf{r},t)$ is the time varying component. The macroscopic dipole-dipole field, often called the demagnetization field, and the anisotropy field will have small time varying contributions and can be neglected. This may not be the case for some nonlinear spin wave dynamics when large power is used as discussed in a later section. In order to determine the

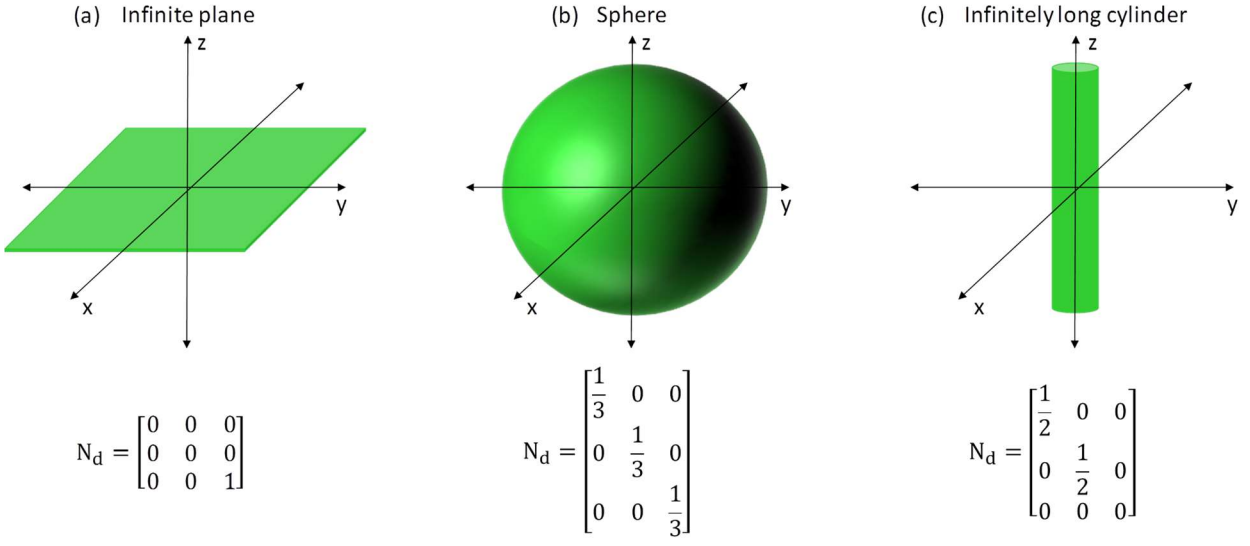

Fig. 2.6. Examples of demagnetization factors for three common geometries. (a) Demagnetization factors for an infinite plane. (b) Demagnetization factors for a sphere. (c) Demagnetization factors for an infinitely long cylinder.

demagnetization field, a demagnetization tensor must be determined for a particular geometry using Maxwell's equations and the appropriate boundary conditions given below[27].

$$\mathbf{H}_{\mathrm{dip}}(\mathbf{r},t) \equiv \mathbf{H}_{\mathrm{demag}}(\mathbf{r},t) = \mathrm{N_d}\mathbf{M} = \begin{bmatrix} N_{\mathrm{xx}} & N_{\mathrm{xy}} & N_{\mathrm{xz}} \\ N_{\mathrm{yx}} & N_{\mathrm{yy}} & N_{\mathrm{yz}} \\ N_{\mathrm{zx}} & N_{\mathrm{zy}} & N_{\mathrm{zz}} \end{bmatrix} \mathbf{M} \tag{2.58}$$

Where N_{ij} are the demagnetization factors. This is valid for shapes that can be defined for ellipsoid classes of geometries. Figure 2.6 shows several common geometries that are often solved for in many textbooks. Normally, the static components are treated as spatially uniform. This works well for materials with uniform properties and where the boundaries weakly influence the bulk dynamics as mentioned previously.

Two different methods have been used to study the dynamics in spin waves. The first is applying the magnetostatic approximation to Maxwell's equations and the second is solving the eigenvector problem of the LL equation using an approximation. Each method provides slightly different information, and the two methods need to be used together to obtain a more complete understanding of the physics. Also, it's relatively easy to arrive at a set of electromagnetic boundary conditions for Maxwell's equations, valid for static or time varying fields. For macroscopic media they are given as

$$\mathbf{n}_{21} \cdot (\mathbf{D}_2 - \mathbf{D}_1) = \Sigma \tag{2.59}$$

$$\mathbf{n}_{21} \times (\mathbf{E}_2 - \mathbf{E}_1) = 0 \tag{2.60}$$

$$\mathbf{n}_{21} \cdot (\mathbf{B}_2 - \mathbf{B}_1) = 0 \tag{2.61}$$

$$\mathbf{n}_{21} \times (\mathbf{H}_2 - \mathbf{H}_1) = \mathbf{K} \tag{2.62}$$

where $\mathbf{n_{21}}$ is the unit vector normal to the surface directed from region 1 to region 2, Σ is the surface charge density, and $\mathbf{K}$ is the surface current density**.** By assuming a plane wave solution to Maxwell's equation of the form $e^{-i\mathbf{k}\cdot\mathbf{r}}$ (recalling the uniqueness theorem), one can write

$$\mathbf{k} \times \mathbf{h} = -\omega \bar{\varepsilon} \mathbf{e} \tag{2.63}$$

$$\mathbf{k} \times \mathbf{e} = \omega \mu_0 (\mathbf{h} + \boldsymbol{m}) \tag{2.64}$$

where $\mathbf{e}$ is the time varying component of the electric field, $\boldsymbol{m}$ is the time varying component of the magnetization and $\mathbf{k}$ is the wavevector defined by

$$k = \frac{2\pi}{\lambda} \tag{2.65}$$

where λ is the wavelength. It can be shown that the wavevector in free space is given by

$$k_0^2 = \omega^2 \mu_0 \varepsilon_0 \tag{2.66}$$

Combining Eqs. (2.63), (2.64), and (2.66) yields

$$\hat{\mathbf{k}} \times \mathbf{h} = \frac{k_0^2 (\hat{\mathbf{k}} \times \boldsymbol{m})}{k_0^2 - k^2} \tag{2.67}$$

When the wavevector in free space is much larger or much smaller than the wavevector in the medium one has

$$\boldsymbol{\nabla} \times \mathbf{h} = 0 \tag{2.68}$$

$$\boldsymbol{\nabla} \cdot \mathbf{b} = 0 \tag{2.69}$$

where $\mathbf{b}$ is the time varying component of the magnetic flux. This is known as the magnetostatic approximation and is valid for the experiments done in this dissertation. Now it's useful to define a magnetic scalar potential

$$\mathbf{h} = -\boldsymbol{\nabla} \psi \tag{2.70}$$

such that

$$\boldsymbol{\nabla} \cdot (\bar{\mu} \cdot \boldsymbol{\nabla} \psi) = 0 \tag{2.71}$$

It's also useful to define a susceptibility tensor for magnetization $\bar{\chi}$

$$\mathbf{h} = \bar{\chi} \boldsymbol{m} \tag{2.72}$$

so

$$\bar{\mu} = \mu_0(\mathrm{I} + \bar{\chi}) \tag{2.73}$$

where I is the identity matrix. Combining Eqs. (2.68)-(2.73) yields what is commonly referred to as Walker's equation

$$(1 + \chi_{xx})\frac{\partial \psi^2}{\partial^2 x} + \left(1 + \chi_{yy}\right)\frac{\partial \psi^2}{\partial^2 y} + \frac{\partial \psi^2}{\partial^2 z} = 0 \tag{2.74}$$

where under most circumstances $\chi_{xx} = \chi_{yy}$ (and all circumstances in this dissertation). One of the great things about this analysis is that nice equations can be obtained for all the fields (when applying boundary conditions), but an analytic equation for the susceptibility and a dispersion relation (ω vs. k) cannot. They can however, be numerically or graphically obtained exactly. It is still not feasible to obtain an analytic equation with Maxwell's equations alone, which makes studying the dynamics time consuming and challenging.

Thankfully, an analytic equation for the susceptibility terms and an approximate dispersion relation can be obtained from the LL equation using the electromagnetic boundary conditions. Approximate here means a mathematical approximation to the model, not a physical assumption of the system. Even though this method only gives approximate solutions to the dispersion relation (and electromagnetic fields), it gives physicists something more tangible to work with. The Landau-Lifshitz equation can be written as an infinite sum of eigenvalues and eigenvectors which is why it must be approximated mathematically[28]. Lastly, to solve this equation an equation for the exchange field is needed. The static portions are position independent constants and the time varying components of the anisotropy and demagnetization fields are negligible. There is a static contribution to the exchange field that is proportional to the magnetization, but this term will not contribute because of the cross product. The time varying component to first order is

$$\mathbf{h}_{\mathrm{ex}}(\mathbf{r}, t) = A\boldsymbol{\nabla}^2\boldsymbol{m}(\mathbf{r}, t) \tag{2.75}$$

where A is an exchange constant. Lastly, while damping is considered, the equation is linearized, and the damping terms drop out because they are not linear in the magnetization. So while damping does influence the dispersion relation, it is a very small contribution.

Spin waves are often separated into 3 categories defined by the direction of an external DC magnetic field and an external AC magnetic field with respect to the material dimensions. Spin waves are typically studied in thin films where the thickness is small enough such that the in-plane dimensions can be considered infinite when compared with the thickness. Lastly, for the 3 types of waves that are about to be described, the analysis is valid for a dielectric/ferromagnet/dielectric layered structure. If a conductor, for example, was substituted in place of the dielectric, this would change the boundary conditions and the descriptions below would change to a certain degree. This is because there would be strong reflections from the surface of the conductor.

2.6.3 Forward volume waves

This first type of wave has an external DC magnetic field perpendicular to the sample plane with a wavevector k in the plane of the sample. A few key points about these types of waves:

1. It's possible to have different thickness modes where each higher order mode has a location throughout the thickness where the magnetic scalar potential is zero, similar to standing waves. Unlike other guided electromagnetic (EM) waves, all modes have the same cutoff frequency to first order in the exchange interaction.
2. The dispersion relation to first order for the 0^{th} order thickness mode is

$$\omega^2 = \omega_0\left(\omega_0 + \omega_{\mathrm{M}}\left(1 - \frac{1 - e^{-k_{\mathrm{t}}d}}{k_{\mathrm{t}}d}\right)\right) \tag{2.76}$$

with k_t as in the in-plane wave vector, d as the film thickness, and

$$\omega_0 = \mu_0|\gamma|H_{\mathrm{ext}} \tag{2.77}$$

$$\omega_{\mathrm{M}} = \mu_0|\gamma|H_{\mathrm{dip}} \tag{2.78}$$

The frequency is dependent upon the magnitude of the wavevector k but not the direction of k such that the wave propagation is isotropic in the plane of the film if there is no anisotropic field present in the plane of the film. An example of this dispersion relation is show in Fig. 2.7. The other modes are typically much weaker and can be ignored in this dissertation, though shown in Fig. 2.7. This, however, is not always the case as there can be thickness mode coupling.

3. Although the group and phase velocities, defined (to first order) as

$$v_{\mathrm{g}} = \frac{\partial\omega}{\partial k} \tag{2.79}$$

$$v_{\mathrm{p}} = \frac{\omega}{k} \tag{2.80}$$

have different magnitudes, they have the same direction. Waves with this characteristic are often referred to as forward waves.

4. The amplitude of the wave is distributed sinusoidally throughout the volume of the film.

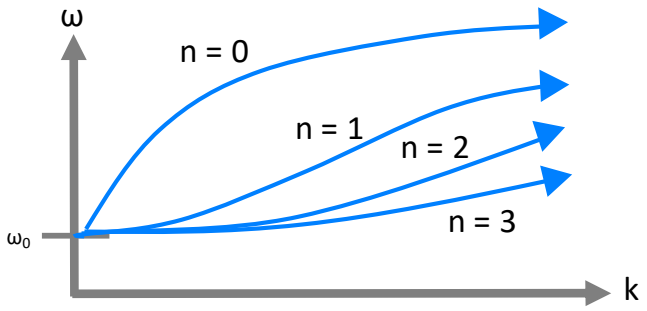

Fig. 2.7. Dispersion relation for the first 4 thickness modes in the forward volume wave configuration.

2.6.4 Backward volume waves

This second type of wave has an external DC magnetic field in the plane of the film with a wavevector k in the plane of the sample along the same direction of the DC field. A few key points about these types of waves:

1. As in the case of forward volume waves, all thickness modes share the same cutoff frequency.
2. The dispersion relation to first order in k for the lowest order thickness mode is

$$\omega^2 = \omega_0 \left(\omega_0 + \omega_M \left(\frac{1 - e^{-k_\parallel d}}{k_\parallel d} \right) \right) \tag{2.81}$$

   and k is parallel to the DC field. Also, reversing the direction of magnetic field does not change the properties of the field mode across the film thickness. This is not the case for surface waves. An example of this dispersion relation is shown in Fig. 2.8.
3. These waves have a negative group velocity but a positive phase velocity. Waves with this property are often called backward waves.
4. Lastly, the wave amplitude is distributed sinusoidally throughout the volume of the film.

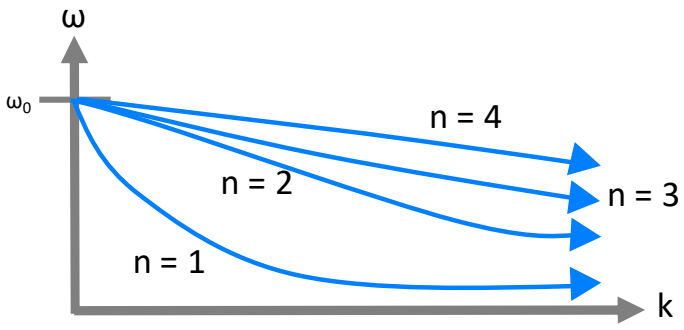

Fig. 2.8. Dispersion related for the first 4 thickness modes in the backward volume wave configuration.

2.6.5 Surface waves

This last type of wave has an external DC magnetic field in the plane of the film with a wavevector k in the plane of the sample but perpendicular to the DC field. A few key points about these types of waves:

1. Unlike the previous two cases, there are no thickness modes present in this configuration.
2. The dispersion relation to first order in k is

$$\omega^2 = \omega_0(\omega_0 + \omega_M) + \frac{\omega_M^2}{4}(1 - 2e^{-k_\perp d}) \tag{2.82}$$

   and k is perpendicular to the DC field. An example of this dispersion relation is shown in Fig. 2.9.
3. When the DC field is reversed the field shifts from one side of the film to the other, while the dispersion relation is unaffected. This is called field displacement non-reciprocity.
4. The group and phase velocity are in the same direction (with different magnitudes) and thus this is a forward wave.
5. Unlike the previous two cases, the wave amplitude decays exponentially from the surface of the film.

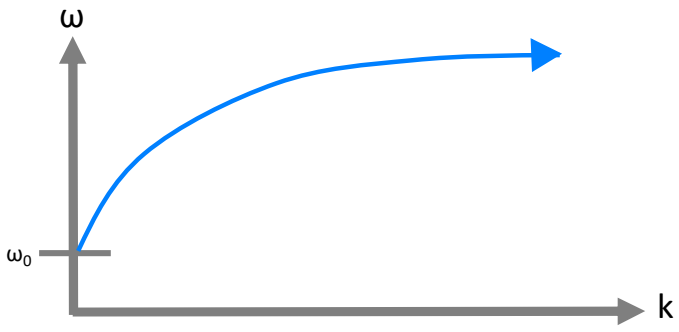

Fig. 2.9 Dispersion relation for the surface wave configuration.

2.6.6 Ferromagnetic resonance - 0th order mode

The k = 0 mode is referred to as ferromagnetic resonance (FMR) and can be used to experimentally determine the damping constant. In this mode all moments process together uniformly. The k=0 implies an infinite wavelength, but this is because some boundaries are ignored, and the film has been considered as an infinite plane. In this dissertation, FMR measurements using out-of-plane fields are carried out to determine damping and effective fields for hard drive media materials with large exchange fields or anisotropy fields. The exchange field refers to an induced field that a magnetic material will experience due to strong coupling with an outside source. Much like a permanent external field on the material. This section will focus on the Gilbert damping constant and the relaxation time damping constant of the Bloch and Bloch like equations discussed earlier.

First, by using two of Maxwell's equations, Eqs. (2.9) and (2.10), in macroscopic media, one can arrive at an equation of energy conservation for the cases of a linear dispersive media with losses. By combining

$$\boldsymbol{\nabla} \times \mathbf{H} = \mathbf{J}_{\text{free}} + \varepsilon_0 \frac{\partial \mathbf{E}}{\partial t} + \frac{\partial \mathbf{P}}{\partial t} \tag{2.83}$$

$$\boldsymbol{\nabla} \times \mathbf{E} = -\mu_0 \frac{\partial \mathbf{H}}{\partial t} - \mu_0 \frac{\partial \mathbf{M}}{\partial t} \tag{2.84}$$

$$Total\ work\ done\ by\ the\ fields = \frac{1}{2} \int (\mathbf{J}^* \cdot \mathbf{E}) d^3x \tag{2.85}$$

into a single equation by dotting H into the first equation and E into the second equation, the conservation equation within a volume (integral dropped here) is

$$\mathbf{J}^*_{\text{free}} \cdot \mathbf{E} + \boldsymbol{\nabla} \cdot (\mathbf{E} \times \mathbf{H}^*) + \mathbf{H}^* \cdot \left(\mu_0 \frac{\partial \mathbf{H}}{\partial t} + \mu_0 \frac{\partial \mathbf{M}}{\partial t} \right) + \mathbf{E} \cdot \left(\varepsilon_0 \frac{\partial \mathbf{E}^*}{\partial t} + \frac{\partial \mathbf{P}^*}{\partial t} \right) = 0 \tag{2.86}$$

This equation states that (from left to right) the total work done by the fields on the free currents,

plus the energy flow out of the boundary surface, the time rate of change of the energy in the magnetic field and magnetization, and the time rate of change of the energy in the electric field and polarization is equal to zero. In the magnetostatics limit (which applies to the FMR mode) only the 3rd and 4th terms are applicable. The real and imaginary parts of this equation correspond to the conservation of energy and stored energy, respectively. Thus, the power dissipation due to magnetic precession is

$$P = \mathbf{H}^* \cdot \left(\mu_0 \frac{\partial \mathbf{M}}{\partial t}\right) \tag{2.87}$$

This can be shown to be equal to

$$P = -\frac{1}{2}\omega\mu_0|h|^2 Im(\chi_{ii}) \tag{2.88}$$

where the AC field is in the ith direction. The simplest approach is determining the susceptibility for a given damping term. The power absorption can be directly measured using any of the FMR techniques described in chapter 3 and fitted using the above equation to extract the damping constant. In the case of multiple scattering mechanisms as shown later, it is easier to find a general curve to fit to extract the linewidth vs. frequency to determine all contributions. One could in principle treat the power absorption as a superposition of two or more different powers, but it's often easiest to find a general fitting function and fit the linewidth vs. frequency, field angle, or some other parameter to determine contributions from each source such as inhomogeneous broadening or two-magnon scattering. In this way one determines a linewidth function for a given model and does not have to worry much about the actual absorption fitting if the fitting is good. The damping constant for the Gilbert damping model (that describe magnon-electron scattering very well) can be written to 1st order in terms of the power absorption linewidth at half maximum (ΔH) and angular frequency (ω) as

$$\alpha = \frac{\mu_0|\gamma|(\Delta H)}{2\omega} \tag{2.89}$$

The damping constant for the Bloch model to 1st order specifically (it's easy to infer the other similar ones) in terms of the linewidth is

$$\frac{1}{T_2} = \mu_0|\gamma|(\Delta H) \tag{2.90}$$

These equations are independent of the type of spin waves. The dispersion relations for the case of zero wave vector for forward volume waves is given as

$$\omega = \omega_0 + \omega_{\mathrm{M}} \tag{2.91}$$

and is referred to as out-of-plane. The dispersion relation (referred to as in-plane) for the two other cases of zero wave vector is given as

$$\omega^2 = \omega_0(\omega_0 + \omega_{\mathrm{M}}) \tag{2.92}$$

2.6.7 Attenuation of spin wave modes

It's important to discuss power for the higher order modes as well. In principle, the damping constant should be the same for the higher order spin-wave modes as well. This isn't entirely correct as experimentally this doesn't hold true for the very high k modes, but it is a good approximation so going forward this assumption will be implied in the analysis. It's important to know, for a given magnetic field, how much power is absorbed (attenuated), reflected, or transmitted for a type of wave and wave number. The 0th order FMR mode can be ignored here. While still technically a spin wave, no "wave" is formed or propagates since all moments process together. The efficiency of an antenna to excite a specific wavelength will also play a key role in the power observed as well.

Losses due to the medium absorbing power don't show up in the analysis of the magnetostatics approximation or the linear approximation of the LLG equation. It's well

understood that, for electromagnetic waves, the real part of the complex frequency corresponds to the dispersion while the imaginary part corresponds to the absorption such that

$$\omega \rightarrow \mathrm{Re}(\omega) + i\mathrm{Im}(\omega) \tag{2.93}$$

This leads to a new time dependence of

$$e^{-i\omega t} \rightarrow e^{-i\mathrm{Re}(\omega)t} e^{\mathrm{Im}(\omega)t} \tag{2.94}$$

Thus, the Im(ω) describes the decay of the wave modes. The question becomes how to determine an equation to describe the imaginary part of ω. If ω is expanded in a Taylor series about the change in the FMR mode due to the losses

$$\omega(\omega_0 + \Delta\omega_0) = \omega(\omega_0) + \frac{\partial\omega}{\partial\omega_0}\Big)_{\omega_0} \Delta\omega_0 + \cdots \tag{2.95}$$

then a useful equation can be obtained. The first term represents the dispersion term that has already been derived while the following terms represent the losses. If kept to first order, the Im(ω) term can be written as

$$\mathrm{Im}\left(\frac{\partial\omega}{\partial\omega_0}\Big)_{\omega_0} \Delta\omega_0\right) \tag{2.96}$$

For most spin wave systems (and in this dissertation) the losses are described well by the LLG equation, and the imaginary part of ω needs to be related to the Gilbert damping constant to proceed. It's well known that, for the FMR mode from the LLG equation, ω is changed by

$$\omega_0 \rightarrow \omega_0 - i\alpha\omega \tag{2.97}$$

Thus

$$\mathrm{Im}\left(\frac{\partial\omega}{\partial\omega_0}\Big)_{\omega_0} \Delta\omega_0\right) = \alpha\omega \frac{\partial\omega}{\partial\omega_0}\Big)_{\omega_0} \equiv -\frac{1}{T_\mathrm{k}} \tag{2.98}$$

and the losses can be written as

$$L = \frac{-20\log * e^{\frac{-t}{T_k}}}{10^6} (\mathrm{dB/\mu s}) \tag{2.99}$$

Using the analysis above the Eq. (2.98) for both types of volume waves is given by

$$\frac{1}{T_k} = \alpha \frac{\omega_0^2 - \omega^2}{2\omega_0} \tag{2.100}$$

This describes how the losses change as a function of k and applied field. The lower limit ($k = 0$) is

$$\frac{1}{T_{kl}} = \alpha\omega \tag{2.101}$$

and the higher limit ($k \to \infty$) is

$$\frac{1}{T_{kh}} = \alpha\omega \left[1 + \frac{\omega_M^2}{4\omega^2}\right]^{\frac{1}{2}} \tag{2.102}$$

For surface waves

$$\frac{1}{T_k} = \alpha \left(\omega_0 + \frac{\omega_M}{2}\right) \tag{2.103}$$

With lower and high limits of

$$\frac{1}{T_{kl}} = \alpha\omega \left[1 + \frac{\omega_M^2}{4\omega^2}\right]^{\frac{1}{2}} \tag{2.104}$$

and

$$\frac{1}{T_{kh}} = \alpha\omega \tag{2.105}$$

respectively. Interestingly, for surface waves, the losses are the same across the entire pass band for a fixed applied field. That is, the losses are not frequency dependent for a fixed external field.

For both the volume waves and the surface waves, these equations show the maximum length of a pass band for a given field as well as how the losses change within the passband. It

should also be noted that there is some discrepancy between the theory and experimental evidence for backward volume waves. If a detailed analysis of the loss was needed, it would be necessary to keep more terms in the Taylor expansion for backward volume waves.

Lastly, it's important to discuss excitation efficiency of the spin waves. Antennas are normally designed for a specific wavenumber range, so as the wavenumber moves away from this value, there is less power delivered to the system. This will add an apparent loss to the system because this effect is frequency dependent. It's important for the reader to keep this in mind when viewing the power transmission curves in chapters 7 and 8.

2.7 Nonlinear wave dynamics

There is a plethora of nonlinear phenomenon that can be explored in spin-wave systems. Over the years, many interesting studies have done involving bright and dark solitons, nonlinear frequency shifts, nonlinear damping enhancements, and many more. While in principle it's possible to arrive at some interesting equations using the LLG equation or Maxwell's equations without linear approximations, this is analytically very extensive. In fact, for some of the simpler nonlinear behavior, such as the nonlinear frequency shift of the FMR mode, the LLG equation is satisfactory. To simplify the analysis a bit, the nonlinear Schrödinger equation for spin waves is often used. It's relatively straightforward to arrive at this equation for spin waves if the dispersion relation is expanded in a Taylor series in a general way:

$$\delta\omega = \frac{\partial\omega}{\partial k}\delta k + \frac{1}{2}\frac{\partial^2\omega}{\partial k^2}(\delta k)^2 + \frac{\partial\omega}{\partial|\psi|^2}|\psi|^2 + \cdots \tag{2.106}$$

There are many terms that could appear in this equation. So, it's necessary to know something about this system to determine how many terms are kept. Because it's a general Taylor series, ω can be expanded about other variables besides k and the correlation factor ψ as well, so terms including damping or other physical properties can be included when necessary. The

correlation factor describes the demagnetization at large precession angles and describes the nonlinearity of the system. The partial derivatives are evaluated at a value and are therefore constants.

$$\delta\omega = v_{\mathrm{g}}\delta k + \frac{D}{2}(\delta k)^2 + N|\psi|^2 \tag{2.107}$$

where D is the dispersion coefficient and N is the nonlinearity coefficient. $\delta\omega$ and δk correspond to the operators

$$\delta\omega = i\frac{\partial}{\partial t} \tag{2.108}$$

$$\delta k = i\frac{\partial}{\partial x} \tag{2.109}$$

Sometimes it's useful to change reference frame to the envelope of the traveling wave.

$$i\frac{\partial u}{\partial t} = -\frac{D}{2}\frac{\partial^2 u}{\partial x'^2} + N|u|^2 u \tag{2.110}$$

where u is the amplitude of the envelope and the prime indicates the frame of the traveling wave. This equation, the nonlinear Schrödinger equation (NLS) has been used for many years to describe interesting phenomena that have been observed for envelope spin waves.

Chapter 3. Measurement techniques

3.1 Vector network analyzer – ferromagnetic resonance

This technique relies on using a vector network analyzer (VNA) to measure the transmitted power through a coplanar waveguide (CPW) that consists of two ground planes and one signal line, typically made of gold or copper. When a sample undergoes resonance, the impedance changes and there is a corresponding change in transmission. This change in transmission can be related to the susceptibility of the sample. A general example of a VNA-FMR system is shown in Fig. 3.1.

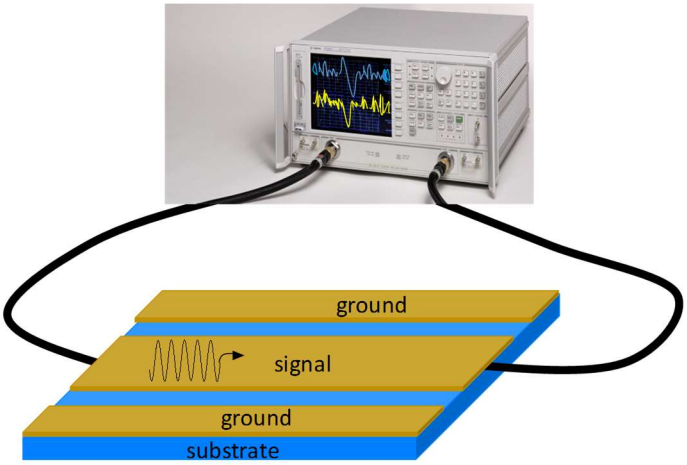

Fig. 3.1. Diagram of a VNA-FMR system using a CPW structure.

For a CPW structure, the lumped circuit is shown in Fig. 3.2 where R is the resistance, L is the inductance, C is the capacitance, and G is the shunt conductance. The reflection and transmission coefficients measured by a VNA, S_{11} and S_{21} respectively, can be directly measured by a VNA. In term of the lumped circuit elements they can be written as[29]

$$S_{11} = \frac{i\omega L + R \quad \dfrac{Z_0}{1 + Z_0(G + i\omega C)} - Z_0}{i\omega L + R + \dfrac{Z_0}{1 + Z_0(G + i\omega C)} + Z_0} \tag{3.1}$$

$$S_{21} = \frac{\frac{2Z_0}{1 + Z_0(G + i\omega\ )}}{i\omega L + R + \frac{Z_0}{1 + Z_0(G + i\omega\ )} + Z_0} \tag{3.2}$$

where Z_0 is the characteristic impedance of the CPW. S_{11} and S_{21} can in general be written as

$$S_{11} = {S_{11}}^0 + \Delta S_{11} \tag{3.3}$$

$$S_{21} = {S_{21}}^0 + \Delta S_{21} \tag{3.4}$$

where the 0 above indicates the transmission independent of the susceptibility. It's also important to note that the inductance can be written as

$$L \approx L_0 + \chi_0 \chi \tag{3.5}$$

and in the quasistatic limit

$$\Delta S_{11} = -\Delta S_{21} \tag{3.6}$$

as well as in the limit of weak reflections

$$|S_{11}| \ll 1 \tag{3.7}$$

χ_0 will be related to physical and experimental properties, and can be treated as a fitting parameter. Combing the many equations above one obtains

$$\Delta S_{21} \cong \frac{\chi}{-2\chi_0} \tag{3.8}$$

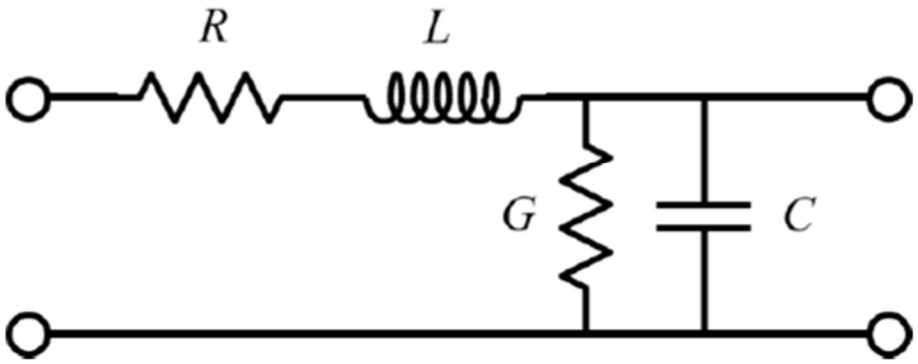

Fig. 3.2. Diagram of a lumped RLC circuit describing the CPW structure.

So that finally

$$S_{21} = {S_{21}}^{0} + DH + \frac{\chi}{-2\chi_0} \tag{3.9}$$

The middle term was added to include the fact that the background (independent of the susceptibility) will change with time (thus field) due to drifts in the electronics. The transmission parameter will be complex so it's necessary to measure the real and imaginary parts and fit the two sets of data together to obtain the static properties as well as the damping. Though the power absorption isn't explicitly written here, it is related to S_{21}.

3.2 Microwave resonant cavity-based ferromagnetic resonance

Cavity resonators have been used for a very long time and they come in many shapes and sizes. A resonant cavity is designed so that incoming microwaves are trapped to form standing waves within conducting walls but allow a small signal to be reflected out for detection. A sample is then placed in a position where the microwave magnetic field is a maximum and, in the direction, wanted for the measurement. Many textbooks like Jackson *et al*. derive solutions to Maxwell's equations for various geometries (with and without dielectric materials on the inside). This amounts to solving for plane wave solutions with conducting walls as boundaries. However, the coupling that allows the microwaves in and out as well as the perturbation of the fields due to a sample are typically not addressed in detail. If the coupling hole is designed well and the sample small enough, the perturbations are not noticeable.

Cavity quality is quantified through a parameter called the Quality factor (Q). It represents a ratio of the power stored to the energy lost either to the conducting walls or a dielectric medium inside. The Q is directly related to the surface area of the cavity so the larger the cavity, the higher the theoretical Q. It's also worth noting that in general, cylindrical cavities have an order of magnitude higher Q than a rectangular cavity at the same frequency. The FMR measurements in

this dissertation utilize a TE102 mode 13.7 GHz rectangular cavity. Though a cylindrical design would have been better, due to the experimental constraints of the high-temperature FMR system (discussed below), this wasn't possible.

When microwaves are sent into the cavity and the sample undergoes FMR, there is less power reflected back out of the cavity than when the sample isn't undergoing resonance. Since the cavity is non-magnetic (mostly anyway), there is only a change in the strength of the reflected wave when the sample undergoes resonance. Thus, the change in reflected power is equal to the power absorbed by the sample given in Eq. (2.88).

3.2.1 Modulating the static field

For samples with very small thicknesses, like in the case of nm-thick thin films, the change in reflected power is almost unnoticeable when compared with the noise level of the reflected power. So a small AC signal is often used to modulate the DC field in order filter out the

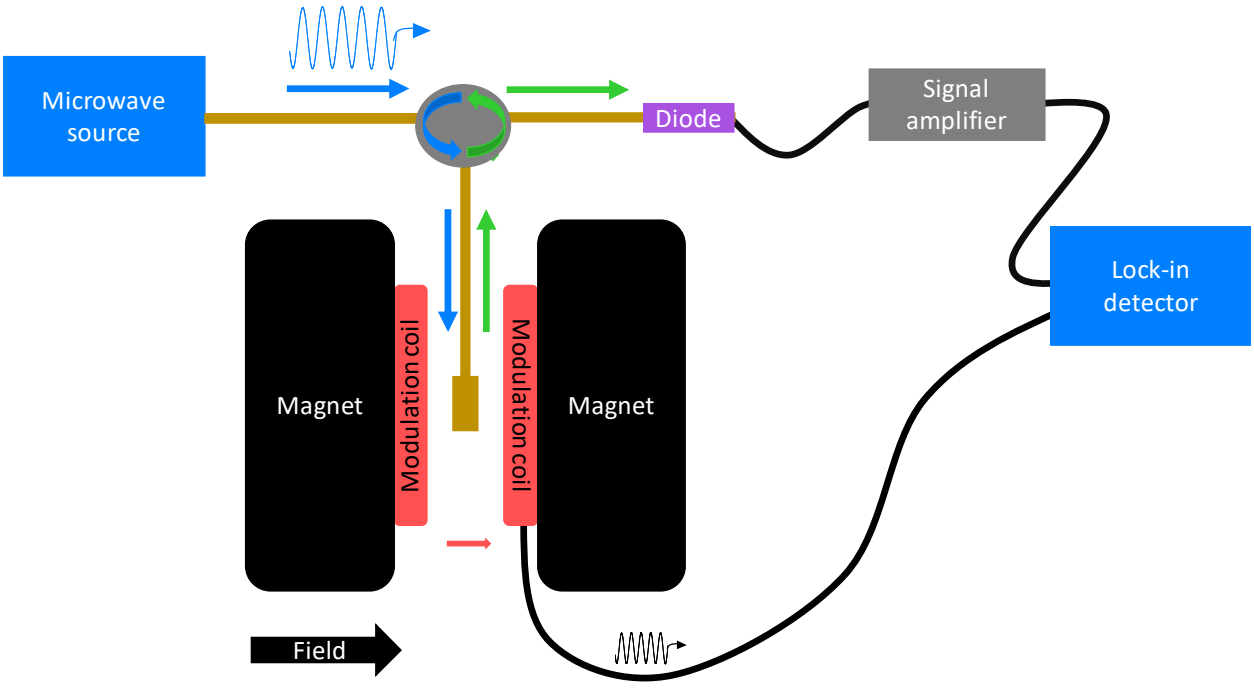

Fig. 3.3. Diagram of a cavity-based reflection FMR system using a modulation field technique.

background. By using a lock-in amplifier that modulates the signal, the background can be filtered out and the only signal measured is the change in reflection[30]. Determining the ideal AC frequency and amplitude can be a little tricky. The stronger the field is the stronger the measured amplitude. However, as the amplitude approaches the width of the power absorption peak, the absorption peak begins to broaden and become distorted. So the amplitude should be as large as possible without noticeably interfering with the signal. Similarly, the larger the frequency, the larger the amplitude strength, but it must be very small compared to the AC field driving the precession and the resonant frequency. So, the frequency should be as large as possible without noticeably interfering with the dynamics. A general example of a resonant cavity FMR system using a modulation field is shown in Fig. 3.3.

3.2.2 High temperature configuration

To measure FMR at high temperatures for many different materials, a hole was drilled in the side of the TE102 cavity mentioned above. The sample is attached to the end of a diamond rod that passes through the hole in the cavity. Diamond was chosen because of its excellent thermal conductivity but low dielectric strength (to reduce interference with the microwaves). The diamond rod is attached to a ceramic resistive heater using an aluminum nitride compound that is electrically insulating but highly thermally conductive. The cavity is placed in a vacuum chamber to reduce thermal fluctuations and allow a higher temperature to be reached. With a vacuum pressure of about 10^{-5} Torr, a temperature as high as 550 °C can be reached. The adaption was designed specifically for perpendicularly magnetized films.

3.3 Strip line excitation of spin waves

Strip line antennas (or transducer) are the most widely used structures for exciting spin waves. It typically consists of a thin metallic line deposited on a substrate that is backed by a

metallic ground plane. The line is usually grounded at one end. An AC electric current travels down the metallic line, creating AC magnetic and electric fields. The dimensions are designed to excite electromagnetic waves typically in the range of 1-10 GHz with the higher efficiencies at the lower frequencies. This gives an apparent loss to the spin-wave transmission as each frequency is not excited the same. A general example of a strip line antenna structure is shown in Fig. 3.4. The spin waves are detected by placing a second strip line at some distance away from the excitation strip line. The magnetic precession generates an AC magnetic field that will induce an AC current in the detection strip line. Sometimes at the smaller wavelength side of the spin wave transmission curve (higher wavevector numbers) the electromagnetic waves will interfere with the spin waves. This is because some of the power radiated by the excitation strip line will radiate enough power through the air to the detection strip line to cause wave interference when the wavevectors in air and in the medium, are similar. Because the excitation fields are circular, often there will be other types of spin waves (other than the intended ones) weakly excited. It's also possible to have reflections from the sides or ends of the film that will create standing waves. Such standing waves

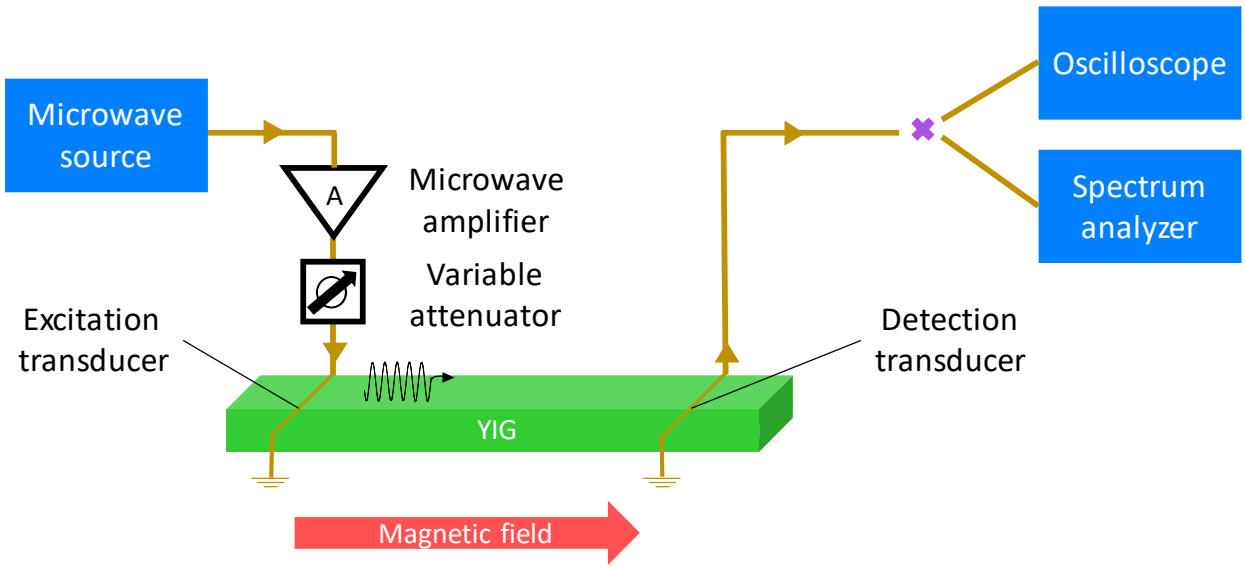

Fig. 3.4. Diagram of a strip line spin wave system.

will cause perturbations to the equations given in chapter 2 but they are normally small enough to ignore if the sample dimensions are appropriate. It is also possible, and sometimes convenient, to use a VNA for the source and detection of spin waves. As a reminder to the reader, the following chapters involving the actual experimental work will be done in the CGS unit system.

Chapter 4. Intergranular exchange coupling in CoPtCr-based perpendicular recording media

4.1 Introduction to perpendicular recording

Perpendicular magnetic recording (PMR) using CoCrPt-oxide granular media has recently achieved areal storage densities close to 1 Tb/in^2.[31,32] While PMR media technology has matured, there is still a great need to better understand the physics behind the granular media, which is very important not only for the current PMR technology to realize densities beyond 1 Tb/in^2 but also for the next-generation HAMR media. One of the physics questions of great significance, for example, is how the oxide segregant in the media affects the grain size and the grain properties and thereby the thermal stability,[33,34,35] and how it affects the strength of the effective field experienced by individual grains and thereby influences the signal-to-noise ratio (SNR) during reading.[36,37,38]

In addition to the external writing field, an individual grain in the PMR media experiences a uniaxial magneto-crystalline anisotropy field, a self-demagnetization field, an effective dipolar interaction field due to other grains, and an intergranular exchange field. The anisotropy and demagnetization fields can be determined relatively easily through conventional measurement techniques such as vibrating sample magnetometer (VSM) and FMR techniques, but the accurate determination of the effective dipolar and exchange interaction fields is rather challenging. Some indirect methods, such as the so-called ΔH_c method (difference in the coercivities of full hysteresis loops and minor recoil loops),[39,40,41] the first-order reversal curve (FORC) approach,[42] the differential remnant curve approach,[43,44,45,46] and the demagnetizing factor compensation method[47,48,49] have been used to examine the dipolar and exchange interactions in PMR media,

mostly through switching field distribution measurements. However, those methods are limited because they either rely on a certain set of assumptions or do not incorporate all the material details, and each method alone does not yield accurate results.[50]

4.2 Static properties of media doped with SiO_2 segregant

This chapter reports on the study of intergranular exchange coupling in PMR media through the determination of effective exchange fields for different remnant magnetic states via FMR measurements. The effective exchange field H_{ex} increases linearly with a decrease in the remnant magnetization M_r. The extrapolation of the H_{ex} vs. M_r plot to the H_{ex} axis yields the intrinsic intergranular exchange field. This FMR approach was first used by Hinata *et al*. to compare the exchange fields in two media samples prepared using different argon pressures.[51] In this work it is used to investigate systematically the effects of oxide segregant on the intergranular exchange interactions in PMR media. The data show that the intrinsic exchange field in CoPtCr granular films is about the same as the saturation induction and about half of the perpendicular anisotropy field. With the introduction of SiO_2 segregant to the films, the exchange field decreases. It decreases to zero when the volume fraction of the SiO_2 segregant is increased to 30%. These results, together with others presented shortly, contribute to the understanding of intergranular exchange coupling in PMR media.

The study made use of four CoPtCr-based granular film samples with different amounts of SiO_2 segregant, which were provided by Western Digital. The samples are 4-mm-diameter circular elements cut from 2-inch-diameter media disks that were grown by magnetron sputtering. The static magnetic properties of the samples were determined through VSM, magneto-optical Kerr effect (MOKE), and standard FMR measurements and are presented in Fig. 4.1.

Figures. 4.1(a) and 4.1(b) show the effective saturation induction $4\pi M_s$ and the effective perpendicular anisotropy field H_k, respectively, as a function of the volume fraction x of the SiO_2 segregant. One can see from the data that the introduction of 10% SiO_2 into the CoPtCr film leads to a slight increase in $4\pi M_s$ and a notable increase in H_k. This results mainly from the improvement of the composition gradient from the grain centers to the grain boundaries in the PMR media.[52] In more details, the introduction of the oxide segregant into the grain boundaries leads to the migration of the non-magnetic elements (Pt and Cr) from the grain cores to the grain boundaries, resulting in a higher magnetization and stronger anisotropy in the grain cores. The increase in the core magnetization gives rise to a slight increase in the $4\pi M_s$ value of the sample, even though the overall volume fraction of the magnetic phase is reduced. The enhancement in the core anisotropy is responsible for the increase in H_k. An increase in x from 10% to 20% gives rise to relatively

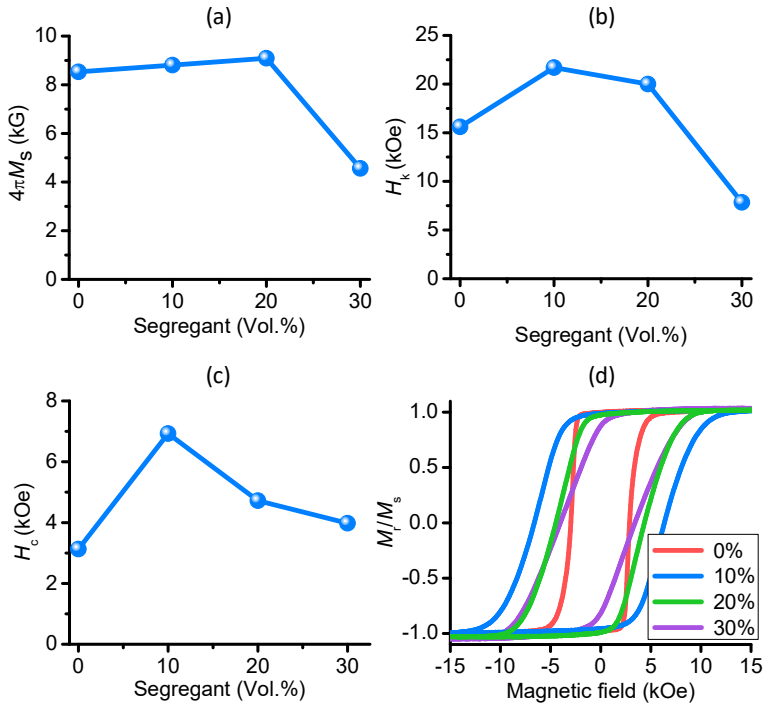

Fig. 4.1. Static magnetic properties of the samples. (a), (b), and (c) present the saturation induction $4\pi M_s$, effective perpendicular anisotropy field H_k, and coercivity H_c as a function of the volume fraction of the SiO_2 segregant. (d) presents the magnetic hysteresis loops of the four samples, where the vertical axis shows the remnant magnetization M_r to saturation magnetization M_s ratio.

insignificant changes: $4\pi M_s$ increases slightly while H_k decreases slightly. This indicates that the effects of adding 20% SiO_2 are similar to those of adding 10% SiO_2. A further increase to 30%, however, results in rather significant drops in both $4\pi M_s$ and H_k. There are two main reasons for this observation. First, high-x segregant gives rise to a reduction in the grain size, simply due to the segregant-produced constraint of space. Smaller grains are less thermally stable, resulting in a decrease in the $4\pi M_s$ and H_k values of the sample. Second, the presence of high-x SiO_2 segregant also leads to the partial oxidation of the grains,[52,53] degrading their magnetic properties.

Two important points should be made about the above discussions. First, qualitatively it is well understood that the above-described change of the magnetic properties with an increase in x should be accompanied by a drop in H_{ex}. However, quantitative studies about this have not been carried out yet. Such studies are presented below. Second, when the volume fraction of the oxide segregant is very large, the segregant enters deeply into the grain cores and thereby splits the grains into closely-spaced, exchange-coupled, smaller sub-grains or even clusters.[54] This will result in a lower effective magnetization and a lower effective anisotropy field, just as in the above-discussed sample with x=30%, as well as enhanced exchange coupling. As presented shortly, the x=30% sample shows very weak exchange coupling, indicating no segregant-caused grain splitting in the sample.

Figure 4.1(c) presents the coercive field H_c as a function of x. The data show a trend which is similar to the change of H_k with x shown in Fig. 4.1(b). This similarity is expected because the magnetization switching in the PMR media largely depends on the strength of the perpendicular anisotropy. Fig. 4.1(d) presents the full hysteresis loops of the four samples measured by the MOKE technique, from which the H_c data in Fig. 4.1(c) were determined. One can see that the sample with x=0 shows a nice square loop. The samples with $x\neq0$ show similar loops, but with a

squareness much lower than that of the x=0 sample.

4.3 Experimental procedure for measuring the exchange field

The intergranular exchange field H_{ex} in the samples was measured using the experimental configuration sketched in Fig. 4.2(a) and the measurement steps illustrated in Fig. 4.2(b). The experiment setup consists mainly of the CPW device and a VNA (discussed in chapter 3), and the sample is placed on the CPW with the media side facing the CPW structure and the substrate side facing up. The measurements involve the following three major steps. First, the sample is magnetized to saturation in an out-of-plane configuration using a large positive magnetic field. The corresponding magnetization state in the hysteresis loop is indicated by point A in Fig. 4.2(b). Next, a moderate negative field is applied to switch some of the grains from the "up" state to the "down" state. This step brings the magnetization state in the loop from point A to point B. Last, a smaller negative field, which points downward as shown in Fig. 4.2(a), is applied to change the magnetization state from point B to point C, and the FMR measurement is then performed by sweeping the external field about this field and measuring the complex transmission parameter S_{21} of the CPW/sample structure with the VNA. During the FMR measurements, both the microwave frequency and power are kept constant.

By selecting the appropriate microwave frequency, one can realize FMR for un-switched "up" grains, not switched "down" grains, in the media sample. For the FMR in those "up" grains, one can write the Eq. (2.91) (in CGS units) as

$$f = |\gamma|(H_{\mathrm{FMR}} + H_{\mathrm{eff}}) \tag{4.1}$$

where H_{FMR} is the external static magnetic field at which the resonance occurs and H_{eff} is the effective internal field on the "up" grains and can be written as[51]

$$H_{\mathrm{eff}} = H_{\mathrm{k}} - N_{\mathrm{g}} 4\pi M_{\mathrm{s}} - \left(N_0 M_{\mathrm{r}} - N_{\mathrm{g}} 4\pi M_{\mathrm{s}}\right) - H_{\mathrm{ex}} \tag{4.2}$$

where H_k is the anisotropy field, N_g is the demagnetization factor of an individual grain, N_0 is the global demagnetization factor of the film sample, and M_r is the remnant magnetization. Note that for the data presented below most of the FMR measurements were performed in a field region indicated by point C in Fig. 4.2(b) and H_{FMR} in Eq. (4.1) took a negative value. Note also that in the right side of Eq. (4.2), the second term denotes the self-demagnetization field in a grain, while the third term describes the global demagnetization field or the effective dipolar field on the grain due to other grains. The substitution of Eq. (4.2) into Eq. (4.1) yields

$$2\pi f = |\gamma|(H_{FMR} + H_k - N_0 M_r - H_{ex}) \tag{4.3}$$

Once the FMR field and the static properties are known, H_{ex} can be calculated using Eq.

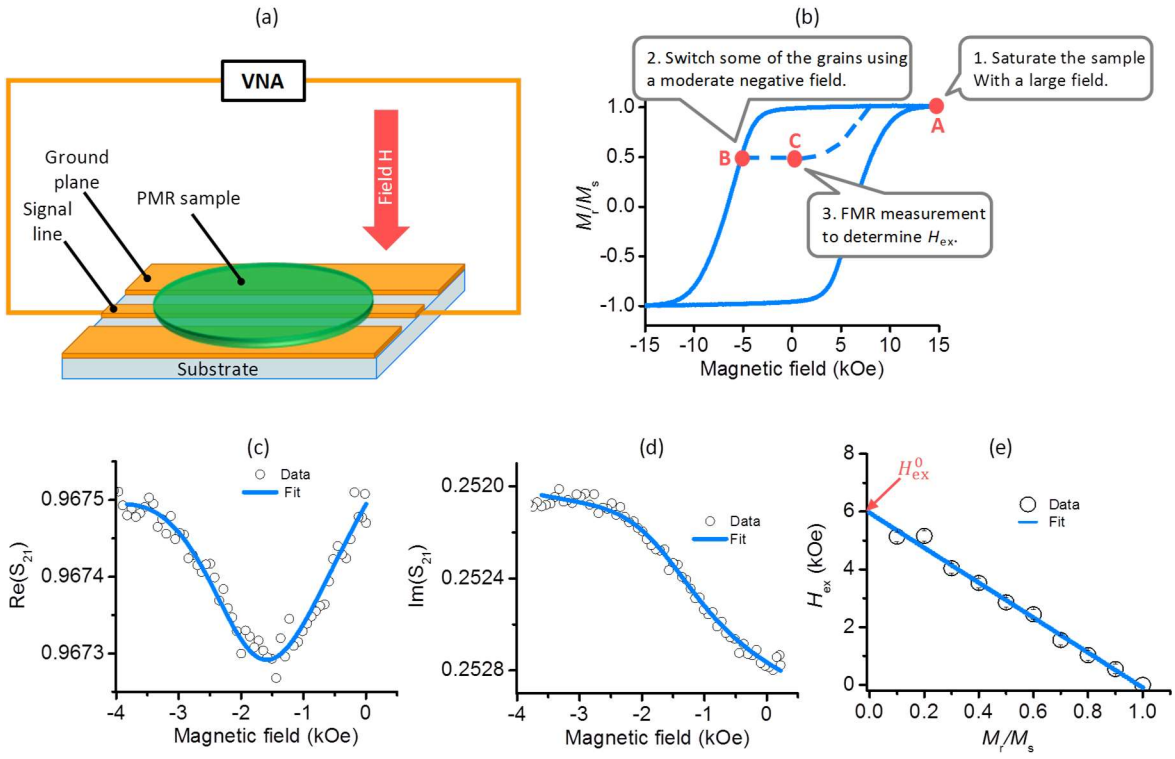

Fig. 4.2. Exchange field measurement approach. (a) Experiment configuration. (b) Major experimental steps. (c) and (d) the real and imaginary parts of the S_{21} parameter of the CPW/sample structure. The open circles show the data, while the blue curves show the numerical fits. (e) Effective exchange field H_{ex} as a function of M_r/M_s. The open circles present the data, while the line is a linear fit. The fitting yields the intrinsic exchange field H^0_{ex}, as indicated. All the data were obtained with the 10%-segregant sample.

(4.3). The strength of H_{ex} strongly depends on M_r. When M_r=0, about half of the grains are in the "up" state, while the other half is in the "down" state. In this case, H_{ex} is close to the intrinsic intergranular exchange field which the grains experience. When $0<M_r<M_s$, more grains are in the "up" state than in the "down" state. In this scenario, among the "up" grains only those that are in close proximity to the "down" grains experience strong exchange coupling, while other grains experience a much weaker exchange field. The net effect is that the H_{ex} field calculated using Eq. (4.3) is an effective field averaged over the entire sample and is therefore lower than the intrinsic exchange field. Further, the closer the M_r value is to the M_s value, the smaller the H_{ex} field is. It turns out that with an increase in M_r, the H_{ex} field decreases linearly, as presented shortly. Thus, one can measure H_{ex} at different remnant states first and then plot H_{ex} as a function of M_r and extrapolate the plot to M_r=0 to determine the intrinsic intergranular exchange field. In the discussions below, H_{ex} denotes the effective exchange field at $M_r>0$, while the intrinsic exchange field at M_r=0 is denoted by H_{ex}^0.

One can take the following procedures to determine the intrinsic exchange field H_{ex}^0.

(i) Perform FMR measurements for a certain remnant state with a known M_r value, using the steps illustrated in Fig. 4.2(b). The measurements yield the complex S_{21} data, which are shown by the open circles in Figs. 4.2(c) and 4.2(d). Note that the data were measured with the 10%-SiO_2 sample at f= 36 GHz and M_r/M_s = 0.5.

(ii) Determine H_{FMR} through fitting the real and imaginary parts of S_{21} with theoretical FMR profiles,[55, 56] as shown by the blue curves in in Figs. 4.2(c) and 4.2(d).

(iii) Calculate H_{ex} using Eq. (4.3) and the H_{FMR} value from (ii).

(iv) Repeat (i)-(iii) for different remnant states and obtain H_{ex} data for different M_r values.

(v) Plot H_{ex} as a function of M_r/M_s, as shown in Fig. 4.2(e).

(vi) Fit the H_{ex} vs. M_r/M_s data linearly and then extrapolate the line to the vertical axis to determine H_{ex}^0 as shown in Fig. 4.2(e).

4.4 Exchange field vs. segregant

Figure 4.3 presents the results obtained through the measurement and analysis procedures described above. Fig. 4.3(a) shows the H_{ex} vs. M_r/M_s data and the corresponding linear fits. One can see that all the numerical fits are reasonably good, and the H_{ex} values are all close to zero at M_r/M_s=1 as expected. The extrapolation of the lines to the H_{ex} axis yields the H_{ex}^0 values for the four samples, which are presented in Fig. 4.3(b).

One can see three important results from the data shown in Fig. 4.3(b). First, the intergranular exchange field in the CoPtCr granular films with zero oxide segregant is strong, about the same as $4\pi M_s$ and about half of H_k. Second, with the introduction of an oxide segregant to the CoPtCr films, the overall trend is that the exchange field decreases with an increase in the volume fraction x of the oxide segregant. Third, the exchange field decreases to zero when the volume fraction of the segregant is increased to 30%. This provides strong evidence for the absence of the segregant-caused splitting of the grains into smaller grains or clusters in the x=30% sample. Such

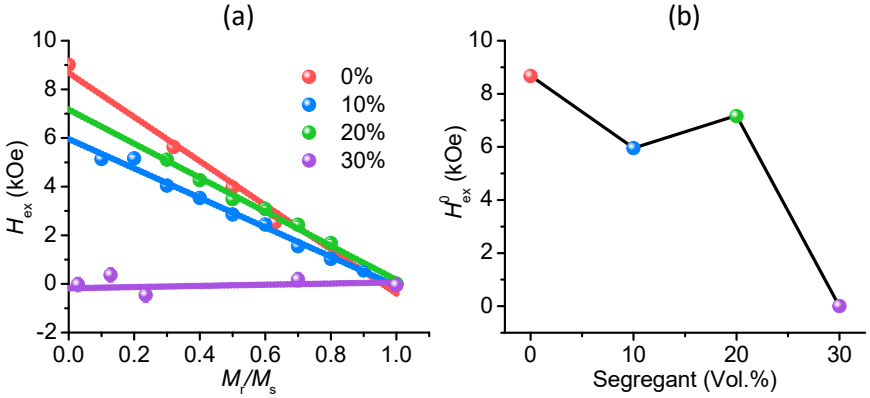

Fig. 4.3. Intergranular exchange field. (a) Effective exchange field H_{ex} as a function of M_r/M_s for four samples, as indicated. The dots present the data, while the lines are linear fits. (b) The intrinsic exchange field H^0_{ex}, obtained from the linear fitting shown in (a), as a function of the volume fraction of the SiO_2 segregant.

splitting would result in an enhancement in the exchange field, rather than a decrease. These results together indicate that one can effectively manipulate the intergranular exchange coupling in PMR media via controlling the amount of the oxide segregant. They also indicate that the experimental approach described above allows for the determination of intrinsic intergranular exchange fields in granular films. It should be pointed out that, although the overall trend is that H_{ex}^{0} decreases with an increase in x, H_{ex}^{0} increases slightly when x is increased from 10% to 20%. The reason for this change is currently unknown. A simple analysis of the changes in the static properties, such as the decrease in H_c and the increase in $4\pi M_s$, suggests that this increase is real and not due to an experimental error. However, there are other factors, such as degraded texture, grain size, and thermal stability, that would need to be considered in detail in order to explain this H_{ex}^{0} increase.

For the data presented above, the CPW structure had a 50-μm-wide signal line and a signal line-to-ground spacing of 25 μm, the out-of-plane field used to magnetize the sample to saturation had a strength of 18 kOe, and the microwave used for the S_{21} measurements had a nominal power of 0.1 mW. All the FMR measurements were performed in a region where the magnetization was either constant or changes very little during the sweeping of the magnetic field. There are error bars in Fig. 4.3(a) and 4.3(b), but they have a size either similar to or smaller than the data points and are therefore not visible. The error bars in Fig. 4.3(a) are the standard deviations for the numerical fitting of the S_{21} profiles, while those in Fig. 4.3(b) are the standard deviations for the linear fitting of the H_{ex} vs. M_r/M_s data. The calculations of H_{ex} using Eq. (4.3) took $|\gamma|$=2.8 MHz/Oe and N_0=1.

4.5 Conclusions

In summary, this work studied intergranular exchange coupling in PMR media materials through FMR measurements at different magnetic states. The data showed that the exchange field

in CoPtCr granular films is comparable to the saturation magnetization of the films in the absence of oxide segregant, can be reduced through the addition of SiO_2 segregant to the films, and can be reduced to zero if the volume fraction of the SiO_2 segregant is increased to 30%. The static and FMR measurements together indicate that, when the volume fraction of the segregant is as high as 30%, the segregant does not penetrate deeply into the grain cores and break the grains into smaller grains. These results contribute to the understanding of the effects of the oxide segregant on the media properties as well as on the recording performance, including thermal stability and the signal-to-noise ratio during reading. Two final notes should be made. First, the exchange field measurement approach used in this work was first used by Hinata et al., though in Ref. [51] they presented only a simple comparison study on two PMA samples made using different argon pressures. Second, both the results on the effects of the oxide segregant presented above and the exchange field measurement technique used in this work should apply to future FePt-based HAMR media, though the FMR measurements have to be carried out at elevated temperatures so that the FMR frequencies can be reduced to ease experiments and the effects at temperatures close to the writing temperature can be examined. In the next chapter, damping in HAMR media is studied for several samples where a carbon based segregant, instead of SiO_2, is used to change the properties of FePt-based HAMR media.

Chapter 5. Near-T_c ferromagnetic resonance and damping in FePt-based heat assisted magnetic recording media

5.1 Introduction to heat assisted magnetic recording

Heat assisted magnetic recording (HAMR), the most promising technology for next-generation hard disk drives, makes use of laser to heat the recording media to an elevated temperature, near the Curie temperature (T_c), to significantly reduce the coercivity of the media material and thereby ease the switching of the magnetization.[57,58,59,60] HAMR drives have been promised to be released to the market in the near future, but understanding of the damping at high temperatures near T_c in HAMR media has not been realized yet, though it is of great fundamental and practical interest.

Fundamentally, the physical mechanisms underlying the near-T_c damping in HAMR media are unclear, although there have been interesting experimental studies on damping properties at room temperature (RT) in perpendicular recording media materials including HAMR media.[61,62,63,64,65] Further, it is also unknown which macroscopic model is more suitable to describe the near-T_c damping in HAMR media, although several different models have been previously used to analyze damping at high temperature (T), including the Gilbert equation,[18,19] the Bloch-Bloembergen (BB) equation,[20] the Landu-Lifshitz-Block equation,[23,24] the Xu-Zhang equation,[22,25] and the Tzoufras-Grobis equation.[21] Practically, the nature and strength of the damping in the HAMR media is directly related to the switching time and the signal-to-noise ratio of the reading which significantly impact hard drive performance.

The previous experimental efforts on damping in perpendicular recording media include three studies on damping in $L1_0$-ordered FePt thin films,[63,64,65] which have been widely accepted

as the very media material in next-generation HAMR drives. Those studies used the same approach, the optical pump-probe technique, to measure the effective Gilbert damping constant (α_{eff}), but the α_{eff} values obtained are inconsistent, possibly due to the differences in the samples or the experiment details. Specifically, Mizukami *et al.* found α_{eff}=0.055 and also emphasized that the intrinsic damping should be smaller than this value, [63] while Becker *et al.* found a much larger value α_{eff}=0.1 and claimed that this value was mostly intrinsic and contained little extrinsic contribution if any.[64] Lee *et al.* obtained an even larger value which was 0.21.[65] Though these studies represent the first attempts on exploring damping in FePt-based HAMR media, the measurements were all carried out at RT, rather than at elevated temperatures at which the writing operation occurs. Possible relaxation routes in FePt media include spin-flip magnon-electron scattering (SF-MES, inter-band scattering),[7,8,9,10] magnon-electron scattering associated with Fermi surface breathing (intra-band scattering),[7,8,9,10] two-magnon scattering (TMS),[12,13,14,61,62] and magnon-phonon scattering.[6] As these relaxation processes all exhibit strong T dependence, the damping value near T_c in FePt HAMR media may differ significantly from the RT values cited above.

This chapter reports on the first experimental study of near-T_c damping in commercial-like $L1_0$-FePt-based HAMR media. Specifically, ferromagnetic resonance (FMR) experiments were performed along three distinct dimensions of important relevance to practical HAMR applications, (1) the volume fraction of carbon (x) in the media, (2) the media temperature (T), and (3) the angle of the external magnetic field (θ_H) relative to the film normal direction, at temperatures right below T_c. The FMR linewidth (ΔH) data as a function of T, x, and θ_H were determined, and the effective damping constant α_{eff} in the Gilbert model[18,19] and the transversal relaxation time T_2 in the BB model20[20] were estimated. The data indicate that at temperatures about 10-45 K below T_c, relevant

to T in HAMR writing operation, the TMS and SF-MES processes co-exist and make comparable contributions to ΔH. With a decrease in T, however, ΔH increases, mostly due to the enhancement of the TMS process. Via varying x, ΔH, α_{eff}, and T_2 can be tuned as large as a factor of four near T_c. When varying θ_H, ΔH and α_{eff} show a maximum at about 45°, which is an angle relevant to the actual HAMR writing operation. The α_{eff} values obtained are smaller than those measured at RT in previous works.[63,64,65]

5.2 Sample growth and characterization

The samples were grown on single-crystal (001) MgO substrates by DC magnetron sputtering and consist of a 10-nm-thick FePt layer with the carbon volume fraction x=0%, 10%, 20%, or 30% and a 3-nm-thick carbon capping layer. The base pressure of the sputtering chamber was 5.0×10^{-7} Pa or lower. Prior to the sputtering growth, the MgO substrate surface was thermally cleaned at 600 °C for 1 hour. After that, the MgO substrate was maintained at the same temperature, and a FePt-C granular film was deposited by co-sputtering a FePt alloy target and a carbon target under an Ar pressure of 0.48 Pa at a deposition rate about 0. 2 Å/s. The Fe:Pt atomic ratio in the FePt films is nearly 1:1. The alternating layer deposition technique was used to suppress the growth of the secondary mis-oriented FePt grains and obtain single-columnar, highly-(001)-textured FePt nano-granular films. Following the FePt growth, a 3-nm-thick carbon over-coating layer was deposited at RT, which works as the protection layer of the FePt film. The microstructure properties of the samples were measured by transmission electron microscopy (TEM) using an "FEI Tecnai T20" TEM system at an electron accelerating voltage of 200 kV. The magnetization curves and hysteresis loops were measured by a superconducting quantum interference device vibrating sample magnetometer using magnetic fields of up to ±70 kOe. More details about the sample growth and characterization are provided in Refs. [66], [67], [68], and [69]. Note that for

the data presented below, all the samples were provided by the National Institute for Materials Science in Tsukuba, Japan.

Figure. 5.1 presents the main data about the microstructure and static magnetic properties of the samples. Fig. 5.1(a) shows the TEM images of the four samples, with the carbon volume fraction x indicated at the left-top corners. Figs. 5.1(b), 5.1(c), and 5.1(d) give the average grain size (d), coercivity (H_c) measured with perpendicular fields, and the ratio of the in-plane remnant magnetization ($M_{r\text{-}IP}$) to the out-of-plane remnant magnetization ($M_{r\text{-}OP}$), respectively, as a function of x. The data were all measured at RT.

The data in Figs. 5.1(a) and 5.1(b) show that the addition of carbon to FePt can effectively break big FePt grains with d≈75 nm into much smaller grains with d≈10 nm; and the higher the carbon volume fraction is, the smaller the grains are. The data in Fig. 5.1(c) indicate that the

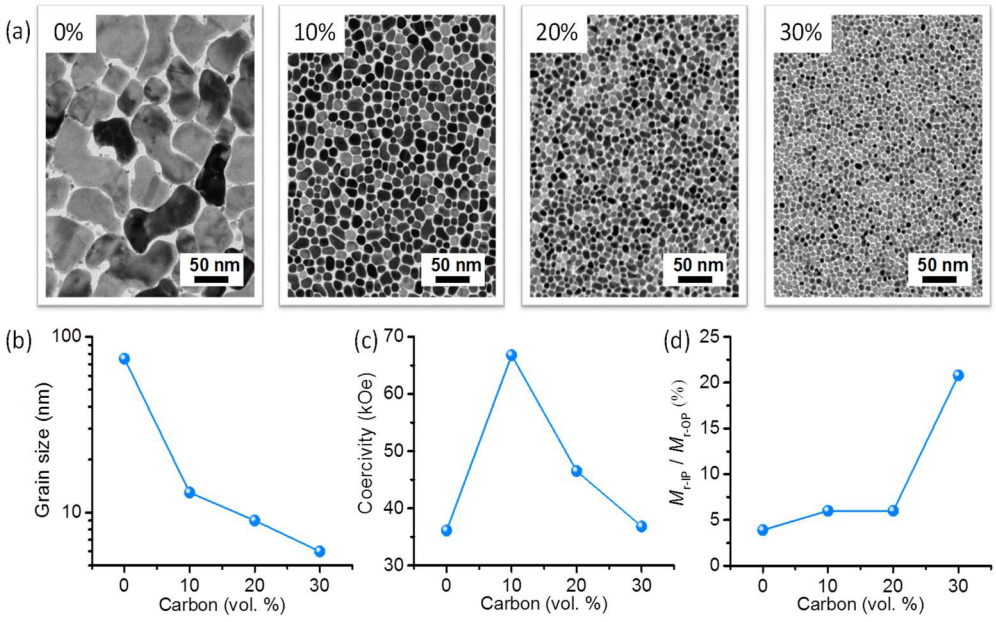

Fig. 5.1. Microstructural and static magnetic properties of four FePt media samples. (a) TEM images. (b) Average grain size as a function of the carbon volume fraction (x). (c) Coercivity as a function of x. (d) The ratio of in-plane remnant magnetization ($M_{r\text{-}IP}/M_{r\text{-}OP}$) to out-of-plane remnant magnetization as a function of x.

introduction of 10% carbon can result in a significant increase in H_c, which is mostly due to the formation of physically separated, vertically oriented, small-size columnar FePt grains and a corresponding transition from domain wall motion-type magnetization reversal to rotation reversal. However, an increase in x to 20% and then 30% results in a notable decrease in H_c, which is mainly due to the size effect of the grains, namely, that the smaller the grains are, the stronger role the thermal energy plays in magnetization reversal. In contrast, the $M_{r\text{-}IP}/M_{r\text{-}OP}$ ratio exhibits a completely different trend – it increases very little when x increases from 0% to 10% and then 20% but increases substantially when x is raised to 30%, as shown in Fig. 5.1(d). This result suggests that, an increase in x from 0% to 10% and then 20% results in big changes in both d and H_c but not in the (111) orientation of the FePt grains, while an increase to x=30% leads to the presence of some mis-oriented grains in the FePt layer. This degrading of the (111) orientation also explains in part the relatively low H_c value measured for x=30%. These results together clearly indicate that one can use the carbon volume fraction as a very effective tool to widely tune the microstructural and magnetic properties of the FePt media, as well as the FMR and damping properties as presented shortly.

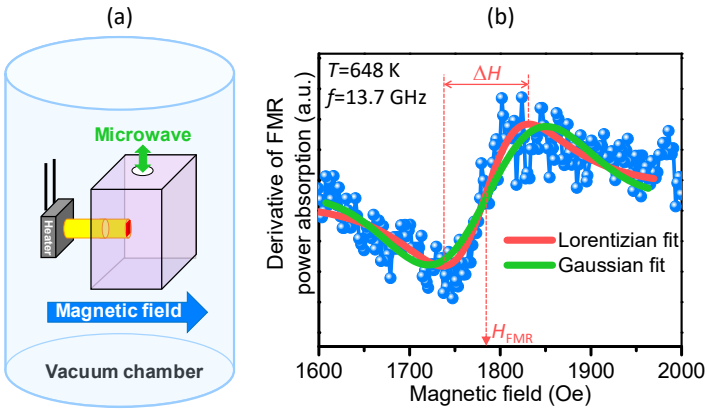

Fig. 5.2. High-Temperature Ferromagnetic resonance (FMR). (a) Schematic of experimental setup. (b) Representative FMR power absorption data (blue dots), and Lorentzian fit (red curve) and Gaussian fit (green curve) of the data. The data were measured on the FePt media sample with x=20% at 648 K. The Lorentzian fit-yielded FMR field H_{FMR} and peak-to-peak FMR linewidth ΔH are indicated in (b).

5.3 Experimental procedure

Figure 5.2 shows the high-T FMR approach which was used to study the near-T_c damping in the above-described samples. Figure 5.2(a) shows a schematic diagram of the experimental system. The main components include a rectangular microwave cavity (purple), a diamond rod (yellow) with a diameter of 2 mm that loads the sample (red) into the cavity, and a ceramic heater (gray) that heats the sample through the diamond rod. These components are housed in a high-vacuum chamber, and the measurements are performed at a pressure of about 5×10^{-5} Torr to prevent changes in sample properties due to oxygen during high-T measurements. For the FMR data presented in this paper, the microwave frequency (f) was kept constant at 13.7 GHz, which was also the resonant frequency of the microwave cavity, while the external magnetic field was swept. Field modulation and lock-in detection were used, so all the FMR profiles presented in this paper are the derivatives of the FMR power absorption. The sample temperature (T) was calibrated through separate measurements using a thermal couple. Prior to placing the sample in the FMR system, the sample was saturated by an out-of-plane field of 80 kOe at room temperature. After placing the sample in the FMR system and heating it, prior to each FMR measurement the sample was saturated by a field of 15 kOe.

Figure 5.2(b) presents the FMR data (blue dots) measured at T=648 K on the "x=20%" sample and a numerical fit (red curve) to the derivative of a Lorentzian trial function. The Lorentzian fitting-yielded peak-to-peak FMR linewidth ΔH and field H_{FMR} are indicated in the figure. A fit (green curve) to the derivative of a Gaussian trial function is also included in the figure. One can see that the Lorentzian fit is better than the Gaussian fit, indicating that the inhomogeneity line broadening contribution, if any, to ΔH is small. In the case that a film sample has strong spatial inhomogeneity and the associated line broadening is large, the Gaussian function

would fit the data better than the Lorentzian function.[70] It should be noted that the inhomogeneity line broadening contribution may be significant at room temperature due to the presence of very strong anisotropy (75-100 kOe based on hard-axis measurements). Note also that one can carry out frequency-dependent FMR measurements to determine the inhomogeneity line broadening contribution, as reported in Refs. [32] and [71].

5.4 Carbon volume fraction dependence of resonance field and linewidth

Turn now to the high-T FMR data measured using the approach described above. Figure 5.3 presents the data measured on the "x=20%" sample at six different T. Figure 5.3(a) gives the FMR data (blue dots) measured at four different T, as indicated, and the corresponding Lorentzian fits (red curves). Figures 5.3(b) and 5.3(c) plot the Lorentzian fitting-yielded H_{FMR} and ΔH, respectively, as a function of T. Figure 5.3(d) shows the saturated magnetic moment (m_s) and coercivity (H_c), as a function of T. The big blue arrows in Figs. 5.3(b) and 5.3(c) indicate the overall trends, while the blue rectangle in Fig. 5.3(d) indicates the T range of the FMR measurements. All the measurements were taken with a perpendicular magnetic field, namely, θ_H=0.

Prior to discussing the data in Fig. 5.3, it should be noted that the FMR measurements were carried out over a T range of 634-673 K, as indicated by the blue rectangle in Fig. 5.3(d). No FMR measurements were taken at T<634 K. This is because, with a decrease in T, the FMR profile shifts to negative fields, which can be inferred from the trend shown in Fig. 5.3(b); and the signal-to-noise ratio of the FMR data also become small at low T, due to linewidth enhancement which is shown in Fig. 5.3(c). At T>673 K, the FMR signal becomes non-detectable, mainly due to a significant drop in m_s which is evident from the red curve in Fig. 5.3(d). It should be highlighted that although the highest measurement temperature 673 K is still about 22 K below T_c, which is

about 695 K as shown in Fig. 5.3(d), it is already near or close enough in terms of HAMR applications, in which the writing operation occurs at temperatures 10-25 K below T_c.

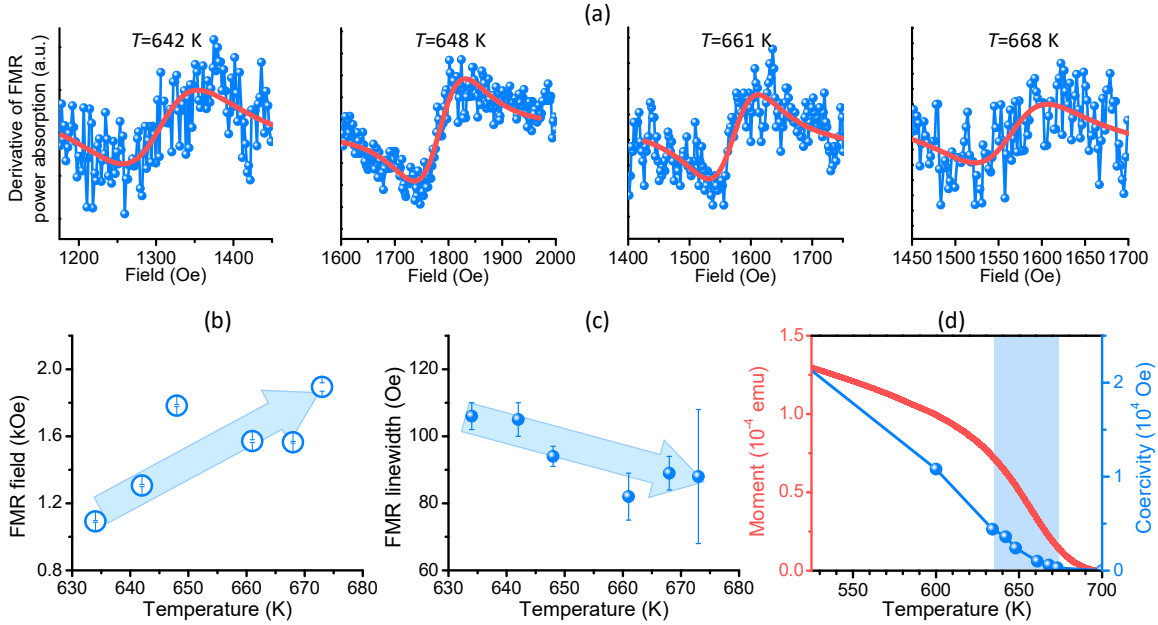

Fig. 5.3. High-T FMR data measured on the "x=20%" sample with the field angle θ_H=0. (a) Representative FMR profiles (blue dots) and corresponding Lorentzian fits (red curves). (b) FMR field H_{FMR} as a function of T. (c) FMR linewidth ΔH as a function of T. (d) Saturated magnetic moment (red, left axis) and coercivity (blue, right axis) as a function of T. The blue rectangle in (d) indicates the T range of the FMR measurements.

The data in Fig. 5.3(b) show an overall increase of H_{FMR} with T, and this result suggests that with an increase in T over 634-673 K, the effective perpendicular anisotropy field H_u drops by a larger amount than the saturation magnetization $4\pi M_s$ does. The Kittel equation for the FMR concerned here can be written (in CGS units) as

$$2\pi f = |\gamma|(H_{FMR} + H_u - 4\pi M_s) \tag{5.1}$$

One can see that for a given f, an increase in H_{FMR} would mean a decrease in H_u-$4\pi M_s$. Since the T dependences of H_u and $4\pi M_s$ differ in different samples due to differences in the microstructures, one would expect different H_{FMR} vs. T trends in the four samples. This expectation is discussed shortly.

The data in Fig. 5.3(c) suggest an overall decrease of ΔH with increasing T. This result may indicate that two-magnon scattering is a dominant relaxation mechanism in the T range considered here. Theoretically speaking, the damping mechanisms in FePt medium samples should include spin-flip magnon-electron scattering (SF-MES),[7,8,9,10] magnon-electron scattering associated with Fermi surface breathing,[7,8,9,10] two-magnon scattering (TMS),[12,13,14] and magnon-phonon scattering,[6] as listed in the introduction section. Practically, the contributions to ΔH from both the Fermi surface breathing-associated magnon-electron scattering and the magnon-phonon scattering should be notably smaller than those from the SF-MES and TMS processes. The damping due to the Fermi surface breathing-associated scattering usually decreases with an increase in T, so it is large at low T but can be ignored near T_c.[7,8,9] The magnon-phonon scattering generally plays important roles in relaxation in magnetic insulators, such as $Y_3Fe_5O_{12}$ and $BaFe_{12}O_{19}$,[72,73] but in metallic systems it usually makes much less contributions to the damping than the magnon-electron scattering processes.[6] Thus, for the FMR data in this work one can approximately write

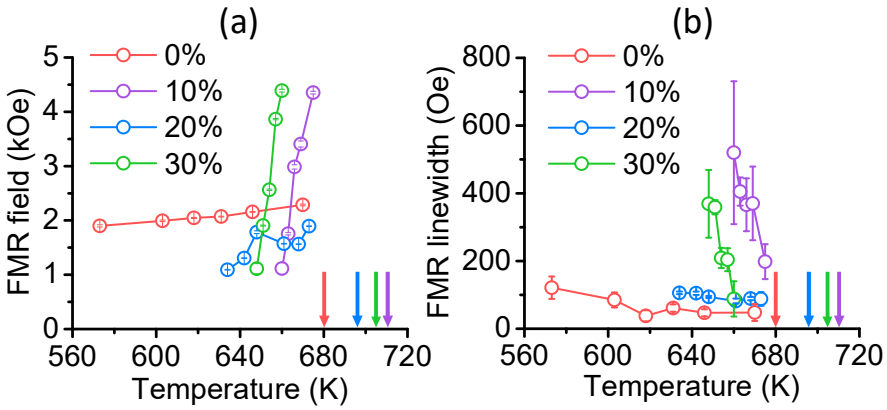

Fig. 5.4. Comparison of high-T FMR data of four samples with different carbon volume fractions, as indicated, measured at the field angle θ_H=0. (a) FMR field H_{FMR} as a function of T. (b) FMR linewidth ΔH as a function of T. The vertical arrows indicate the T_c values of the four samples, with the colors matching those of the data sets.

$$\Delta H = \Delta H_{SF-M} + \Delta H_{TMS} \quad (5.2)$$

where $\Delta H_{\text{SF-MES}}$ and ΔH_{TMS} denote the contributions of the SF-MES and TMS processes, respectively.

It is known that both $\Delta H_{\text{SF-MES}}$ and ΔH_{TMS} exhibit strong T dependences. $\Delta H_{\text{SF-MES}}$ generally increases with T. This is because the SF-MES process requires both the momentum and energy conservations which can be satisfied more easily at high T.[7,8,9] In contrast, ΔH_{TMS} usually decreases with an increase in T in magnetic thin films with perpendicular anisotropy. This is because the damping due to the TMS generally scales with the square of H_{u},[14] while the latter drops as T approaches T_{c}. For this reason, the data in Fig. 5.3(c) seem to indicate that ΔH_{TMS} may be dominant over $\Delta H_{\text{SF-MES}}$ over the T range of 634-673 K. This result is further discussed below.

To confirm the above conclusions and also evaluate the effects of the carbon volume fraction x, the same FMR measurements and analyses were performed on the other three samples. Fig. 5.4 summarizes the main results of all the four samples. Note that the measurement temperature range is different for different samples, due to the temperature limitations mentioned above. The data in Fig. 5.4(a) show that the four samples share the same trend, namely, that H_{FMR} increases with T. This result indicates that in all the samples H_{u} drops by a larger amount than $4\pi M_{\text{s}}$ when T increases, as discussed above. The data also show that the "x=10%" and "x=30%" samples exhibit much stronger T dependences than the other two samples. This suggests that with an increase in T, H_{u}-$4\pi M_{\text{s}}$ drops faster in the "x=10%" and "x=30%" samples. In other words, H_{u} decreases by a larger amount than $4\pi M_{\text{s}}$ does in the "x=10%" and "x=30%" samples, but not as large in the other two samples. This result supports the above-drawn conclusion that one can effectively manipulate the magnetic properties of the HAMR media via tuning the carbon volume fraction in the media.

The data in Fig. 5.4(b) show that ΔH decreases with an increase in T for all the four samples, indicating that the TMS process is a dominant relaxation mechanism in all the samples. The data also indicate that the "x=10%" and "x=30%" samples show much stronger T dependences than the other two samples. This result is consistent with the above-described result on the T dependences of H_{FMR}. This consistency supports the above conclusion that the TMS is a dominant damping mechanism. In general, H_{FMR} increases with a decrease in H_u as shown in Eq. (5.1) while ΔH_{TMS} scales with H_u^2 as discussed in Ref. [14]. For this reason, a fast drop in H_u would give rise to a fast increase in H_{FMR} and a fast decrease in ΔH.

5.5 Angle dependence of resonance field and linewidth

The FMR data presented in Figs. 5.2-5.4 were all measured at θ_H=0, but in actual HAMR applications the writing operation occurs at θ_H=35°-45°. For this reason, high-T FMR measurements were also performed at different field angles, with the major results presented in Fig. 5.5. Note that the largest angle used in the experiments was 65°, and the physical constraints of the FMR system did not allow for measurements at larger angles (θ_H>65°).

The data in Fig. 5.5(a) indicate that the H_{FMR} vs. T responses show different trends for different θ_H. This is because the roles of H_u and $4\pi M_s$ in the FMR strongly depend on the

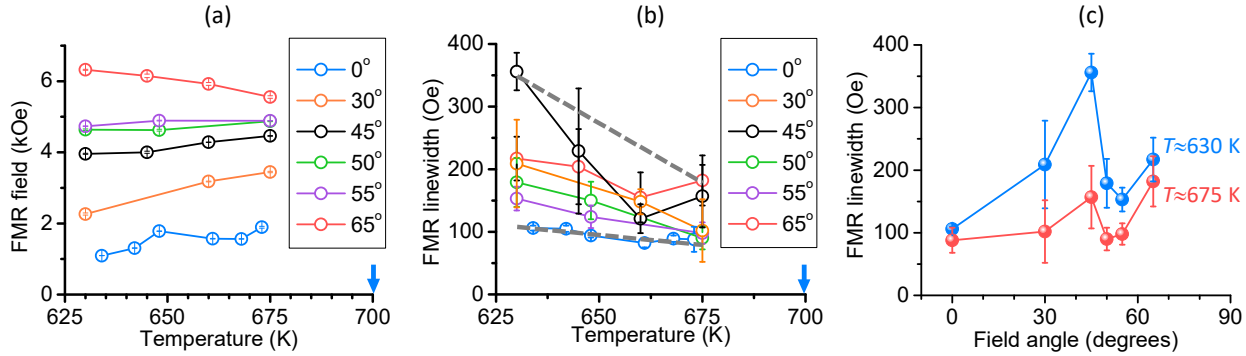

Fig. 5.5. Field angle-dependent high-T FMR data measured on the "x=20%" sample. (a) and (b) show the FMR field H_{FMR} and linewidth ΔH, respectively, as a function of T measured at six different θ_H. (c) shows ΔH as a function of θ_H for two different T, as indicated. The vertical arrows in (a) and (b) indicate the T_c of the sample.

equilibrium direction of the magnetization vector in the materials, as described by (in CGS units)

$$\left(\frac{2\pi f}{|\gamma|}\right)^2 =$$

$$[H_{FMR}\cos(\theta_H - \varphi_M) + (H_u - 4\pi M_s)\cos(2\varphi_M)] \cdot$$

$$[H_{FMR}\cos(\theta_H - \varphi_M) + (H_u - 4\pi M_s)\,cos^2(2\varphi_M)] \quad (5.3)$$

where φ_M is the angle of the equilibrium magnetization relative to the film normal direction. It is expected that as T is increased towards T_c, one has θ_H-φ_M, H_u, and $4\pi M_s$ approach zero and H_{FMR} becomes closer to $(2\pi f)/|\gamma|$ =4.89 kOe. This trend for H_{FMR} is somewhat shown in Fig. 5.5(a).

The data in Figs. 5.5(b) and 5.5(c) together indicate that the ΔH data show a clear θ_H dependence, and this dependence is very strong at lower T but less pronounced at higher T. These results agree with the expectations of the TMS process. Specifically, the strength of the TMS strongly relies on the spin-wave manifold, while the latter varies with the magnetic field direction. This gives rise to a strong θ_H dependence of ΔH_{TMS}.[61,62] With an increase in T, however, ΔH_{TMS} decreases due to its proportionality to H_u^2,'[14] and the weight of ΔH_{TMS} in ΔH decreases accordingly, leading to a weaker θ_H dependence. It should be noted that the ΔH vs. θ_H data in Fig. 5.5(c) seem to show more than one peak. This multi-peak behavior differs from the TMS-associated single-peak responses discussed in Refs. [61] and [62], but was also observed previously.[74] Future studies are of great interest that confirm the existence of the second peak at θ_H>65° and explore its physical origin.

Further, the data in Figs. 5.5(b) and 5.5(c) also suggest that near T_c the SF-MES process makes notable contributes to ΔH and $\Delta H_{SF\text{-}MES}$ is comparable to ΔH_{TMS}. This result is supported by two observations. First, the extrapolation of the data shown in Fig. 5.5(b) to T_c seems to give a nonzero ΔH value, as indicated by the dashed gray lines in the figure. Second, the data in Fig.

5.5(c) indicate a non-trivial component of ΔH that does not vary with θ_H. These observations, together with the facts that ΔH_{TMS} decreases to zero when T approaches T_c,[14] $\Delta H_{SF\text{-}MES}$ increases with T,[7,8,9] and $\Delta H_{SF\text{-}MES}$ exhibits a very weak θ_H dependence,[61,62] indicate that the SF-MES and TMS processes co-exist and make comparable contributions to ΔH at T=675 K.

One can draw the four main conclusions from the above-discussed results on the T, x, and θ_H dependences of the FMR data. (1) At temperatures about 10-45 K below T_c, which are the temperatures relevant to the writing operation, the TMS and SF-MES processes co-exist in the FePt-based HAMR media and make comparable contributions to ΔH. (2) With a decrease in T, ΔH increases due to the enhancement of the TMS process. (3) When θ_H is varied, ΔH shows a maximum at about 45°, which is an angle relevant to the writing operation. (4) The strength of the T dependence of ΔH correlates with that of the T dependence of H_u-$4\pi M_s$, while the latter can be effectively tuned by the carbon volume fraction.

5.6 Phenomenological damping parameters

One can use the ΔH data to estimate the effective damping constant α_{eff} in the Gilbert model[18,19] (in CGS units) as

$$\alpha_{eff} = \frac{\sqrt{3}|\gamma|(\Delta H)}{2(2\pi f)} \tag{5.4}$$

as well as the transversal relaxation time T_2 in the BB model[20] (in CGS units) as

$$\frac{1}{T_2} = \sqrt{3}|\gamma|(\Delta H) \tag{5.5}$$

where $|\gamma|/(2\pi)$ is close to 2.8 MHz/Oe. The estimated values together with the ΔH data are listed in Tables 5.1 and 5.2. It should be mentioned that the reason why the α_{eff} values are estimated and listed here is that the Gilbert model has been widely considered in previous studies on damping in

perpendicular media,[19,61,62,63,64,65] not that the Gilbert model is the most appropriate model to describe near-Tc magnetization dynamics. It is known that the Gilbert model assumes a conserved magnetization vector length during the relaxation, but most likely this is not the case at high T. In comparison, the BB model appears as a better model because it involves two separate relaxation processes – the longitudinal relaxation or the T_1 process, and the transversal relaxation or the T_2 process, and thereby does not assume a conserved magnetization vector.[20] Note that the TMS relaxation involves a decrease in the magnetization vector length; it could be described by the T_2 process, but not the Gilbert model.

Table 5.1. Comparison of near-T_c FMR linewidth (ΔH), effective Gilbert damping constant (α_{eff}), and the BB transversal relaxation time (T_2) for four samples with different carbon volume fractions (x). The data were measured at a field angle of θ_H=0.

x	T_c (K)	T (K)	ΔH (Oe)	α_{eff}	T_2 (ns/rad)
0%	680	670	48	0.0084	0.684
10%	710	675	195	0.0345	0.168
20%	695	673	88	0.0155	0.373
30%	705	660	86	0.0152	0.382

Table 5.2. Comparison of near-T_c FMR linewidth (ΔH), effective Gilbert damping constant (α_{eff}), and the BB transversal relaxation time (T_2) for six different field angles (θ_H). The data were measured on the "x=20%" sample.

θ_H (°)	T (K)	ΔH (Oe)	α_{eff}	T_2 (ns/rad)
0	673	88	0.0155	0.373
30	675	102	0.0180	0.322
45	675	157	0.0277	0.209
50	675	90	0.0159	0.365
55	675	98	0.0173	0.335
65	675	182	0.0321	0.180

There are four important points that should be made about the data listed in Tables 5.1 and 5.2. (1) The data in Table 8.1 indicate that by varying the carbon volume fraction one can tune the ΔH, α_{eff}, and T_2 parameters of the FePt-based HAMR media by as large as a factor of four. (2) The data in Table 8.2 show that the damping at field angles relevant to the HAMR writing operation is relatively larger. For example, the damping at θ_H=45° is about 1.8 times of that at θ_H=0°. (3) The α_{eff} values in Tables 5.1 and 5.2 represent the upper limit of the Gilbert damping constant, as ΔH may include a small contribution due to inhomogeneity line broadening.[70] This contribution

was ignored during the estimation for the reason mentioned in the discussion about the numerical fits in Fig. 5.2(b). (4) The α_{eff} values listed are all smaller than the values (0.055-0.21) measured on FePt medial materials at RT in previous studies.[63,64,65] Possible reasons for this inconsistency include that the TMS process[14] and the Fermi surface breathing-associated damping[7,8,9] make stronger contributions to the overall damping when T is decreased close to room temperature. (5) Strictly speaking, one cannot use Eq. (4) to obtain the α_{eff} values listed in Table 2. In addition to the fact that ΔH includes a contribution from the TMS which cannot be described by the Gilbert model as explained above, the calculations also assumed $\theta_H=\theta_M$. The difference between these two angles can be small near T_c, but it is definitely non-zero.

5.7 Conclusions

In summary, the near-T_c FMR of FePt HAMR media was studied in this work. The FMR linewidth (ΔH) data as a function of the sample temperature (T), the carbon volume fraction (x) in the sample, and the field angle (θ_H) were determined, and the effective Gilbert damping constant and the transversal relaxation time in the BB model were estimated. The data indicate that at temperatures about 10-45 K below T_c, the TMS and SF-MES processes co-exist and make comparable contributions to ΔH. With a decrease in T, ΔH increases due to the enhancement of the TMS process. The strength of the T dependence of ΔH correlates with that of the T dependence of H_u-$4\pi M_s$, while the latter can be effectively tuned by x. As a result, via varying x one can tune the relaxation parameters by a factor of four. The linewidth and damping parameters exhibit a strong θ_H dependence, showing a maximum at about 45°.

It should be noted that although the contributions of the TMS and SF-MES processes to the damping were found to be comparable near T_c, they were not quantized in this work. Future work is of great interest that takes FMR measurements over a wider angle range (0°-90°) as well

as frequency-dependent FMR measurements and then numerically fit the angle- and frequency-dependent linewidth data to separate and quantize those two contributions, as in previous studies.[61,62,74] Possible approaches for enabling frequency-dependent FMR measurements at high temperatures include (1) the use of multiple microwave cavities that have different dimensions and therefore have different resonant frequencies and (2) the replacement of the microwave cavity with a hot-resistant, co-planar waveguide structure that, with the help of a vector network analyzer, can allow for broadband FMR measurements.[29,30,55] The development of such broadband high-temperature FMR spectrometers is of practical interest to the magnetics community in general and the HAMR community in particular. Finally, it should also be mentioned again that it is currently unclear whether the Gilbert and BB damping terms represent appropriate models for near-T_c magnetization dynamics or not, although the corresponding damping parameters have been estimated in this work. Future studies that compare the suitability of various models in terms of describing near-T_c damping is of great interest.

So far, exchange coupling, and damping have been studied in current PMR and future HAMR media with different types of segregants. In the next chapter, and final chapter, on magnetization dynamics in recording media, both damping and exchange coupling are studied in HAMR media samples with soft capping layers. The capping layers allow for strong tunability of the magnetic properties in the FePt hard layer.

Chapter 6. Ferromagnetic resonance in hard/soft bi-layered recording media – interlayer exchange coupling and damping in the soft layer

6.1 Introduction to hard/soft bilayer coupling in recording media

Bi-layered systems that consist of a hard magnetic layer and a soft magnetic layer are of great interest. On one hand, it is fundamentally interesting to understand how the magnetic properties of one layer are influenced by the other layer via direct exchange coupling at the interface. On the other hand, the fact that the soft layer can significantly ease the magnetization reversal in the hard layer through a so-called exchange spring mechanism[75,76] makes the hard/soft bi-layered structure a very attractive material system for energy-efficient, high-density data storage applications.[77,78]

Despite the fundamental and technological importance of the hard/soft bi-layered system, systematic experimental studies on how to control the interlayer exchange coupling (IEC) and how the IEC affects the dynamics in each layer have been limited. This chapter reports on the IEC in a bi-layered structure where the hard layer is a $L1_0$-ordered FePt thin film with strong perpendicular magnetic anisotropy (PMA) and the soft layer is a thin film made of ferromagnetic transition metal (FTM) Fe, Co, or their alloys. Comprehensive FMR studies have been carried out on this bi-layered system to explore (1) how the IEC-produced effective exchange field (H_{ex}) on the soft layer varies with the soft layer thickness, the material choice of the soft layer, and the temperature and (2) how H_{ex} affects the FMR linewidth and damping of the soft layer.

The key results are as follows. First, the effective exchange field (H_{ex}) on the soft layer increases with a decrease in the soft layer thickness (d). There exists a critical thickness, below which one has $H_{ex}>4\pi M_s$ and above which one has $H_{ex}<4\pi M_s$, where $4\pi M_s$ is the saturation

induction of the soft layer. The critical thickness for this transition depends on the material of the soft layer and generally increases with a decrease in $4\pi M_s$. These results are consistent with the general expectation of $H_{ex} \propto (4\pi M_s \cdot d)^{-1}$. Second, when the temperature (T) is increased toward the Curie temperature (T_c) of the hard layer, H_{ex} drops by a larger amount than $4\pi M_s$, mainly because T_c of the hard layer is lower than that of the soft layer. Third, the damping of the soft layer increases with H_{ex}; by varying H_{ex}, the effective Gilbert damping constant (α_{eff}) can be tuned over two orders of magnitude, from 0.0055 to 0.552. Fourth, the damping of the soft layer is relatively insensitive to the choice of the material in the "$H_{ex} > 4\pi M_s$" regime but strongly depends on the material in the "$H_{ex} < 4\pi M_s$" regime. Finally, with an increase in T, the FMR linewidth of the soft layer decreases substantially in structures with relatively large H_{ex} but remains constant in structures with very small H_{ex}. The last three results can be understood in terms of the relative contributions of the intrinsic damping and the spin pumping to the overall damping. Here spin pumping refers to the process in which the magnetization precession in the soft layer pumps a spin current to the hard layer, in a manner similar to the spin pumping effect in ferromagnet/normal metal heterostructures.[79,80,81,82]

Four important points should be mentioned. (1) The hard/soft FePt/FTM system studied in this work is of great technological interest.[83,84] This is because this system has been widely

Table 6.1. Properties of the ferromagnetic transition metal (TM) layers in hard/soft FePt/TM bi-layered samples.

Material	Thickness (nm)	$4\pi M_s$ (kG)
Fe	2.7, 3.3, 4.0, 4.7	21
$Fe_{60}Co_{40}$	3.2, 4.3, 5.8	24
$Fe_{40}Co_{60}$	2.9, 4.3, 5.8, 7.2	23
$Fe_{10}Co_{90}$	3.2, 4.3, 5.8	19
Co	3.2, 4.3, 5.8	18
$Co_{95}Nd_5$	4.3, 5.8, 7.2	-

accepted as the media material for next-generation heat-assisted magnetic recording (HAMR) drives.[85] (2) The conclusions from this work are of general nature and can be applied to many other hard/soft bi-layered systems, although they were drawn from the particular FePt/FTM system. (3) Although this study does not address how the IEC varies with the properties of and affects the damping in the hard layer, this question is equally important and is worthy of being explored in the future. (4) The discussions below focus on the effective exchange field H_{ex}, which is produced by IEC. Future studies that characterize and measure IEC in bi-layered systems using other parameters, such as exchange length and effective exchange constant, are of great interest.

The study made use of twenty FePt/FTM samples which were prepared by DC sputtering under the exact same conditions by Western digital. The hard layers, grown on glass substrates,

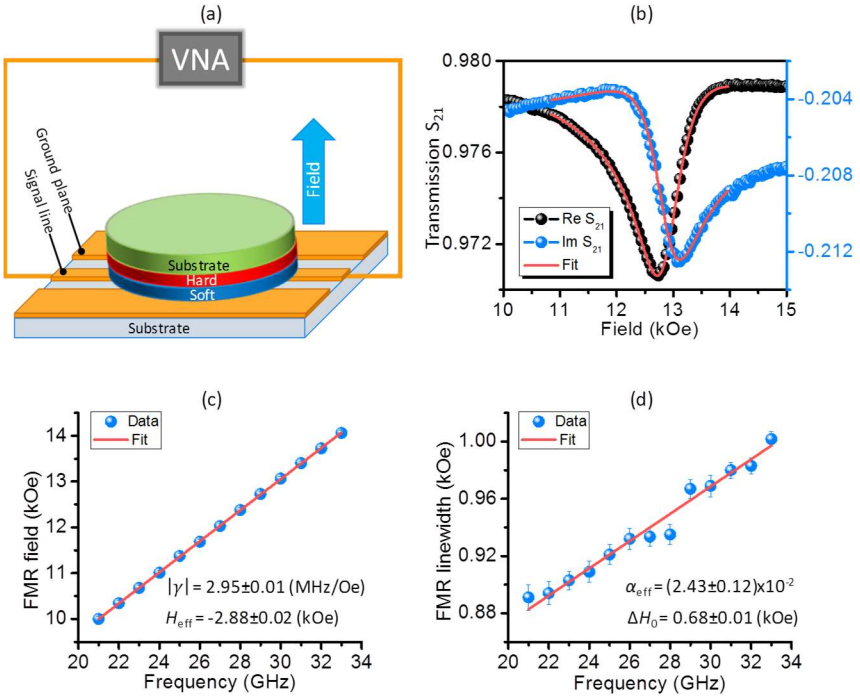

Fig. 6.1. Broadband FMR measurements. (a) Experimental configuration. (b)-(d) Representative data measured on a FePt/ $Co_{60}Fe_{40}$(4.3nm) bi-layered sample. (b) The real and imaginary parts of the complex transmission coefficient S_{21} of the CPW/sample structure measured as a function of the magnetic field at a microwave frequency (f) of 29 GHz. The dots show the data, while the red curves show numerical fits to theoretical S_{21} profiles. (c) FMR field vs. f. The blue dots present the data, while the red line is a numerical fit to Eq. (1). The fitting yields the absolute gyromagnetic ratio $|\gamma|$ and the effective internal field H_{eff}, as indicated. (d) FMR linewidth vs. f. The blue dots present the data, while the red line is a fit to Eq. (3). The fitting yields the effective Gilbert damping constant α_{eff} and the inhomogeneity line broadening contribution ΔH_0, as indicated.

are the same in all the samples. they are 10-nm-thick $L1_0$-ordered FePt granular films with the segregants at the grain boundaries made of C and SiO_2. However, the soft layers, which were grown directly on top of the hard layers, are all different. They were either made of different materials or were made of the same material but had different thicknesses. Table 6.1 lists the main properties of the soft FTM layers, where the $4\pi M_s$ values are all literature values[86]. To protect the soft FTM layers from oxidation, all the samples were capped with a 3-nm-thick carbon layer. The samples for the FMR measurements are all circles, with a diameter of about 2 mm. The FMR measurements included (1) frequency-dependent FMR measurements using a CPW and a VNA at room temperature that were discussed earlier[32,87] and (2) temperature-dependent FMR measurements using the microwave cavity discussed in the last chapter.[88]

6.2 Room temperature ferromagnetic resonance – Experimental procedure

Figure 6.1 shows the experimental configuration and representative data for frequency-dependent FMR measurements. Figure 6.1(a) sketches the experimental setup, which consists mainly of a CPW device and a VNA. The CPW has a 50-μm-wide signal line, a signal line-to-ground spacing of 25 μm, and a nominal impedance of 50 Ω. The sample is placed on the CPW with the soft layer side facing the CPW structure and the substrate side facing up. An external static magnetic field (H) is applied perpendicular to the sample plane, to either magnetize the sample to saturation or enable FMR measurements. The measurement and data analysis procedures involve the following major steps using a similar procedure from previous chapters.

(1) Magnetize the sample with a large magnetic field. For the data shown below, this field is 80 kOe.

(2) Measure the complex transmission coefficient S_{21} of the CPW/sample structure as a function of H at a fixed microwave frequency (f). Note that the field in this process is significantly

smaller than that in (1). Fig. 6.1(b) presents representative S_{21} data which were obtained at f=29 GHz with a sample where the soft layer was made of a 4.3-nm-thick $Co_{60}Fe_{40}$ film. The data show a clear resonance response, which corresponds to the FMR of the soft layer. The FMR of the hard layer is at a significantly higher frequency at room temperature, due to the strong PMA field in the hard layer.

(3) Fit numerically the real and imaginary parts of S_{21} with theoretical S_{21} profiles,[55,56] to determine the FMR field (H_{FMR}) and the FMR linewidth (ΔH). The red curves in Fig. 6.1(b) show such numerical fits.

(4) Repeat steps (1)-(3) for different microwave frequencies.

(5) Plot H_{FMR} vs. f and then fit the data, as shown in Fig. 6.1(c), using

$$f = |\gamma|(H_{\mathrm{FMR}} + H_{\mathrm{eff}}) \tag{6.1}$$

where $|\gamma|$ is the absolute gyromagnetic ratio, and H_{eff} is the effective internal field and can be written as

$$H_{\mathrm{eff}} = H_{\mathrm{ex}} - 4\pi M_{\mathrm{s}} \tag{6.2}$$

where $4\pi M_s$ is the saturation induction of the soft layer. Note that both $|\gamma|$ and H_{eff} are the fitting parameters, and for the fit shown in Fig. 6.1(c) the corresponding values are indicated in the figure.

(6) Plot ΔH vs. f and then fit the data, as shown in Fig. 6.1(d), using

$$\Delta H = \frac{2\alpha_{eff}}{|\gamma|} f + \Delta H_0 \tag{6.3}$$

where ΔH_0 is not associated with the damping but denotes the spatial sample inhomogeneity-caused line broadening. α_{eff} and ΔH_0 are the fitting parameters. The corresponding values for the fit in Fig. 6.1(d) are indicated in the figure. Note that α_{eff} describes the effective damping of the soft layer, rather than the overall damping of the entire bi-layered system, because the measured resonance is from the FMR in the soft layer, as mentioned above. However, it should also be

mentioned that it is possible to indirectly calculate the damping of the hard layer, assuming the hard layer does undergo much precession during the resonance of the soft layer.

6.3 Damping and exchange field – thickness and material dependence

Figure 6.2 presents the data obtained through the above-described procedure. Fig. 6.2(a) gives the effective internal field (H_{eff}) vs. soft layer thickness (d) data. The data show a clear trend – H_{eff} increases with a decrease in d. If one considers Eq. (6.2) and the fact that $4\pi M_s$ is usually independent of d, it can be concluded that H_{ex} is higher in samples with thinner soft layers. Note that although $4\pi M_s$ is an intrinsic property of a magnetic material, it may be possible that in ultrathin films $4\pi M_s$ decreases slightly with a decrease in d due to interfacial diffusion or surface oxidation. However, such a change in $4\pi M_s$, if any, should be relatively small, and it alone cannot account for the large H_{eff} variations shown in Fig. 6.2(a).

The data in Fig. 6.2(a) show four important results. (1) H_{ex} increases with a decrease in d, as mentioned above. (2) There exists a critical thickness (d_c). If $d>d_c$, H_{eff} is negative and one has $H_{ex}<4\pi M_s$. If $d<d_c$, H_{eff} is positive and one has $H_{ex}>4\pi M_s$. (3) d_c strongly depends on the choice of material of the soft layer; except for the samples with the Fe soft layers, the d_c value generally

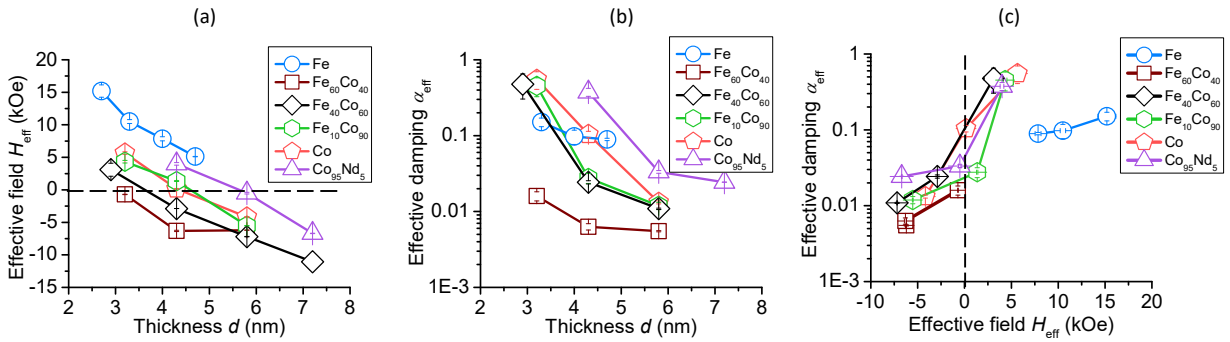

Fig. 6.2. Data from broadband FMR studies. (a) Effective internal field (H_{eff}) vs. soft layer thickness (d) for FePt/TM bi-layered samples where the soft FTM layers were made of different materials, as indicated. (b) Effective Gilbert damping constant (α_{eff}) vs. d for the same samples as for the data in (a). (c) α_{eff} vs. H_{eff}. The H_{eff} data are from (a), while the α_{eff} data are from (b).

increases with a decrease in $4\pi M_s$. (4) For a given soft layer thickness, the Fe samples show H_{ex} significantly larger than other samples.

The first three results discussed above are consistent with the general expectation of $H_{ex} \propto (4\pi M_s \cdot d)^{-1}$ in hard/soft bi-layered systems. The reason for the last result is currently unknown. One possible reason is that the first atomic layer of the Fe film near the interface may also serve as the top atomic layer of the FePt film, resulting in rather strong IEC and large H_{ex}. Those results together clearly suggest that one can tune H_{ex} in hard/soft bi-layered systems by either varying the soft layer thickness or using different materials for the soft layer.

Figure 6.2(b) presents the α_{eff} vs. d data. Two results are evident from the data. First, via varying the material and thickness of the soft layer, α_{eff} can be tuned over two orders of magnitude, with the lowest value being 0.0055 and the largest being 0.552. The physical mechanism that enables such a broad tuning range is discussed shortly.

Second, the data show a common trend - α_{eff} increases with a decrease in d. This thickness dependence is relatively weak in the Fe sample but is very strong in all other samples. For example, in the $Fe_{40}Co_{60}$ sample α_{eff} increases by a factor of 43.8 when d is decreased from 5.8 nm to 2.9 nm. There are two possible reasons for the observed thickness dependence. First, the overall damping in a magnetic thin film may contain a contribution from two-magnon scattering[6,12,14] associated with surface roughness or defects on the surface or at the interface; the weight of this contribution in the total damping is usually larger in thinner films. However, it seems that this mechanism alone cannot explain the rather big α_{eff} changes shown in Fig. 6.2(b), if one takes into account that the two-magnon scattering is very weak in films magnetized perpendicularly.[61,89] Second, the observed thickness dependence may be associated mainly with the thickness dependence of H_{ex}, since the data in Figs. 6.2(a) and 6.2(b) seem to show similar overall trends.

To clarify the above conjecture about the dominant physical mechanism for the strong thickness dependence shown in Fig. 6.2(b), α_{eff} is plotted against H_{eff} in Fig. 6.2(c). One can clearly see that α_{eff} increases with H_{eff}. This response suggests that α_{eff} increases notably with H_{ex} and the d dependence shown in Fig. 6.2(b) is associated mainly with the change of H_{ex} with d, not the two-magnon scattering process. In addition, one can also see that the top-most four data points over the 3-6 kOe field range show similar α_{eff} values, while the left-most five points in a relatively narrower field range show very different α_{eff} values, varying by a factor of 5. This result indicates that in the "$H_{ex}>4\pi M_s$" regime, α_{eff} is insensitive to the choice of the material of the soft layer; in contrast, in the "$H_{ex}<4\pi M_s$" regime, α_{eff} strongly depends on the choice of the material.

The above results about the damping can be understood by considering the presence of two distinct components in the overall damping constant, namely, $\alpha_{eff} = \alpha_0 + \alpha_{sp}$, where α_0 denotes the intrinsic damping of the soft layer, while α_{sp} describes the extrinsic damping due to the pumping of spin by the precessional motion in the soft layer to the hard layer. As the spin pumping is associated with the IEC, α_{sp} increases with H_{ex}. This results in the increasing response shown in Fig. 6.2(c). As H_{ex} can be tuned over a wide range by varying the choice of the material and the thickness of the soft layer, as shown in Fig. 6.2(a), α_{sp} can be changed over a wide range too, giving rise to the wide tuning range of the overall damping α_{eff} (two orders of magnitude) shown in Fig. 6.2(b). In the samples with large H_{ex}, α_{sp} can be significantly larger than α_0, which explains the insensitivity of α_{eff} to the choice of the material shown by the top-most four data points in Fig. 6.2(c). In contrast, in the samples with relatively low H_{ex}, α_{sp} is either comparable to or smaller than α_0, giving rise to the strong dependence of α_{eff} on the choice of the material shown by the left-most five data points in Fig. 6.2(c). Note that α_0 in ferromagnetic FTM thin films results mostly from spin-flip magnon-electron scattering (or inter-band scattering) and Fermi surface breathing-

associated magnon-electron scattering (or intra-band scattering), with the former being dominant at high temperatures while the latter being dominant at low temperatures.[7,8,9,10] Such scattering strongly depends on the properties of band structures in the material, so α_0 is usually material dependent. Note that magnon-photon scattering and eddy current can also contribute to the overall damping, but their contributions should be much smaller than the damping associated with the magnon-electron scattering in the samples studied in this work.

It should be highlighted that, as shown in Fig. 6.2(c), the α_{eff} values of the three Fe samples seem to be off-trend. The actual reason for this is unknown currently, but it may share the same origin as the unusual H_{ex} response of the Fe samples discussed above. Two points should be made about the α_{eff} values of the Fe samples. First, they are all substantially larger than the literature α_0 value in Fe, which is about 0.002.[90] This is likely associated with the presence of the very strong IEC in the Fe samples. Second, they show a H_{eff} dependence much weaker than the α_{eff} values in other samples. This is probably because all the three Fe samples are in the "$H_{\text{ex}}>4\pi M_{\text{s}}$" regime, while the other samples exhibit different H_{ex} strengths.

Two notes should be made about the above discussions on the data in Fig. 6.2. First, the FMR analysis processes described above take a small-damping approximation, namely, $(\alpha_{\text{eff}})^2<<1$. In the case where the damping is strong, "$(\alpha_{\text{eff}})^2<<1$" is not true anymore and a full numerical analysis of the S_{21} data is needed. The top-most four data points in Fig. 6.2(c) were obtained through the full analysis that did not take the small-damping approximation. Details about this analysis are provided near the end of this chapter. Second, 20 samples were measured in the experiments, but Fig. 6.2(b) shows the data for 18 samples only. This is because only a few frequency points were obtained for the 4.7-nm-Fe sample and the 2.9-nm-$Fe_{40}Co_{60}$ sample due to

experimental limitations. While the data were enough to reliably determine H_{eff}, they did not provide enough information to calculate α_{eff}.

6.4 High temperature ferromagnetic resonance – experimental procedure

The data presented above were all measured at room temperature. Turn now to the high-temperature (T) FMR measurements and analyses. Fig. 6.3 shows the high-T FMR approach. Fig. 6.3(a) shows a schematic diagram of the experimental system. This is the same system used in the previous chapter. The main components include a rectangular microwave cavity (purple), a diamond rod (yellow) with a diameter of 2 mm that loads the sample (red) into the cavity, and a ceramic heater (gray) that heats the sample through the diamond rod. These components are housed in a high-vacuum chamber, and the measurements are performed at a pressure of about 6.7×10^{-3} Pa (or about 5×10^{-5} Torr) to prevent changes in sample properties due to oxygen during high-T measurements as well as to reduce temperature fluctuations during the FMR measurements. For the FMR data presented below, f was kept constant at 13.7 GHz, which was also the resonant frequency of the microwave cavity, while H was swept. Prior to placing the sample in the FMR system, the sample was saturated by a perpendicular magnetic field of H=80 kOe at room

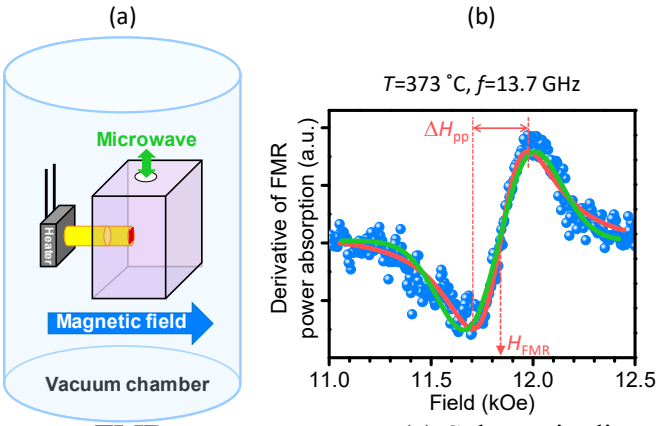

Fig. 6.3. High-temperature FMR measurements. (a) Schematic diagram of the experimental setup. (b) Representative FMR power absorption data (blue dots), a Lorentzian fit (red curve), and a Gaussian fit (green curve). The data were measured at T=373 °C on a FePt/Co(5.8nm) bi-layered sample. The Lorentzian fit-yielded FMR field H_{FMR} and peak-to-peak FMR linewidth ΔH_{pp} are indicated in (b).

temperature. After placing the sample in the FMR system and heating it, prior to each FMR measurement the sample was magnetized by a field of H=15 kOe. More details about this approach are provided in the previous chapter or in Ref. [88].

Fig. 6.3(b) presents the FMR data (blue dots) measured at T=373 °C on a sample where the soft layer was made of a 5.0-nm-thick Co film. The red curve shows a numerical fit to the derivative of a Lorentzian trial function. The Lorentzian fitting-yielded FMR field (H_{FMR}) and peak-to-peak FMR linewidth (ΔH_{pp}) are indicated in the figure. Note that one has $\Delta H_{pp}= \Delta H/\sqrt{3}$. A fit (green curve) to the derivative of a Gaussian trial function is also included in the figure. One can see that the Lorentzian fit is slightly better than the Gaussian fit, indicating that the inhomogeneity line broadening contribution, if any, to ΔH_{pp} is relatively small. In the case that a film sample has strong spatial inhomogeneity and the associated line broadening (ΔH_0) is large, the Gaussian function would fit the FMR data better than the Lorentzian function.[70]

The above-described high-T approach was used to study FMR in three samples whose soft layers were made of a 5.8-nm-thick $Co_{95}Nd_5$ film, a 7.2-nm-thick $Co_{95}Nd_5$ film, and a 5.8-nm-thick Co film, respectively. These three samples were chosen because they show moderate α_{eff} at room temperature, as shown in Fig. 6.2(b). The samples with larger α_{eff} values showed smaller signal-to-noise ratios in high-T FMR measurements. The measurements were carried out over a temperature range of T=25-600 °C. The measurement data are presented in Fig. 6.4.

6.5 Linewidth and exchange field – temperature dependence

Figure 4(a) gives H_{eff} as a function of T, where the H_{eff} data were calculated using Eq. 6.1 with the experimentally measured H_{FMR} data (see Fig. 6.3(b)) and a gyromagnetic ratio of $|\gamma|$=2.8 MHz/Oe. Two main results are evident from the data in Fig. 4(a). First, in all the samples H_{eff} decreases with an increase in T. This result is most likely associated with the fact that the hard

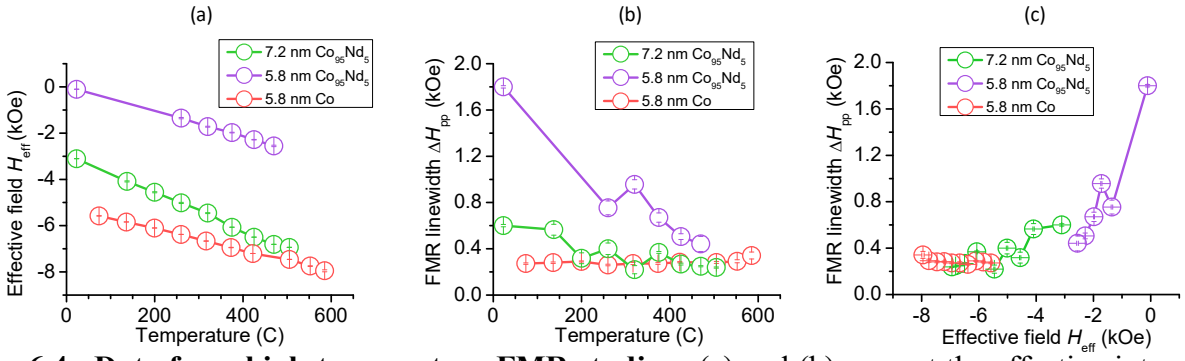

Fig. 6.4. Data from high-temperature FMR studies. (a) and (b) present the effective internal field (H_{eff}) and the FMR linewidth (ΔH_{pp}), respectively, as a function of temperature for three samples with different soft layers, as indicated. (c) plots ΔH_{pp} as a function of H_{eff}. The ΔH_{pp} data are from (b), while the H_{eff} data are from (a).

FePt layer has a Curie temperature of around $T_c \approx 425$ °C[88] while the soft FTM layers usually have a much higher T_c. For example, T_c in bulk Co is about 1130 °C.[91] T_c in Co thin films may be slightly lower than 1130 °C but should be substantially higher than 425 °C.[92] Thanks to this difference in T_c, $4\pi M_s$ in the FePt layer drops faster than that in the soft FTM layer when T is increased toward 600 °C. The net effect is that with an increase in T, H_{ex} drops by a larger amount than the $4\pi M_s$ of the FTM layer and H_{eff} decreases accordingly. Note that H_{ex} strongly depends on the magnetic moment in the hard FePt layer. Second, the 5.8-nm $Co_{95}Nd_5$ sample shows larger H_{eff} values than the other two over the entire T range, indicating larger H_{ex} in this sample. This is because the soft FTM layer in this sample is thinner than in the 7.2-nm $Co_{95}Nd_5$ sample and has a smaller $4\pi M_s$ value than in the 5.8-nm Co sample. Thus, this result is generally consistent with the conclusion drawn from the data in Fig. 6.2(a).

Figure 6.4(b) presents the ΔH_{pp} vs. T data of the three samples. One can see that the T dependence of ΔH_{pp} differs remarkably in the three samples. ΔH_{pp} in the 5.8-nm $Co_{95}Nd_5$ sample shows a rather strong T dependence; ΔH_{pp} decreased by a factor of 5 when T was increased from 23 °C to 467 °C. In contrast, ΔH_{pp} in the 7.2-nm $Co_{95}Nd_5$ sample shows a much weaker T dependence, and ΔH_{pp} in the 5.8-nm Co sample is almost constant.

This result can be understood in terms of the T dependence of the two damping components in Eq. 6.4. Specifically, over the T range considered here α_0 results mainly from spin-flip magnon-electron scattering. This scattering process requires both the momentum and energy conservations which can be satisfied more easily at high T.[7,8,9] As a result, α_0 is expected to increase with T. In contrast, α_{sp} is expected to decrease with T because IEC is weaker and H_{ex} is smaller at higher T as suggested by the data presented in Fig. 6.4(a).

For the 5.8-nm $Co_{95}Nd_5$ sample, H_{eff} is almost zero at room temperature, as shown in Fig. 6.4(a), indicating $H_{ex} \approx 4\pi M_s$. This means that IEC in this sample is relatively strong and α_{sp} dominates over α_0 at room temperature. With an increase in T, IEC becomes weaker and α_{sp} becomes smaller, giving rise to the large ΔH_{pp} drop shown in Fig. 6.4(b).

The situation is completely different in the 5.8-nm Co sample. In this sample, H_{eff} is very small, as shown in Fig. 6.4(a). This indicates that IEC is relatively weak and α_{sp} may be comparable with α_0. With an increase in T, α_{sp} decreases while α_0 increases, resulting in an overall flat response for ΔH_{pp}, as shown in Fig. 6.4(b). When T is close to or higher than T_c, α_{sp} becomes so small and α_0 starts to become dominate. Since α_0 increases with T as discussed above, ΔH_{pp} shows a slight increase over the T range of 500-600 °C.

In addition, the data in Fig. 6.4(b) also show that the three samples show comparable ΔH_{pp} values near T_c, although they show very different ΔH_{pp} values near room temperature. This observation supports the above interpretation. In brief, near room temperature H_{ex} is very different in the three samples, resulting in very different α_{sp} values and very different ΔH_{pp} values. Near T_c, IEC becomes absent in all the samples, resulting in negligible α_{sp} and comparable ΔH_{pp} values.

One can clearly see from the above discons that IEC plays critical roles in the T dependence of the FMR linewidth. To further illustrate this, ΔH_{pp} is plotted against H_{eff} in Fig. 6.4(c), in a way

similar to the plot in Fig. 6.2(c). Note that both the changes of H_{ex} and $4\pi M_s$ with T contribute to the variation of H_{eff}, but H_{ex} plays a bigger role due to the difference in T_c between the FePt and FTM layers, discussed above. The plot surprisingly shows the same trend as the one in Fig. 6.2(c), even though the data here were measured at very different temperatures while all the data in Fig. 6.2(c) were measured at the same temperature, namely, the room temperature. This consistency evidently confirms the above-discussed H_{ex}-damping correlation.

One can also see from the data in Fig. 6.4(c) that even though the overall trend is the increase of ΔH_{pp} with H_{eff}, the slope varies notably with H_{eff}, large in the relatively high H_{eff} region and almost zero in the very low H_{eff} region. This is consistent with the above interpretation of the ΔH_{pp} data presented in Fig. 6.4(b).

6.6 Ferromagnetic resonance analysis with large damping

This section describes how to extract the FMR field and linewidth parameters in magnetic thin films with large damping from the broadband FMR measurement data using the Gilbert damping model described in chapter 2. It should be noted that many of these equations have been listed previously in this dissertation. However, for the ease of following the derivation, they will be given again with extra steps in between that were previously omitted. It is known that the power absorbed during an FMR measurement (in CGS units this time) is given by

$$P = -\frac{1}{2}\omega|h_0|^2 Im(\chi) \tag{6.4}$$

where ω is the angular frequency of the external microwave, h_0 is the amplitude of the microwave field, and χ is the magnetic susceptibility of the film. $-Im(\chi)$ can be derived from the Gilbert equation in the usual manner

$$-Im(\chi) = \frac{\frac{\omega_M}{4\pi}\left[\alpha\omega_y^2 + \alpha\omega^3(\alpha^2+1)\right]}{\left\{\left[\left(\omega_x\omega_y\right)^2 - \omega^2(\alpha^2+1)\right]^2 + \alpha^2\omega^2\left(\omega_x+\omega_y\right)^2\right\}} \tag{6.5}$$

where α is the Gilbert damping constant. There have been no assumptions based on the value of α, whereas previous works (and chapter 2) have utilized $\alpha^2 \ll 1$. ω_M in Eq. (6.5) is defined as

$$\omega_M = |\gamma| 4\pi M_s \tag{6.6}$$

where $|\gamma|$ is the absolute gyromagnetic ratio and is usually close to $2\pi \times 2.8$ MHz/Oe. Because only the out-of-plane configuration is of interest, one can write

$$\omega_x = \omega_y = |\gamma|(H_{FMR} + H_{eff}) \tag{6.4}$$

where H_{eff} is the effective internal field given by

$$H_{eff} = H_{ex} - 4\pi M_s \tag{6.5}$$

and H_{FMR} is the external static magnetic field applied perpendicular to the film plane. Following the previous methods for deriving an equation for the FMR linewidth, the first step is to find the maximum power and then divide it by 2 to find the half maximum power. To do so, one evaluates

$$\frac{\partial P}{\partial H_0}\Big)_{\omega} = 0 \tag{6.6}$$

Since the applied field is the quantity that is changing during the measurements, the frequency is considered to be fixed. The value of H_{FMR} that satisfies Eq. (6.5) by making P a maximum is

$$H_{Pmax} = \frac{\omega}{|\gamma|}\sqrt{2\sqrt{\alpha^2+1} - \alpha^2 - 1} - H_{eff} \tag{6.7}$$

In the limit of $\alpha^2 \ll 1$, the resonance condition for zero damping is recovered. The second step is to find H_{FMR} at both half maximum values as well. To do this, one writes

$$\frac{1}{2}P(H_{Pmax}) = P(H_0) \tag{6.8}$$

With Eq. (6.4), Eq. (6.11) can be rewritten as

$$\frac{1}{2}Im\big(\chi(H_{Pmax})\big) = Im\big(\chi(H_0)\big) \tag{6.9}$$

Eq. (6.12) gives two solutions for H_{FMR}. One is for the half maximum on the left side of the peak,

while the other is for the half maximum on the right side of the peak. The difference in these two will give the FMR linewidth ΔH. One can convert ΔH to a peak-to-peak linewidth by

$$\sqrt{3}\Delta H_{\mathrm{pp}} = \Delta H \tag{6.10}$$

The above procedure gives rise to a linewidth as

$$\Delta H = G(\alpha)\frac{2f}{2\pi|\gamma|} \tag{6.11}$$

where $G(\alpha)$ is given by

$$G(\alpha) = x - y \tag{6.12}$$

$$x = \sqrt{\frac{(\alpha^2-\sqrt{\alpha^2+1}+1)\alpha+\alpha\sqrt{(\alpha^2-\sqrt{\alpha^2+1}+1)^2-\frac{\alpha^2}{4}(\alpha^2+1)+\sqrt{\alpha^2+1}(\alpha^2-\sqrt{\alpha^2+1}+1)}+\frac{\alpha}{4}\sqrt{\alpha^2+1}-\frac{\alpha^3}{4}\sqrt{\alpha^2+1}}{\alpha\sqrt{\alpha^2+1}}}$$

$$y = \sqrt{\frac{(\alpha^2-\sqrt{\alpha^2+1}+1)\alpha-\alpha\sqrt{(\alpha^2-\sqrt{\alpha^2+1}+1)^2-\frac{\alpha^2}{4}(\alpha^2+1)+\sqrt{\alpha^2+1}(\alpha^2-\sqrt{\alpha^2+1}+1)}+\frac{\alpha}{4}\sqrt{\alpha^2+1}-\frac{\alpha^3}{4}\sqrt{\alpha^2+1}}{\alpha\sqrt{\alpha^2+1}}}$$

The equation (given back in chapter 3) used to fit the real and imaginary parts of the complex transmission coefficient S_{21} is

$$S_{21} = S_{21}^0 + DH + \frac{\chi}{2\chi_0} \tag{6.13}$$

where the first term on the right side describes the electronic background, the second denotes the electronic drift during the sweeping of the field, and χ_0 is the usual fitting parameter that has experimental parameters built in. Each term in Eq. (6.13) has a real part and an imaginary part associated with it, namely,

$$S_{21}^0 = \mathrm{Re}(S_{21}^0) + i\mathrm{Im}(S_{21}^0) \tag{6.14}$$

$$DH_{\mathrm{FMR}} = \mathrm{Re}(DH_{\mathrm{FMR}}) + i\mathrm{Im}(DH_{\mathrm{FMR}}) \tag{6.15}$$

$$\frac{\chi}{\chi_0} = \mathrm{Re}\left(\frac{\chi}{\chi_0}\right) + i\mathrm{Im}\left(\frac{\chi}{\chi_0}\right) \tag{6.16}$$

where $\chi = \chi_R + i\chi_I$ and $\chi_0 = \chi_{0R} + i\chi_{0I}$ so that

$$\frac{\chi}{\chi_0} = \frac{1}{\chi_{0R}^2 + \chi_{0I}^2}[(\chi_{0R}\chi_R + \chi_{0I}\chi_I) - i(\chi_{0R}\chi_I + \chi_{0I}\chi_R)] \tag{6.17}$$

The imaginary part χ_I was given earlier for finding the linewidth. The real part is

$$\chi_R = \frac{\frac{\omega_M}{4\pi}\left[\omega_y^3 + \omega_y\omega^2(\alpha^2 - 1)\right]}{\left\{\left[\omega_y^2 - \omega^2(\alpha^2 + 1)\right]^2 + 4\alpha^2\omega^2\omega_y^2\right\}} \tag{6.19}$$

The parameter S_{21}^0, D, and χ_0 have physical information about the VNA-FMR setup and sample built in and must be determined through the fitting of the FMR profile.

The Gilbert damping constant can be obtained by fitting the resonance profile with Eq (6.16). Obtaining the damping constant at different frequencies shows a decrease in the damping constant with increasing frequency. However, the Gilbert damping constant is frequency independent, and this apparent change is actually due to inhomogeneous broadening of the FMR linewidth because of inhomogeneous sample properties. To reconcile this problem, Eq. (6.14) is used at each frequency to calculate a linewidth for the FMR profile. The real damping constant can then be obtained by fitting the linewidth vs. frequency using the following equation

$$\Delta H = G(\alpha)\frac{2f}{2\pi|\gamma|} + \Delta H_0 \tag{6.20}$$

where ΔH_0 is the linewidth contribution due to inhomogeneous broadening and is frequency independent. This fitting yields the true Gilbert damping constant which does not change with frequency. It should be noted that the only thing new here is that the derivation now includes extra terms involving the Gilbert damping constant.

6.7 Conclusions

In summary, broadband ferromagnetic resonance (FMR) and high-temperature (*T*) FMR measurements had been carried out to study interlayer exchange coupling (IEC) in a magnetic

hard/soft bi-layered system where the hard layer was a $L1_0$-ordered FePt thin film and the soft layer was a ferromagnetic transition metal (FTM) thin film. The data indicate that the IEC-produced exchange field (H_{ex}) on the soft layer strongly depends on the choice of material of the soft layer as well as the soft layer thickness. The thinner the soft layer is and the smaller $4\pi M_s$ the soft layer has, the larger the field H_{ex} is. With an increase in T, H_{ex} drops by a larger amount than the $4\pi M_s$ of the soft layer, resulting in an internal field that decreases with T. The IEC strongly affects the FMR linewidth and damping of the soft layer. The general trend is that both the FMR linewidth (ΔH) and the effective Gilbert damping constant (α_{eff}) increases with H_{ex}, but there are also several subtle effects associated with H_{ex}. In the $H_{ex}>4\pi M_s$ regime, α_{eff} is insensitive to the choice of material of the soft layer; in the $H_{ex}>4\pi M_s$ regime, however, α_{eff} strongly depends on the choice of material. With an increase in T, ΔH decreases substantially in samples where H_{ex} is relatively large, but remains constant or even increase slightly in samples where H_{ex} is very small.

This chapter concludes the studies of exchange fields and damping in magnetic recording media at room and elevated temperatures. In chapter 4, intergranular exchange coupling was quantified for media with different SiO_2 segregant amounts. Chapter 5 looked at damping in next generation media with different carbon segregant amounts near the Curie temperature of the hard media layer. In this final chapter for magnetic recording media, both exchange fields due to interlayer hard/soft coupling and damping were studied in next generation media with hard/soft bilayer coupling at room and elevated temperatures. In the next two chapters, spin wave dynamics in yttrium iron garnet films with periodic and random patterns are studied. The periodic patterns give rise to spin-wave fractals in the nonlinear regime, while the random patterns show Anderson localization.

Chapter 7. Spin waves in YIG strips with periodic patterns – observation of exact fractals

7.1 Nonlinear dynamics and fractals

A fractal is a shape made of parts each of which is similar to the whole in some way. One can group fractals into two main categories, (i) exact fractals (or regular fractals) in which the same feature replicates itself on successively smaller scales and (ii) statistical fractals (or random fractals) that display statistically similar features.[93,94,95] Statistical fractals have been observed in a rather wide variety of physical systems, ranging from material structures to lungs in human bodies and stock price fluctuations. In stark contrast, exact fractals are relatively rare in nature, though they can be very easily constructed by mathematical models. Examples of exact fractals include optical fractals formed using self-similar structures.[96,97]

Despite the above facts, exact fractals have been found in nonlinear dynamics, which is rather surprising in view of the strong sensitivity of nonlinear systems. They are (1) space-domain soliton fractals, demonstrated numerically, and (2) time-domain soliton fractals, observed experimentally. The realization of (1) relied on the use of a one-dimensional (1D) nonlinear waveguide that consists of different sections, each with a larger dispersion coefficient D than the prior section.[98,99] As a soliton in the first section enters the next section, it experiences an abrupt increase in D and thereby breaks up into several smaller solitons or daughter solitons. When the daughter solitons enter the next section, each of them undergoes another breakup and produces even smaller solitons or granddaughter solitons. Thus, successive changes in D create soliton fractals along the waveguide.

The demonstration of (2) made use of a feedback ring that consisted of a 1D nonlinear media, and an amplifier that amplified the output signal from the media and then fed it back to the

input of the media.[100] With an appropriate amplification, a single soliton is self-generated in the ring; as the soliton circulates in the ring, its amplitude varies in a fractal manner, yielding a time-domain fractal. In this case, the amplifier ensures sufficient nonlinearity needed to maintain the soliton, while the periodic feedback modifies the wave dispersion to enable the fractal dynamics.

7.2 Spin-wave fractals using magnonic crystals

This chapters report on the observation of a new type of exact fractals in nonlinear dynamics that, in contrast to (1) and (2), form spontaneously out of the constituent media, without being forced into being, and do not involve solitons. To make an analogy, there is a strong difference between spontaneous symmetry breaking, integral to the theory of phase transitions, and forcing symmetry-breaking. The observation uses nonlinear media in which a spatial periodic potential is introduced to create strong dispersion that facilitates the formation of a fractal. The experiments utilize a quasi-1D magnonic crystal[101,102,103,104,105,106,107,108,109] that consists of a long and narrow magnetic $Y_3Fe_5O_{12}$ (YIG) film strip with periodic transversal lines etched into the film. This medium supports the propagation of spin waves. The etched lines create a periodic potential for spin waves, and the latter leads to significant modification to the spin-wave dispersion curve at certain wavenumbers associated with the dimensions of the periodic lines.[102,103] Upon the excitation of a continuous spin wave in one end of the media, the spin wave propagates to the other end, resulting in an output signal that manifests itself as a single peak in the power-frequency spectrum. With an increase in the input power P_{in}, the initial peak (or the mother) can produce additional side peaks (or the daughters) in the frequency range with strong dispersion through modulational instability (MI),[93,110,111,112] resulting in a comb-like frequency spectrum. As P_{in} is further increased, each peak in the comb evolves into its own, finer frequency comb

(granddaughters), also through the MI. Such frequency fractals, which are illustrated in Fig. 7.1, manifest themselves as multiple layers of amplitude modulation in the time-domain signal.

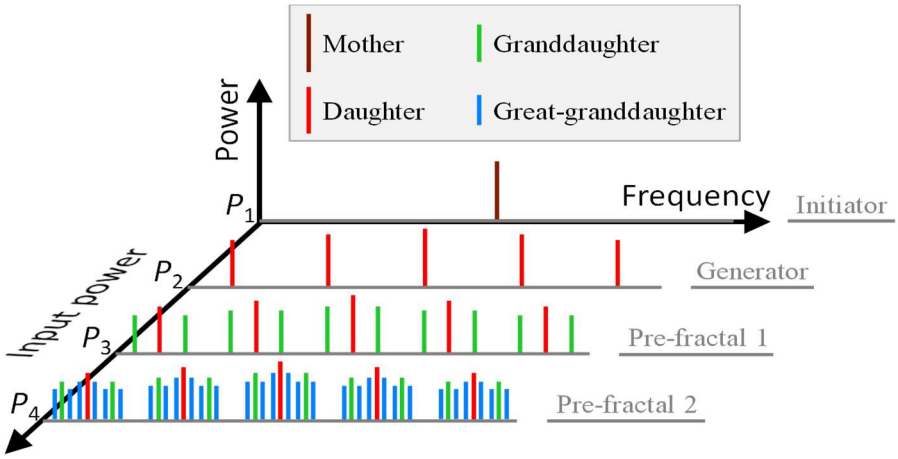

Fig. 7.1. Illustration of the development of a frequency fractal with an increase in the input power (P_1<P_2<P_3<P_4).

Three important points should be highlighted. First, the new fractals in this work are fundamentally different from (1) and (2). On the one hand, (1) and (2) are for solitons, which involve a fine balance between the dispersion-induced pulse broadening and nonlinearity-caused self-narrowing,[98,99,100] while the new fractals do not require such a balance. In this aspect, this work indicates that exact fractals in nonlinear systems do not have to involve solitons. On the other hand, the new fractal relies on a completely different approach to realize the conditions needed for fractal formation; it makes use of spatial periodic potentials to achieve strong dispersion required by fractal generation, while (1) and (2) use successively increased dispersion and periodic feedback, respectively, to interrupt soliton dynamics and realize soliton fractals. Thus the new fractals are spontaneous, not forced. Second, the approach in this work is of a general nature and can be applied to achieve similar fractals in other nonlinear systems, including electromagnetic transmission lines, optical fibers, and water waves. Finally, in addition to advancing the field of

fractals, the results also help interpret various nonlinear effects in magnonic crystals, such as instability and nonlinear damping.[107,109]

7.3 Spin wave characterization

The experimental configuration is sketched in Fig. 7.2(a). The experiments made use of a quasi-1D magnonic crystal that consisted of a 10-mm-long, 2.5-mm-wide, 10.3-μm-thick YIG film strip with 12 lines etched into the film. Each etched line is 50 μm wide and 3.3 μm deep, and the spacing between the lines is 400 μm. Backward volume spin waves[3,113] are excited by placing a microstrip line on one end of the YIG strip and feeding it with microwaves, and are detected by a second microstrip line placed on the other end of the YIG strip. The separation of the two microstrip lines are about 5.5 mm. The magnetic field, indicated by the red arrow, is kept constant at 1175 Oe. Figures 7.2(b) and 7.2(c) show the transmission profile and frequency (f) vs.

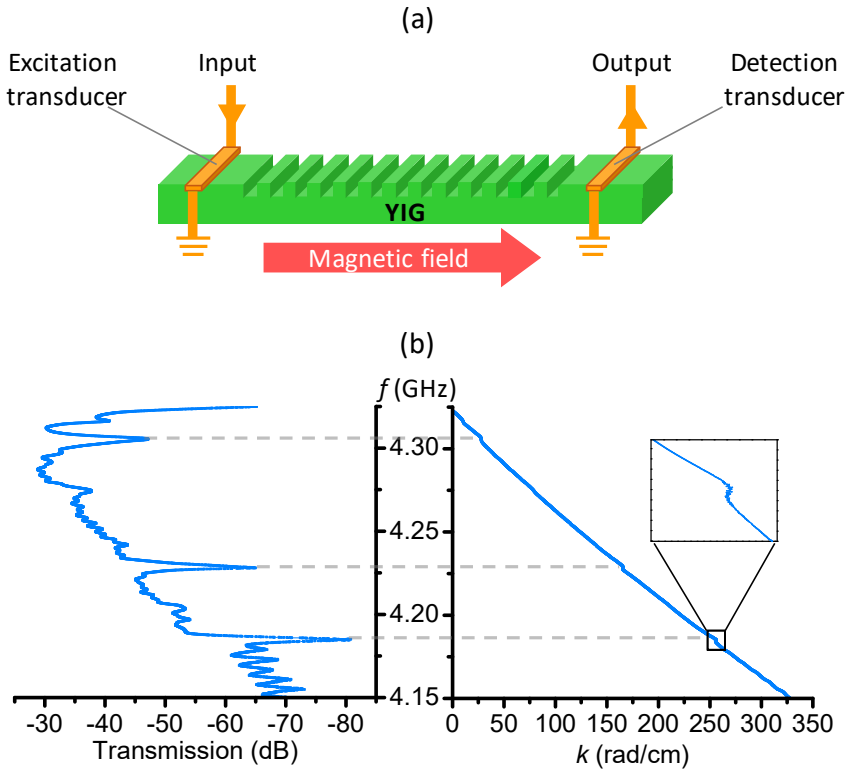

Fig. 7.2. Spin wave configuration and characterization. (a) Experimental configuration. (b) Transmission profile (left) and frequency f vs. wavenumber k dispersion curve (right) measured with a YIG-based 1D magnonic crystal for P_{in}=0.7 mW.

wavenumber (k) dispersion curve, respectively, obtained from the complex transmission coefficient measurements on the magnonic crystal. The strong dips in the transmission profile and the corresponding jumps in the dispersion curve represent unique characteristics of the magnonic crystal[102,103,109] that result from the periodically etched lines.

The data in Fig. 7.2(b) were measured with a relatively low input power (P_{in}=0.7 mW) over a relatively wide f range using a vector network analyzer. In contrast, Fig. 7.3 presents the data measured at a significantly higher power (P_{in}=7 W) over a much narrower f range which are both

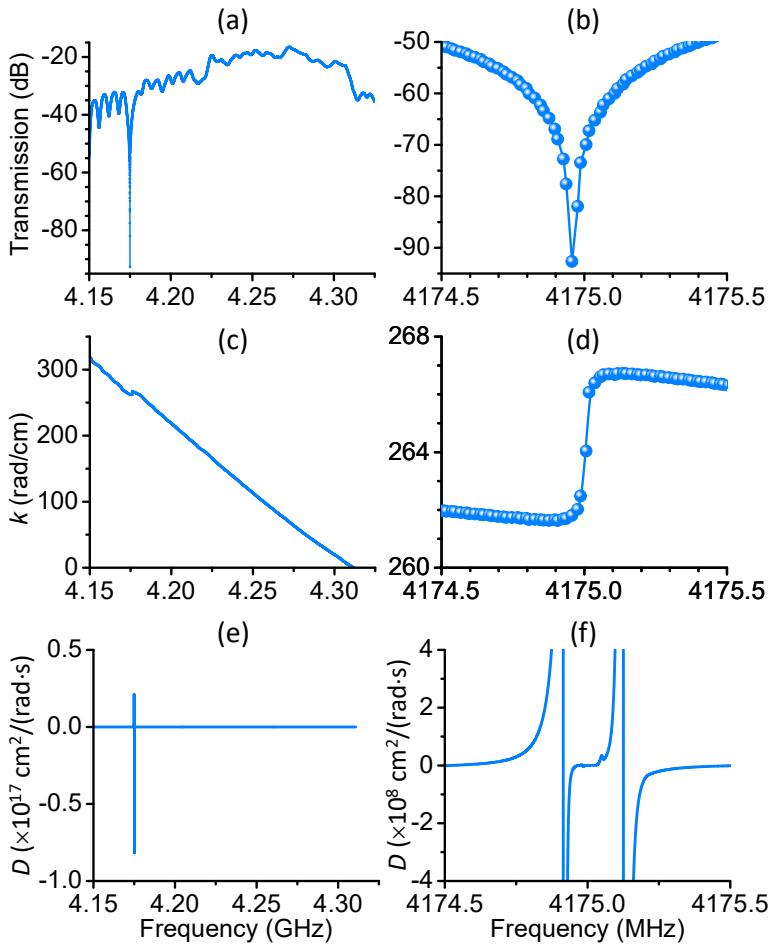

Fig. 7.3. Spin wave transmission and dispersion. The first and second rows show the transmission profile and the frequency vs. wavenumber (k) dispersion curve, respectively, measured with a YIG-based 1D magnonic crystal for P_{in}=7 W. The third row shows the dispersion coefficients (D) calculated based on the dispersion curves in the second row. The right column shows the same data as in the left column but over a much narrower frequency range.

relevant to the fractal measurements described later. The dispersion data, shown by the dots in Figs. 7.3(b) and 7.3(c), were interpolated to produce dispersion curves, shown by lines, and the latter were used to numerically determine the dispersion coefficient $D = \frac{d^2(2\pi f)}{dk^2}$ presented in Figs. 7.3(e) and 7.3(f). The data in Fig. 7.3 clearly show that, as one sweeps f across a transmission dip, the dispersion coefficient D can become substantially large and can even flip its sign. To be more specific, $|D|$ is about 10^3 cm^2/(rad·s) in the off-dip region, which is close to typical values in continuous YIG thin films,[3] but can be seven orders of magnitude larger in the transmission dip. It is this strong dispersion that enables the formation of the fractals presented below.

7.4 Experimental observation – frequency domain

Figure 7.4 shows four power-frequency spectra measured at different P_{in}, as indicated, using a spectrum analyzer that demonstrate the development of the spin-wave fractals. At P_{in}=0.7 mW, the spectrum consists of only one peak, as shown in Fig. 7.4(a), at the frequency that is exactly equal to the input frequency. This peak corresponds to the initiator or the mother shown in Fig. 1. As P_{in} is increased to 7 W, several new side peaks are generated through the MI,[93,110,111,112] and the initial single-peak spectrum evolves into a frequency comb, as shown in

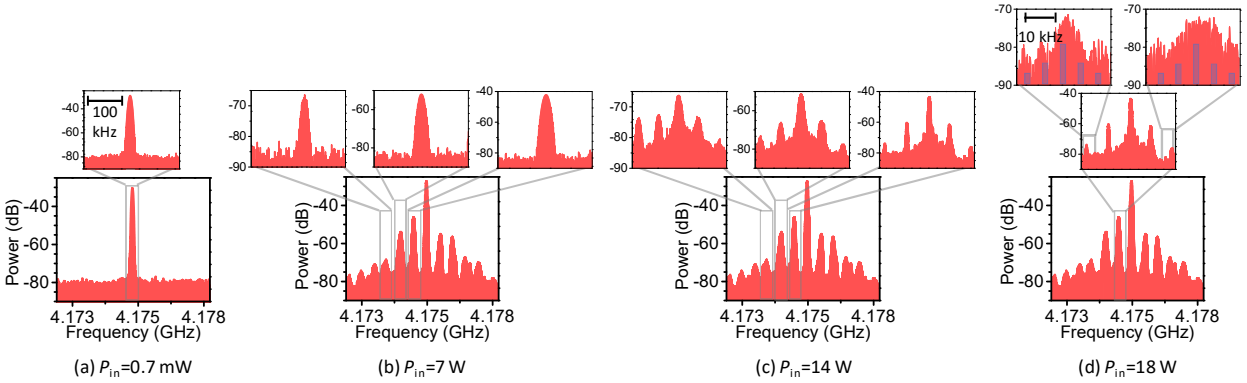

Fig. 7.4. Power-frequency spectra measured at different P_{in}, as indicated, demonstrating fractal development. The diagrams in the middle and top rows share the same frequency scale indicated in the left-most diagram in each row. The vertical bars in the top-row diagrams serve as visual guides to indicate the positions of the frequency peaks.

Fig. 7.4(b). The comb spectrum corresponds to the generator in Fig. 7.1, and the new peaks can be termed as daughter modes. With a further increase in P_{in}, each peak in the comb develops its own, finer comb (granddaughters), as shown in Fig. 7.4(c), also through the MI. As P_{in} is increased further, each granddaughter generates several great-granddaughters, as shown in Fig. 7.4(d). The spectra in Figs. 7.4(c) and 7.4(d) correspond to pre-fractal 1 and pre-fractal 2, respectively.

7.5 Experimental observation – time domain

The time-domain signals that correspond to the spectra in Figs. 7.4(a), 7.4(b), and 7.4(c) are presented in Figs. 7.5(a), 7.5(b), and 7.5(c), respectively. One can clearly see that, with an increase in P_{in} from 0.7 mW to 7 W, the originally constant envelope of the time-domain signal breaks up into a periodic modulation with a period of about 2.0 μs which is the exact reciprocal of the frequency spacing of the comb spectrum in Fig. 7.4(b). As P_{in} is further increased to 14 W, a secondary modulation with a much longer period appears on the top of the first modulation. The

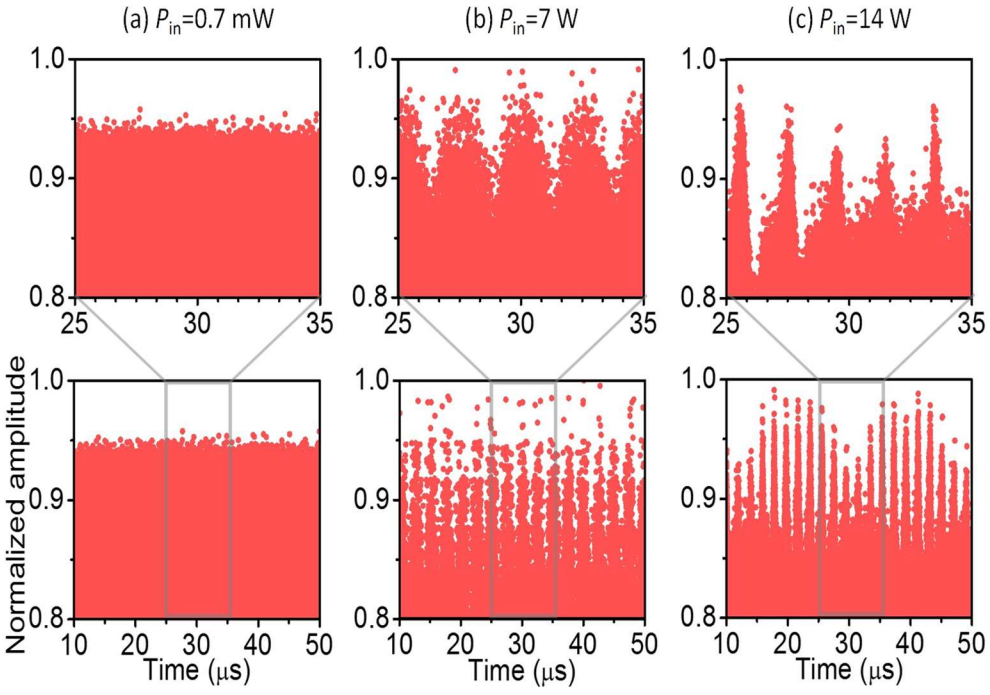

Fig. 7.5. Time-domain signals measured at different P_{in}, as indicated, demonstrating the development of two layers of MI.

period of this modulation is about 20 μs which is the reciprocal of the spacing of the daughter combs in Fig. 7.4(c).

The physical process that underlies the above-mentioned MI is the so-called four-wave interaction;[93,111] and in magnetic materials such an interaction is often termed as four-magnon scattering.[6,114] The process satisfies the energy conservation law $2\omega_0 = \omega_1+\omega_2$, where ω_0 and $\omega_{1,2}$ are the frequencies of the initial mode and the new side modes, respectively. When sufficiently strong, the side mode (ω_1 or ω_2) can interact with the initial mode (ω_0) to produce additional side modes through the four-wave interaction, resulting in an overall comb-like spectrum. As the conservation law can be rewritten as $\omega_2 - \omega_0 = \omega_0 - \omega_1$, one can expect the formation of a uniform comb that has an equal frequency spacing $\Delta\omega$. Indeed, all the combs shown in Fig. 7.4 are equally spaced. The spacing $\Delta\omega$ generally scales with $\frac{1}{\sqrt{|D|}}$,[93] and this is why the fractal appears in the transmission dip region only. In other words, the significantly enhanced dispersion in the transmission dip enables the generation of the granddaughter (and great-granddaughter) modes with small $\Delta\omega$. The MI rate, namely, the rate of the instability growth, generally scales with the square of the wave amplitude, $|u|^2$.[93] This explains why the fractal develops only at high P_{in}.

7.6 Conclusions

Several notes should be made about the fractal data shown in Figs. 7.4 and 7.5. First, the granddaughter and great-granddaughter combs are presented only for three selected daughter modes in Fig. 7.4, but they in fact also exist for other daughter modes. Second, the mother mode has less-developed granddaughter and great-granddaughter combs than the daughter modes. This is probably because the frequency of the mother mode is closer to the center of the transmission dip where D may have a relatively small value as shown in Fig. 7.3(f). Third, the $\frac{\Delta\omega}{2\pi}$ values for the

main combs in Figs. 7.4(b), 7.4(c), and 7.4(d) are 510 kHz, 500 kHz, and 495 kHz, respectively. The slight decrease of $\frac{\Delta\omega}{2\pi}$ with increasing P_{in} is consistent with the facts that one usually has $\Delta\omega \propto |u|$,[93] while the peak intensity of the mother mode slightly decreases with increasing P_{in} because of the re-distribution of energy to new side modes. Fourth, the great-granddaughter modes in Fig. 7.4(d) would be more visible if the diagrams are enlarged. Finally, due to instrumentational limitation, no fractals beyond pre-fractal 2 were observed in the frequency domain and only 2 layers of modulation were measured in the time domain. Future work that uses better instrumentation to demonstrate fractals of more layers is of great interest.

Finally, it should be noted that no fractals beyond pre-fractal 2 were observed in the frequency domain and only 2 layers of modulation were measured in the time domain. The main reasons for this include instrumentational limitation (limited sensitivities of the spectrum analyzer and the oscilloscope) and limited nonlinearity due to various sources of damping (for example, two-magnon scattering) and thermal issues arising at very high P_{in}. Future work that uses better instrumentation and stronger nonlinearity to demonstrate fractals of more layers is of great interest. It should also be noted that this work involves a constant field along the sample length direction, and a change in the field direction may lead to the absence of the above-presented fractals because both the dispersion and nonlinearity properties of spin waves strongly depend on the equilibrium direction of the magnetization.

In summary, this work demonstrates experimentally the development of an exact fractal for nonlinear spin waves in a quasi-1D magnonic crystal. The fractal exists in the frequency regions where the dispersion is significantly enhanced due to a spatially periodic potential and is generated through the four-wave interaction. The fractal manifests itself as three layers of comb-like spectra in the frequency domain and two layers of amplitude modulation in the time domain.

The new fractal fundamentally differs from the fractals found previously in nonlinear systems;[98,99,100] it arises spontaneously out of the fundamental magnonic crystal media, in contrast to previous approaches based on successive forcing of emergent structures, namely, solitons.

While this chapter utilized periodic patterns to alter the dispersion in YIG strips to observe spin-wave fractals, in the next chapter, non-periodic patterns are used to alter the dispersion to enable the observation of Anderson localization of spin waves. The spin-wave fractals are strongly nonlinear; however, the localized spin waves are a linear effect created by an absence of diffusion for specific wavenumbers and frequencies associated with the static properties and sample pattern dimensions.

Chapter 8. Spin waves in YIG strips with non-periodic patterns – observation of Anderson localization

8.1 Introduction to localization

Localization refers to the process by which any physical characteristic of a system is localized in space, time, or some other physical property. Anderson localization, along with weak and Mott localization, are commonly studied forms of a localized state. While the latter two are quantum mechanical in nature (used to describe band structures and quantum phase transitions), Anderson localization is a more general wave phenomenon that involves strong interference that leads to the absence of diffusion in a disordered medium.[115] Anderson localization was named after P. W. Anderson who was the first to theoretically show that the wave function describing the probability of finding an electron in a disordered medium was heavily localized when the disorder was large enough.[116] In chapter 7, a magnonic crystal consisting of a YIG film with periodic etched lines was used to alter the dispersion due to classically described constructive and destructive interference of the spin-wave modes. In this chapter, YIG strips with non-periodic, or random, metallic lines deposited on top were used to observe Anderson localization in a spin-wave system for the first time.

Anderson localization has been observed in many systems to study the conditions and limitations in which diffusion can be eliminated by disorder, including optical systems and electron systems.[117,118,119,120,121] However, several questions remain as to the types and strength of the disorder that lead to Anderson localization, as well as the role of losses. Anderson localization of spin waves is observed for the first time using Pt and Cu lines deposited on top of YIG film strips that were randomly spaced to act as disordered potential barriers for the traveling spin waves. YIG

strips with periodically spaced lines were also fabricated to compare localized states with standing waves where diffusion is still present. The primary mechanism for disorder in the system is the alteration of the dispersion due to electrical conductivity, and the data below show that localization can still occur in systems with higher losses where the disorder is due to strong scattering caused by the electrical conductivity of the metallic lines. In the previous works, losses are very low in comparison to the strength of the disorder. If the losses of the system are too high, the waves cannot localize, and the absence of diffusion is not due to the disorder pattern and thus there is no localized states. The strength of the localized states is much stronger in a spin-wave system than in other systems studied previously and is very classical in nature (reflections due to macroscopic electrical conductivity).

It's important to note that, here, there is a localized phase difference between moments, which implies a large localized concentration of spin, or momentum. Previous works involved a localization of the particles (such as photons or electrons) themselves, rather than a property of the particle. Not to mention that most of the previous observations of Anderson localization required temperatures far below room temperature to allow the particles to localize. Throughout the rest of

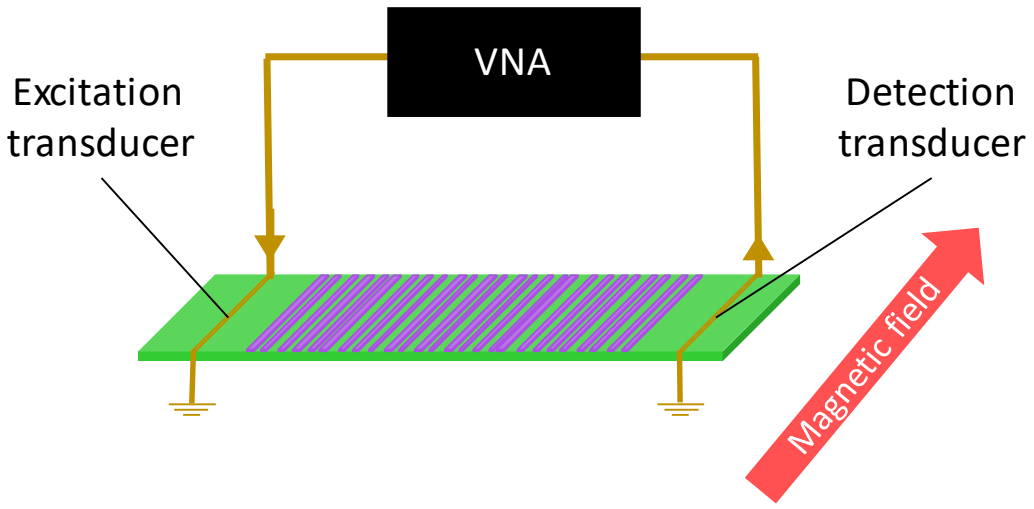

Fig. 8.1. Experimental setup for studying spin-wave localization.

the chapter, any use of the word localization is implied to mean Anderson localization.

8.2 Experimental setup and procedure

Randomly spaced metallic lines were fabricated on the top of $Y_3Fe_5O_{12}$ (YIG) thin film strips using a photolithography technique. The YIG films are about 10 mm long, 2.5 mm wide, and 10 μm thick. They were grown on single-crystal paramagnetic $Gd_3Ga_5O_{12}$ substrates. Both platinum and copper lines were used to make the same random patterns. There are 125 lines on each YIG film strip, which are all parallel to the width direction of the YIG film strips. The lines are all 5 nm thick, 2.5 mm long, and 20 μm wide, while the line spacing varies randomly between 20 μm and 30 μm. The random pattern was generated using a random number generator in excel. The spin waves in those YIG strips with randomly spaced metallic lines were measured in the surface spin wave configuration where the bias DC magnetic field is in the plane of the sample, but perpendicular to the YIG strip length as shown in Fig 8.1. Samples with periodically spaced platinum lines were also fabricated to better understand the data obtained from the random patterned samples. The spacing of periodic lines corresponds to the average of the spacing of the random pattern.

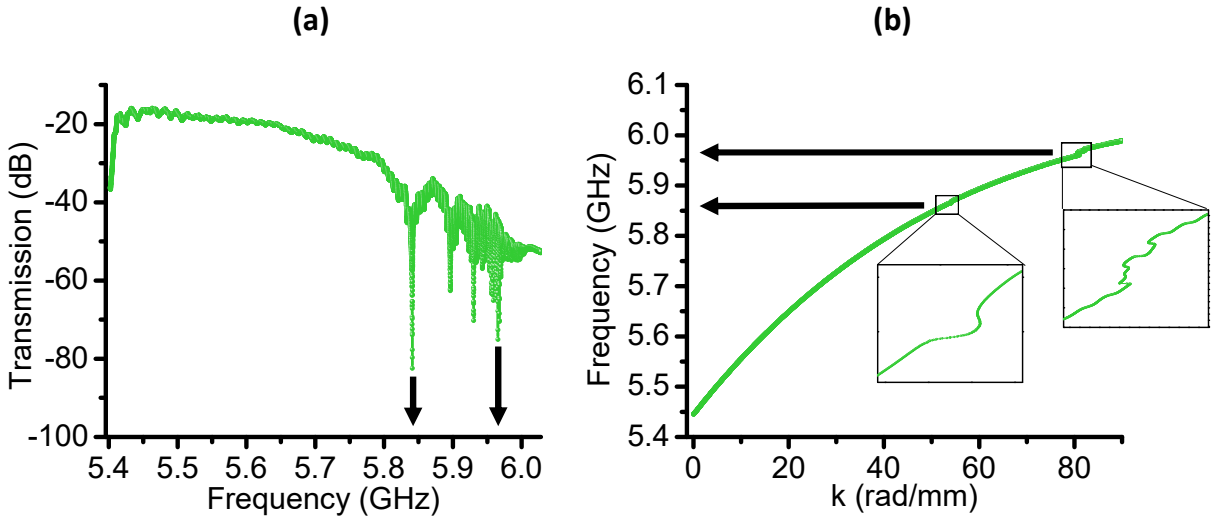

Fig. 8.2. Transmission and dispersion curves. (a) and (b) present the transmission vs. frequency profile and the frequency vs. wavenumber dispersion curve, respectively, obtained with a YIG film strip capped with a random platinum line pattern.

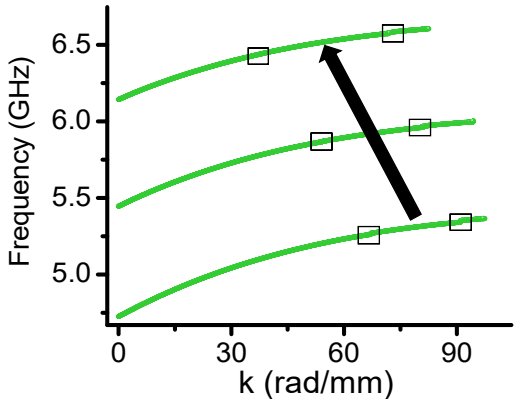

Fig. 8.3. Frequency vs. wavenumber dispersion curves measured at different fields (*H*) on the same sample as for the data shown in Fig. 8.2. Top: *H*=1020 Oe; middle: *H*=1260 Oe; bottom: *H*=1500 Oe.

In the randomly patterned YIG samples described above, one observed spin-wave localization that manifests itself as (1) pronounced dips in the transmission vs. frequency profiles and (2) characteristic oscillations in the frequency vs. wavenumber dispersion curve at the same frequencies where the transmission dips occur. Such transmission dips and dispersion oscillations are repeatable in samples fabricated at different times or using different metallic lines (platinum and copper). They show features that differ from the conventional spin-wave interferences observed in the periodically patterned YIG samples. The detailed data are presented below.

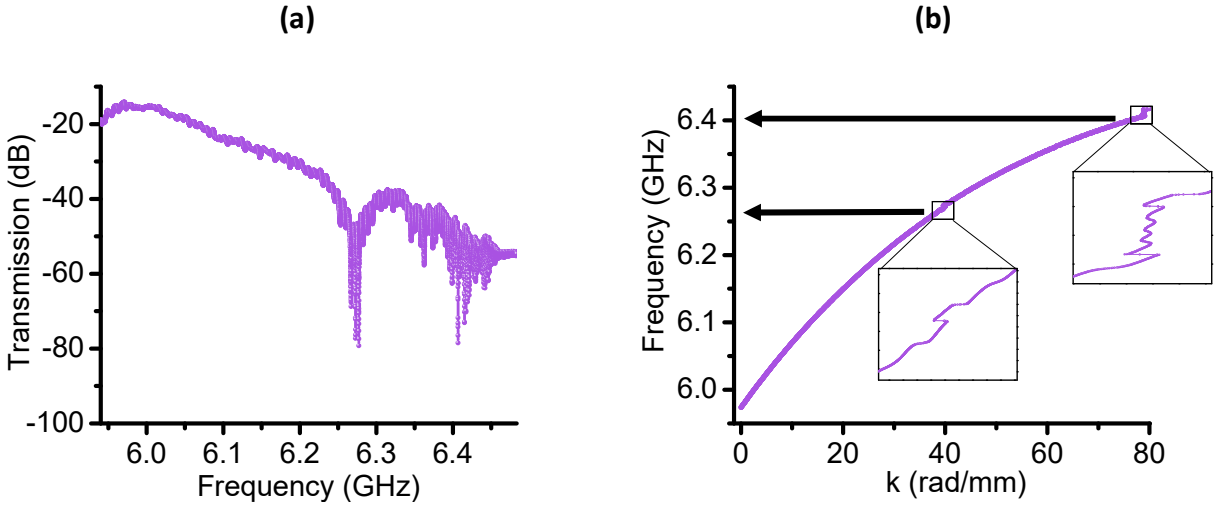

Fig. 8.4. Transmission and dispersion curves for a sample with random copper lines. (a) and (b) present the transmission vs. frequency profile and the frequency vs. wavenumber dispersion curve, respectively.

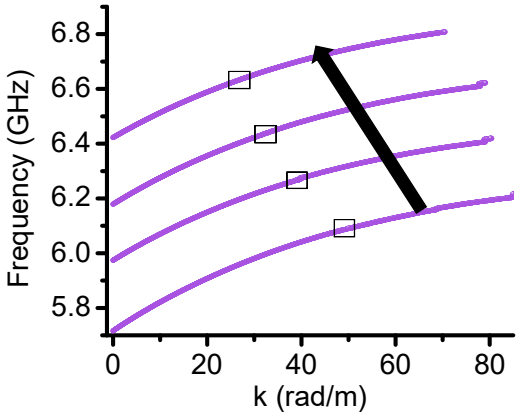

Fig. 8.5. Frequency vs. wavenumber dispersion curves measured at different fields (*H*) on the same sample as for the data shown in Fig. 8.4. The corresponding fields for the four curves from top to bottom are 1340 Oe, 1420 Oe, 1500 Oe, and 1580 Oe.

8.3 Platinum and copper patterns

The transmission and dispersion curves for the sample with random platinum pattern are presented in Figs. 8.2(a) and 8.2(b), respectively. Figure 8.1 shows the experimental configuration. Two microwave transducers, which are end-shorted microstrip lines, are placed on the two ends of the YIG strip to measure the complex transmission parameter S_{21} with the help of a vector network analyzer (VNA). The transmission coefficient in Fig. 8.2(a) is the magnitude of S_{21}, while the

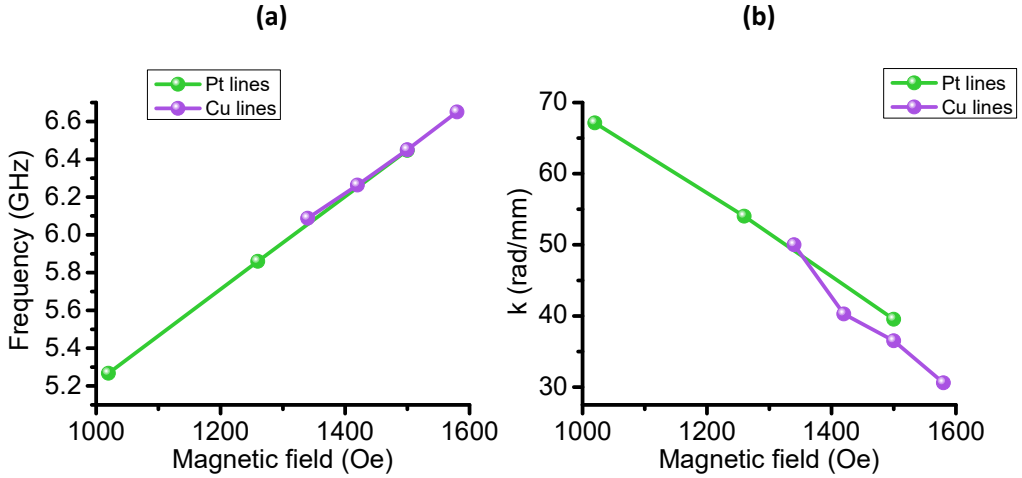

Fig. 8.6. Comparison of the data from samples with platinum and copper lines. (a) and (b) present the frequency and wavenumber, respectively, of the spin waves as a function of the magnetic field. The green and purple dots show the data obtained for the YIG films with random Pt and Cu line patterns, respectively.

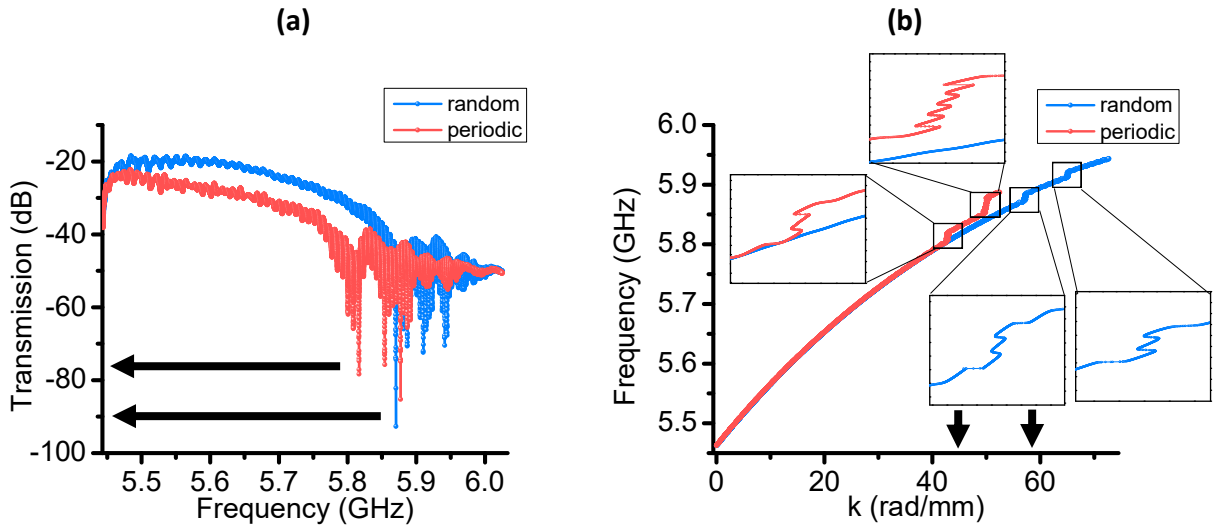

Fig. 8.7. Comparisons between the responses of the randomly (blue) and periodically (red) patterned YIG samples. (a) and (b) present the transmission vs. frequency profiles and the frequency vs. wavenumber dispersion curves, respectively.

dispersion curve in Fig. 8.2(b) is obtained by examining the phase of S_{21} with the distance between the two transducers taken into account. The transmission curve shows very strong dips at certain frequencies due to the random patterning. The first dip from the left is the principle dip, and comparisons between the samples will be made using this dip. The dispersion curve shows an oscillating response at the same frequencies which are indicated by the black arrows. Figure 8.3 presents the field dependence of this interference. One can see that there is a shift in the wavenumber k value with a change in the magnetic field, as indicated by the black arrow. The reason for this shift is unclear currently, but it might indicate that the group velocity plays an important role in the localization since the shift ensures a constant group velocity. The same results are indicated by the data obtained on the sample with random copper lines and presented in Figs. 8.4 and 8.5. Figure 8.6 compares the responses of the two samples. Although the field ranges where the localization was observed are different, the trend of the frequency vs. field response is the same. It is unclear what causes the diffence in field range, but this could be due to the diffrence in electrical conductivity.

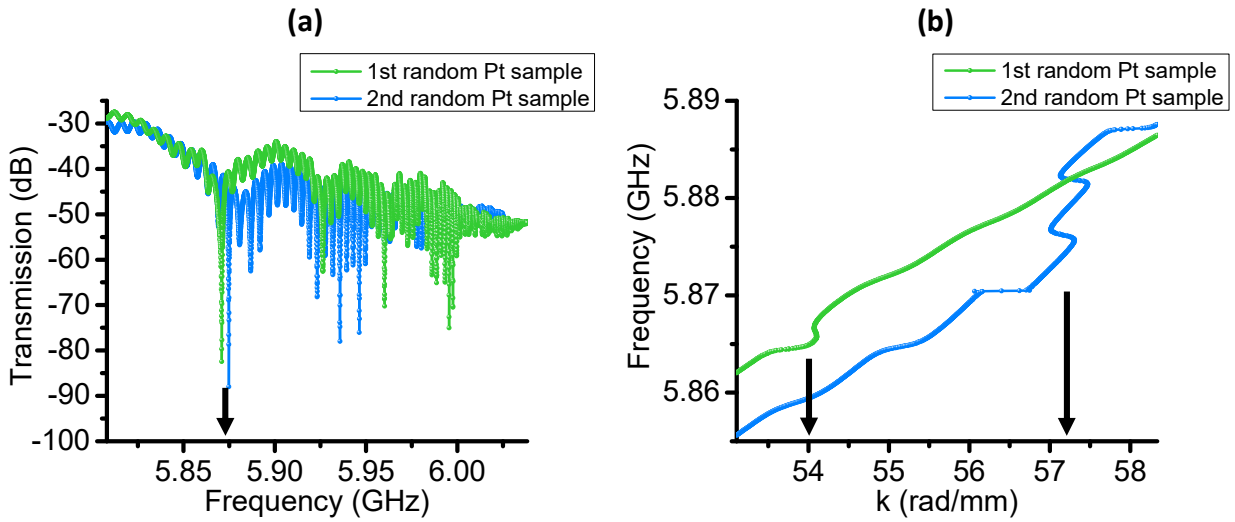

Fig. 8.8. Comparisons between the responses of the two randomly patterned YIG samples made separately. (a) and (b) present the transmission vs. frequency profile and the frequency vs. wavenumber dispersion curves, respectively.

8.4 Random vs. periodic platinum patterns

To better understand the above-presented interference due to the random patterning, a YIG film strip with a periodic pattern equal to the average spacing of lines in the random sample was fabricated. The average spacing was 32.2 micron. A new sample with the same random pattern was fabricated at the same time as the periodic pattern was made, to ensure similar quality. Figures 8.7(a) and 8.7(b) compare the transmission and dispersion curves, respectively, of the samples with the random and periodic patterns. The data indicate several remarkable results. First, while both the samples show characteristic responses in the transmission and dispersion curves, the responses occur at different frequency and wavenumber values. This indicates that the interference-like responses in the randomly patterned sample are not due to periodic averaging across the sample and are in fact attributed to the random pattern on the YIG film. Second, the characteristic responses in the random sample occur at a much higher k value than in the periodic sample, indicated by the black arrows. This is expected if the interference-like response in the random pattern is due to spin-wave localization. Third, the strength of the first principle dip for the sample

with a random pattern is much stronger than that for the sample with a periodic pattern, as indicated by the black arrows. Though microscope images (not shown here) suggest the periodic pattern is of much higher quality, it still shows weaker interferences. These three results together provide strong evidence that the characteristic interference-like responses in the random patterned YIG film are due to the localization along the YIG strip.

8.5 Control measurements

To study this further, measurements on two randomly patterned samples were carried out to test the repeatability and to see how the variance in the quality of the pattern changed the responses. The data for the two samples are presented in Fig. 8.8. One can see that the first principle dips occur at the frequencies which are very close to each other, and the responses in the dispersion curves also have very similar wavenumber values. Moreover, the strengths of the dips are also comparable. Though there is some variation, the difference in the samples with periodic and random patterns is much larger than these minor variations. It should be noted, however, that there is a difference in the shape in the k response. While the green data show a clear dip, the blue data show a wiggle-like response, or several dips. It is unclear if these responses are noise due to the lack of power at this frequency or if it is a key characteristic of the interference mechanism.

8.6 Conclusions

In conclusion, Anderson localization was observed for the first time in a spin-wave system where metallic lines on top of YIG film strips were used to create disorder for traveling spin waves. The lines acted as disorder potentials that led to the absence of diffusion of spin waves with a specific frequency (and wave number), corresponding to the random patterning. It is interesting that localization can still occur in systems with such large losses through such a classical

interference mechanism. Future work that investigates the roles of nonlinearity and stronger losses of spin waves are of great fundamental interest.

Chapter 9. Summary and outlook

9.1 Summary

In summary, Ch. 4-6 looked at exchange coupling and damping in magnetic recording media, while Ch. 7 and 8 looked at various spin wave phenomenon involving patterned structures made of YIG and other metallic elements. While the studies of magnetic recording media revealed the different types of scattering mechanisms caused by the propagating electromagnetic wave in the high-loss limit where moments are highly exchange coupled, the spin-wave experiments provided a more fundamental understanding of wave propagation and the various types of waveforms that can be observed in low-loss limits. Both are examples of the interactions of electromagnetic waves propagating in magnetically ordered materials, or magnetization dynamics.

Chapters 4-6 looked at exchange coupling and damping in magnetic recording media with high losses. Intergranular exchange coupling, interlayer exchange coupling, and damping were studied in current PMR media as well as future HAMR media provided by Western Digital and the National Institute for Material Science in Japan.

Chapters 7 and 8 looked at spin waves propagating in patterned structures with low losses. Spin-wave fractals and localization were observed using YIG films with periodic etched lines, periodic metallic lines deposited on top, as well as randomly spaced metallic lines deposited on top.

9.2 Outlook

There are still several open fundamental questions relevant to the subjects studied in this dissertation. The spin-wave fractals revealed that, for the first time, fractals can exist in nonlinear dynamics without involving solitons. Further studies that address specifically why and under what

conditions solitons and fractals must exist together are of great interest. It's not clear how nonlinearity and large losses will affect the localization of propagating spin waves. Future studies that investigate the stability of the localization under large nonlinearity and its relationship to the group velocity or dispersion would greatly help the current understanding of localization, not just in spin waves, but in general. New media samples with different properties and thus different scattering mechanisms and exchange coupling strengths would be of great interest. It would be interesting to create structures with even larger damping (larger than the already largest damping reported) and exchange coupled properties to study how the scattering strength changes as well as how the different mechanisms contribute to the overall damping. Though the work in this dissertation provides new insight into many interesting physical phenomena, there are still many questions to be answered and more studies on these topics are needed to fully understand the physics at play.

References

[1] J. D. Jackson, *Classical electrodynamics* (Wiley, New York, 1999).
[2] D. J. Griffiths, *Introduction to electrodynamics* (Pearson, Boston, 2013).
[3] D. D. Stancil and A. Prabhakar, *Spin waves-theory and applications* (Springer, New York, 2009).
[4] J. J. Sakurai and J. Napolitano, *Modern quantum mechanics* (Pearson, San Francisco, 2011).
[5] D. J. Griffiths, *Introduction to quantum mechanics* (Pearson, Upper Saddle River, 2005).
[6] M. Sparks, *Ferromagnetic-Relaxation Theory* (McGraw-Hill, 1964).
[7] J. Kunes and V. Kambersky, Phys. Rev. B **65**, 212411 (2002).
[8] V. Kambersky, Phys. Rev. B **76**, 134416 (2007).
[9] K. Gilmore, Y. U. Idzerda, and M. D. Stiles, Phys. Rev. Lett. **99**, 027204 (2007).
[10] T. Qu and R. H. Victora, Appl. Phys. Lett. **106**, 072404 (2015).
[11] J. M. Lock, Brit. J. Appl. Phys. **17**, 1645 (1966).
[12] R. D. McMicheal and P. Krivosik, IEEE Trans. Magn. **40** (1), 2 (2004).
[13] P. Landeros, Rodrigo E. Arias, and D. L. Mills, Phys. Rev. B **77**, 214405 (2008).
[14] P. Krivosik, N. Mo, S. Kalarickal, and C. E. Patton, J. Appl. Phys. **101**, 083901 (2007).
[15] L. Lu, *Damping mechanisms in magnetic recording materials and microwave-assisted magnetization reversal* (CSU, Fort Collins, 2014).
[16] N. Smith, IEEE Trans. Mag. **23** (4), 1995 (1987).
[17] T. L. Gilbert, IEEE Trans. Mag. **40** (6), 3443 (2004).
[18] S. M. Bhagat and P. Lubitz, Phys. Rev. B **10** (1), 179 (1974).
[19] N. A. Natekar, W. H. Hsu, and R. H. Victora, AIP Advances **7**, 056004 (2017).
[20] N. Bloembergen, Phys. Rev. **78**, 572 (1950).
[21] M. Tzoufras and M. K. Grobis, New J. Phys. **17**, 103014 (2015).
[22] L. Xu and S. Zhang, Physica E **45**, 72 (2012).
[23] D. A. Garanin, Phys. Rev. B **55** (5), 3050 (1997).
[24] R. F. L. Evans, D. Hinzke, U. Atxitia, U. Nowak, R. W. Chantrell, and O. Chubykalo-Fresenko, Phys. Rev. B **85**, 01443 (2012).
[25] L. Xu and S. Zhang, J. Appl. Phys. **113**, 163911 (2013).
[26] T. Holstein and H. Primakoff, Phys. Rev. **58**, 1098 (1940).
[27] G. D. Fratta, Proc. R. Soc. A **472**, (2016).
[28] B. A. Kalinikos and A. N. Slavin, J. Phys. C: Solid State Phys. **19** (35), 7013 (1986).
[29] Y. Ding, T. J. Klemmer, and T. M. Crawford, J. Appl. Phys. **96** (5), 2669 (2004).
[30] I. S. Maksymov and M. Kostylev, Physica E **69**, 253 (2015).
[31] D. Weller, G. Parker, O. Mosendz, E. Champion, B. Stipe, X. Wang, T. Klemmer, G. Ju, and A. Ajan, IEEE Trans. Magn. **50**, 1 (2014).
[32] L. Lu, M. Wu, M. Mallary, G. Bertero, K. Srinivasan, R. Acharya, H. Schultheiß, and A. Hoffmann, APL **103**, 042413 (2013).
[33] T. Oikawa, M. Nakamura, H. Uwazumi, T. Shimatsu, and H. Muraoka, IEEE Trans. Magn. **38**, 1682 (2002).
[34] H. Uwazumi, T. Shimatsu, M. Terakawa, Y. Sakai, S. Takenoiri, S. Watanabe, H. Muraoka, and Y. Nakamura, J. Magn. Soc. Jpn. **26**, 205 (2002).
[35] S. Oikawa, A. Takeo, T. Hikosaka, and Y. Tanaka, IEEE Trans. Magn. **36**, 2393 (2000).

[36] Y. Inaba, T. Shimatsu, T. Oikawa, H. Sato, H. Aoi, and H. Muraoka, IEEE Trans. Magn. **40**, 2483 (2004).
[37] T. Shimatsu, H. Uwazumi, H. Muraoka, and Y. Nakamura, IEEE Trans. Magn. **38**, 1973 (2002).
[38] H. Uwazumi, K. Enomoto, Y. Sakai, S. Takenoiri, T. Oikawa, and S. Watanabe, IEEE Trans. Magn. **39**, 1914 (2003).
[39] I. Tagawa and Y. Nakamura, IEEE Trans. Magn. **27**, 4975 (1991).
[40] T. Shimatsu, T. Kondo, K. Mitsuzuka, S. Watanabe, H. Aoi, H.Muraoka, and Y. Nakamura, IEEE Trans. Magn. **43**, 2091 (2007).
[41] Y. Liu, K. Dahmen, and A. Berger, Phys. Rev. B **77**, 1 (2008).
[42] C. Papusoi, K. Srinivasan, and R. Acharya, J. Appl. Phys. **110**, 083908 (2011).
[43] M. El-Hilo, K. O'Grady, P. I. Mayo, R. W. Chantrell, I. L. Sanders, and J. K. Howard, IEEE Trans. Magn. **28**, 3282 (1992).
[44] J. P. C. Bernards and H. Cramer, J. Magn. Magn. Mat. **120**, 221 (1993).
[45] H.Uwazumi, T. Shimatsu, and Y.Kuboki, J. Appl. Phys. **91**, 7095 (2002).
[46] O. Perevertov, J. Phys. D: Appl. Phys. **36**, 785 (2003).
[47] R. J. M. van de Veerdonk and D. Weller, IEEE Trans. Magn. **39**, 590 (2003).
[48] A. Berger, Y. Xu, B. Lengsfield, Y. Ikeda, and E. E. Fullerton, IEEE Trans. Magn. **41**, 3178 (2005).
[49] H. Nemoto, I. Takekuma, H. Nakagawa, T. Ichihara, R. Araki, and Y. Hosoe, J. Magn. Mat. **320**, 3144 (2008).
[50] S. Hinata, S. Saito, N. Itagaki, and M. Takahashi, IEEE Trans. Magn. **48**, 1248 (2012).
[51] S. Hinata, S. Saito, and M. Takahashi, IEEE Trans. Magn. **48**, 3177 (2012).
[52] M. Zheng, B. R. Acharya, G. Choe, J. N. Zhou, Z. D. Yang, E. N. Abarra, and K. E. Johnson, IEEE Trans. Magn. **40**, 2498 (2004).
[53] T. Shimatsu, H. Sato, T. Oikawa, Y. Inaba, O. Kitakami, S. Okamoto, H. Aoi, H. Muraoka, and Y. Nakamura, IEEE Trans. Magn. **41**, 566 (2005).
[54] D. Laughlin, N. Nuhfer, S. Park, H. Yuan, and J. Zhu, J. Appl. Phys. **105**, 07B739 (2009).
[55] Y. Ding, T. J. Klemmer, and T. M. Crawford, J. Appl. Phys. **96**, 2969 (2004).
[56] H. T. Nembach, T. J. Silva, J. M. Shaw, M. L. Schneider, M. J. Carey, S. Maat, and J. R. Childress, Phys. Rev. B **84**, 054424 (2011).
[57] L. Pan and D. B. Bogy, Nat. Photonics **3**, 189 (2009).
[58] D. Weller, G. Parker, O. Mosendz, E. Champion, B. Stipe, X. Wang, T. Klemmer, G. Ju, and A. Ajan, IEEE Trans. Magn. **50** (1), 3100108 (2014).
[59] C. Vogler, C. Abert, F. Bruckner, D. Suess, and D. Praetorius, Appl. Phys. Lett. **108**, 102406 (2016).
[60] D. Weller, G. Parker, O. Mosendz, A. Lyberatos, D. Mitin, N. Y. Safonova, and M. Albrecht, J. Vac. Sci. technol. B **34** (6), 060801 (2016).
[61] P. Krivosik, S. S. Kalarickal, N. Mo, S. Wu, and C. E. Patton, Appl. Phys. Lett. **95**, 052509 (2009).
[62] N. Mo, J. J. Green, P. Krivosik, and C. E. Patton, J. Appl. Phys. **101**, 023914-1 (2007).
[63] S. Mizukami, S. Iihama, N. Inami, T. Hiratsuka, G. Kim, H. Naganuma, M. Oogane, and Y. Ando, Appl. Phys. Lett. **98**, 052501 (2011).
[64] J. Becker, O. Mosendz, D. Weller, A. Kirilyuk, J. C. Maan, P. C. M. Christianen, Th. Rasing, and A. Kimel, Appl. Phys. Lett. **104**, 152412 (2014).
[65] K. Lee, H. Song, J. Kim, H. S. Ko, J. Sohn, B. Park and S. Shin, Appl. Phys. Express **7**,

113004 (2014).
[66] A. Perumal, Y. K. Takahashi, and K. Hono, Appl. Phys. Express **1**, 101301 (2008).
[67] L. Zhang, Y. K. Takahashi, A. Perumal and K. Hono, J. Magn. Magn. Mater. **322**, 2658 (2010).
[68] B. S. D. Ch. S. Varaprasad, J. Wang, T. Shiroyama, Y. K. Takahashi, K. Hono, IEEE Trans. Magn. **51** (11), 3200904-1 (2015).
[69] J. Wang, S. Hata, Y.K. Takahashi, H. Sepehri-Amin, B.S.D. Ch.S. Varaprasad, T. Shiroyama, T. Schrefl, K. Hono, ACTA Materialla. **91** (1), 41 (2015).
[70] S. S. Kalarickal, P. Krivosik, J. Das, K. S. Kim, and C. E. Patton, Phys. Rev. B **77**, 054427 (2008).
[71] S. Kalarickal, P. Krivosik, M. Wu, C. Patton, M. Schneider, P. Kaobs, T. Silva, and J. Nibarger, J. Appl. Phys. **99**, 093909 (2006).
[72] M. Wu and A. Hoffmann, Recent Advances in Magnetic Insulators – From Spintronics to Microwave Applications (Solid State Physics Vol. 64, Academic Press, Burlington, 2013).
[73] M. Wu, "M-Type Barium Hexagonal Ferrite Films," in Advanced Magnetic Materials, Edited by L. Malkinski (InTech, Rijeka, 2012). ISBN: 978-953-51-0637-1.
[74] J. Dubowik, K. Zaleski, H. Glowinski, and I. Goscianska, Phys. Rev. B **8**4, 184438 (2011).
[75] D. Suess, T. Schrefl, S. Fahler, M. Kirschner, G. Hrkac, F. Dorfbauer, and J. Fidler, Appl. Phys. Lett. **87**, 012504 (2005).
[76] A. Berger, N. Supper, Y. Ikeda, B. Lengsfield, A. Moser, and E. Fullerton, Appl. Phys. Lett. **93**, 122502 (2008).
[77] G. Choe, M. Zheng, B. Acharya, E. Abarra, and J. Zhou, IEEE Trans. Mag. **41** (10), 3172 (2005).
[78] H. Jung, E.Velu, S. Malhotra, G. Bertero, and U. Kwon, J. Magn. Magn. Mat. **320** (22), 3151 (2008).
[79] Y. Tserkovnyak, A. Brataas, and G. E.W. Bauer, Phys. Rev. Lett. **88**, 117601 (2002).
[80] B. Heinrich, Y. Tserkovnyak, G. Woltersdorf, A. Brataas, R. Urban, andG.E.W. Bauer, Phys. Rev. Lett. **90**, 187601 (2003).
[81] E. Simanek and B. Heinrich, Phys. Rev. B **67**, 144418 (2003).
[82] W. Zhang, M. B. Jungfleisch, W. Jiang, J. Sklenar, F. Y. Fradin, J. E. Pearson, J. B. Ketterson, and A. Hoffmann, J. Appl. Phys. **117**, 172610 (2015).
[83] J. Tsai, H. Tzeng, and G. Lin, Appl. Phys. Lett. **96**, 032505 (2010).
[84] H. Guo, J. Liao, Z. Zhang, Q. Jin, W. Rui, J. Du, H. Wang, and J. Wang, Appl. Phys. Lett. **111**, 103916 (2012).
[85] D. Weller, G. Parker, O. Mosendz, E. Champion, B. Stipe, X. Wang, T. Klemmer, G. Ju, and A. Ajan, IEEE Trans. Magn. **50** (1), 3100108 (2014).
[86] M. Schoen, D. Thonig, M. Schneider, T. Silva, H. Nembach, O. Eriksson, O. Karis, and J. Shaw, Nat. Phys. **12**, 839 (2016).
[87] D. Richardson, K. Srinivasan, S. Katz, and M. Wu, Appl. Phys. Lett. **111**, 183506 (2017).
[88] D. Richardson, S. Katz, J. Wang, Y. K. Takahashi, K. Srinivasan, A. Kalitsov, K. Hono, A. Ajan, and M. Wu, Phys. Rev. Appl., under review (2018).
[89] N. Mo, J. Hohlfeld, M. ul Islam, C. S. Brown, E. Girt, P. Krivosik, W. Tong, A. Rebei, and C. E. Patton, Appl. Phys. Lett. **92**, 022506 (2008).
[90] M. Oogane, T. Wakitani, S. Yakata, R. Yilgin, Y. Ando, A. Sakuma, and T. Miyazaki, Jap. J. Appl. Phys. **45** (5A), 3889 (2006).
[91] B. Cullity and C. Graham, *Introduction to Magnetic Materials* (Wiley, Hoboken NJ, 2009).
[92] P. Bruno, J. Magn. Soc. Jpn. **15**, 15 (1991).

[93] M. Remoissenet, *Waves Called Solitons: Concepts and Experiments* (Springer, Berlin, 1999).
[94] Y. S. Kivshar and G. P. Agrawal, *Optical Solitons: From Fibers to Photonic Crystals* (Academic, San Diego, CA, 2003; Fizmatgiz, Moscow, 2005).
[95] M. Segev, M. Soljacic, and J. M. Dudley, Nat. Photonics **6**, 209 (2012).
[96] M. V. Berry, J. Phys. A **12**, 781 (1979).
[97] O. Mendoza-Yero, B. Alonso, G. Mínguez-Vega, Í. J. Sola, J. Lancis, and J. A. Monsoriu, Oppt. Lett. **37**, 1145 (2012). doc ID:156405.
[98] M. Soljacic, M. Segev, and C. R. Menyuk, Phys. Rev. E **61**, R1048 (2000).
[99] S. Sears, M. Soljacic, M. Segev, D. Krylov, and K. Bergman, Phys. Rev. Lett. **84**, 1902 (2000).
[100] M. Wu, B. Kalinikos, L. Carr, and C. Patton, Phys. Rev. Lett. **96**, 187202 (2006).
[101] V. V. Kruglyak and A. N. Kuchko, J. Magn. Magn. Mat. **272**, 303 (2004).
[102] A. V. Chumak, A. A. Serga, B. Hillebrands, and M. P. Kostylev, Appl. Phys. Lett. **93**, 022508 (2008).
[103] A. V. Chumak, A. A. Serga, S. Wolff, B. Hillebrands, and M. P. Kostylev, Appl. Phys. Lett. **94**, 172511 (2009).
[104] Z. K. Wang, V. L. Zhang, H. S. Lim, S. C. Ng, M. H. Kuok, S. Jain, and A. O. Adeyeye, Appl. Phys. Lett. **94**, 083112 (2009).
[105] S. Tacchi, F. Montocello, M. Madami, G. Gubbiotti, G. Carlotti, L. Giovannini, R. Zivieri, F. Nizzoli, S. Jain, A. O. Adeyeye, and N. Singh, Phys. Rev. Lett. **107**, 127204 (2011).
[106] A. V. Drozdovskii and B. A. Kalinikos, JETP Lett. **95**, 357 (2012).
[107] J. R. Vivas, S. Mamica, M. Krawczyk, and V. V. Kruglyak, Phys. Rev. B **86**, 144417 (2012).
[108] S. V. Grishin, E. N. Beginin, M. A. Morozova, Yu. P. Sharaevskii, and S. A. Nikitov, J. Appl. Phys. **115**, 053908 (2014).
[109] L. Ordonez-Romero, Z. Lazcano-Ortiz, A. Drozdovskii, B. Kalinikos, M. Aguilar-Huerta, J. L. Dominguez-Juarez, G. Lopez-Maldonado, N. Qureshi, O. Kolokoltsev, and G. Monsivais, J. Appl. Phys. **120**, 043901 (2016).
[110] K. Tai, A. Hasegawa, and A. Tomita, Phys. Rev. Lett. **56**, 135 (1986).
[111] V. E. Zakharov and L. A. Ostrovsky, J. Phys. D **238**, 540 (2009).
[112] M. Erkintalo, K. Hammani, B. Kibler, C. Finot, N. Akhmediev, J. M. Dudley, and G. Genty, Phys. Rev. Lett. **107**, 253901 (2011).
[113] P. Kabos and V. S. Stalmachov, *Magnetostatic Waves and Their Applications* (Chapman and Hall, London, UK, 1994).
[114] A. G. Gurevich and G. A. Melkov, *Magnetization Oscillations and Waves* (CRC Press, Boca Raton, FL, 1996).
[115] P. Sheng, *Introduction to Wave Scattering, Localization, and Mesoscopic Phenomenon* (Springer, Berlin, Germany, 2006).
[116] P. W. Anderson, Phys. Rev. **109**, 1492 (1958).
[117] M. Storzer, P. Gross, C. Aegerter, and G. Maret, Phys. Rev. Lett. **96**, 063904 (2006).
[118] Y. Lahini, A. Avidan, F. Pozzi, M. Sorel, R. Morandotti, D. Christodoulides, and Y. Silberberg, Phys. Rev. Lett. **100**, 013906 (2008).
[119] G. Roati, C. D'Errico, L. Fallani, M. Fattori, C. Fort, M. Zaccanti, G. Modugno, M. Modugno, and M. Inguscio, Nat. **453**, 895 (2008).
[120] T. Ying, Y. Gu, X. Chen, X. Wang, S. Jin, L. Zhao, W. Zhang, and X. Chen, Sci. Adv. **2** (2), e1501283 (2016).
[121] S. Choi, S. Kim, Z. Ku, M. Visbal-Onufrak, S. Kim, K. Choi, H. Ko, W. Choi, A. Urbas, T. Goo, and Y. Kim, Nat. Comm. **9** (1), 452 (2018).